ON THE COLLAPSE OF
LONG THICK-WALLED CIRCULAR TUBES
UNDER BIAXIAL LOADING

Thesis by

Raghu Madhavan

In Partial Fulfillment
of the Requirements for the Degree of
Doctor of Philosophy

California Institute of Technology
Pasadena, California

1988
(Submitted 10 March 1988)

ACKNOWLEDGMENTS

ABSTRACT

The collapse phenomenon of long, thick-walled tubes subjected to axial tension and external pressure is investigated. A combined experimental and analytic approach is adopted. The diameter to thickness ratio (D/t) of the tubes studied is in the range 10-40.

A series of collapse tests are conducted using thick-walled, small diameter tubes of two different materials. Careful measurements of geometrical and material parameters are carried out before each collapse test. Tension-Pressure collapse envelopes are obtained for tubes of different D/t and loading paths. Collapse tests involving initially ovalized tubes are also carried out. The results show that collapse strength is strongly influenced by initial ovality.

A two-dimensional model is used for predicting the collapse strength. The limit point behavior of a long tube with initial geometric imperfections has been modeled. The tube is assumed to be under generalized plane strain conditions and the possible variations of material and geometric parameters along the length are not considered. Hill's anisotropic plasticity theory involving a quadratic yield function is used to model the anisotropies in yield shown by drawn tubes. A power law creep model is employed to assess the effect of primary creep on collapse strength.

The interaction between collapse pressure and tension is found to depend on both material and geometric parameters. The yield behavior of the tube material strongly affects the collapse phenomenon. Initial ovality of the tube is shown to be a very important geometric parameter that influences collapse strength. The effect of primary creep on collapse is shown to be not very significant, for the type of materials used (304 stainless steel and 6061-O aluminum).

TABLE OF CONTENTS

LIST OF FIGURES

LIST OF TABLES

LIST OF SYMBOLS

Symbol	Description
A_o, A_n	= Fourier Coefficients
B_n	= Fourier Coefficients
a_n, b_n	= Displacement Coefficients
D	= Tube Outer Diameter
D_i	= Tube Inner Diameter
D_{max}, D_{min}	= Maximum and Minimum Tube outer Diameter
D_o	= Tube Mean Diameter (= D - t)
E	= Young's Modulus
e	= Membrane Strain
H	= Plastic Tangent Modulus
K	= LVDT Constant (inches/volt)
N	= Number of Terms in the Displacement Expansion
n	= Material Hardening Parameter
P	= Pressure
P_c	= Elastic Buckling Pressure = $\dfrac{E}{4(1-\nu^2)}\left[\dfrac{t}{R_o}\right]^3$
P_{co}	= Collapse Pressure
P'_o	= Yield Pressure = $\sigma'_o t / R_o$
R	= Tube Outer Radius = $D/2$
R_θ	= Tube Mean Radius at Angle θ (see Figure 12)
R_o	= Tube Mean Radius = $(D-t)/2$
s	= Tube Mid-surface Coordinate
S_θ, S_r	= Anisotropic Parameters
T	= Axial Tension
T_c	= Axial Tension at Collapse

T'_o = Yield Tension = $2\pi R_o\, t\, \sigma'_o$

t = Mean Wall Thickness of the Tube or Time in Chapter 6

t_e = Effective Time in the Power Law Creep Model

u = Axial Displacement

V = Voltage Output from LVDT

v = Circumferential Displacement

W = Work Done by External Loads in the Virtual Work Expression

w_{max} = Maximum Radial Displacement

w_o = Amplitude of Initial Ovality ($\Delta'_o = w_o/R_o$)

x = Axial Coordinate

z = Through Thickness Coordinate

Δ'_o = Initial Ovality = $D_{max} - D_{min}/2D$

Δ''_o = Initial Ovality = $2(A_2^2 + B_2^2)^{1/2}/D$

$\varepsilon, \varepsilon_\theta, \varepsilon_x$ = Strains

ε_e^p = Equivalent Plastic Strain

ε_o = Axial Strain ε_x Under Generalized Plane Strain Conditions

ε_{xc} = Axial Strain at Collapse

θ = Angular Coordinate

K_s = Curvature

Λ = Loading parameter

ν = Poisson's Ratio

$\sigma, \sigma_\theta, \sigma_x$ = Stresses

σ_e = Equivalent Stress

σ_{ij} = Stress Tensor Components

σ_o = Yield Stress (0.2 % strain offset)

σ'_o = API Yield Stress = $\sigma|_{\varepsilon=0.5\%}$

$\sigma_{or}, \sigma_{o\theta}, \sigma_{ox}$ = Initial Yield Stresses in the Radial, Hoop, and Axial Directions

σ_R = Bending Residual Stress at the Tube Inner Wall

σ_y = Ramberg-Osgood Yield Stress

Chapter 1

GENERAL INTRODUCTION

1.1. Motivation.

Thick-walled tubular components are often used as structural members in many practical engineering applications. They appear as heat exchanger components in conventional power plants and nuclear reactors, as high pressure containers in the chemical industry and as deep submersibles. In oil well drilling, the drill string itself consists of many lengths of tubes connected together. Oil casings are tubular structural parts used as protective conduits for the downhole production machinery while drilling for oil. They are also very widely used in the exploration and extraction of oil and natural gas in the offshore areas. Very often these tubular parts are subjected to combined loads which include an effective external pressure loading. Such loading conditions can lead to the catastrophic collapse of these components called a plastic instability failure. For developing a better and simpler design process for these structural parts, it is important to have a better understanding of the collapse phenomenon under combined loading.

The oil and gas industries are currently involved in increased exploration of the offshore areas in deeper water. Marine pipelines are widely used in this continuing exploration process and also for the extraction of oil, natural gas and other minerals. In shallow waters, the most important parameters in the design of a pipeline are based on optimizing the internal flow and minimizing the corrosion problems. At greater water depths, the external pressure which increases linearly with the depth becomes the main concern. These offshore pipelines are subjected to extreme loading conditions during both their installation and operation. Feasibility studies conducted by the oil and gas industries [1] have shown acceptable costs for exploration and extraction at water depths up to 10,000 ft. The design of a pipeline under such severe conditions is guided by the collapse strength of the pipe under the combined loading of external pressure and axial tension, or bending.

In Figure 1.1, the conventional pipe laying technique used in water depths up to 3,000 ft., in which the line is payed into the water in an " S " configuration from a lay barge, is shown. For

water depths above 3,000 ft., another pipe laying method in which the line that leaves the lay barge takes a " J " configuration as shown in Figure 1.2 is used. Figure 1.3 represents the latest generation of floating production systems (FPS) and tension leg platforms (TLP), which house production risers bringing oil and natural gas to the platform from various drill sites on the sea floor. In all these examples, long strings of line pipe coming down from an installation at sea surface to the sea floor are shown. It can be clearly seen that the weight of the pipe string results in an axial tensile load distribution in which it is a maximum at the surface level going to a minimum at the bottom. The ambient pressure acting on the pipe is proportional to the water depth. At some intermediate section away from the bottom, depending on the pipe geometry and specific weight [2], the worst combination of external pressure and tension is expected to occur. Based on the configuration of the pipe string, certain locations are also subjected to high bending moments. The movement of the sea level installation with the winds, currents and waves, further causes small amplitude cycling of the load states on the pipeline, thus accelerating its deterioration. In such environments, a local collapse pattern can develop at the weakest location on the line if the loads are large enough. The propagating nature [3-6] of the collapse at ambient pressures much lower than the initiation pressure makes the problem more challenging. Collapse results in the flattening of the tube and high circumferential strains develop along the sides of the tube. This can in turn lead to fracturing of the tube resulting in severe environmental impacts.

For deep water applications, in order to withstand the higher pressures, tubular structures of lower diameter to thickness ratio (D/t) are required. Thick-walled tubes characterized by low D/t values exhibit inelastic collapse failure. This study was motivated by the need to develop a predictive tool for the collapse of thick tubes under the combined loading of axial tension and external pressure.

1.2. Definition of Collapse.

An ideal, geometrically perfect tube subjected to axial tension and external pressure will exhibit a bifurcation type instability. At this bifurcation load, the tube response changes from an axisymmetric mode to a non-axisymmetric mode. It has been shown [7,8] that a thick-walled tube under external pressure is an imperfection sensitive structure. This sensitivity to

imperfections can be demonstrated [9,10] by a postbuckling analysis of the perfect tube. Presence of initial geometric imperfections, in the form of wall thickness variations and out-of-roundness of the tube, changes the response of the tube to a limit point type behavior. This means that when a load controlled situation exists, the tube will collapse when the loads reach the limit point value. As the structure is imperfection sensitive, the imperfections lower the limit load to below the bifurcation load. In the case of a thick-walled tube, this situation is schematically shown in Figure 1.4.

It was found that the collapse envelope under combined tension and pressure is not very sensitive to the order in which loads are applied. For an initially imperfect tube, the role of tension is such that the tube section when subjected to external pressure will undergo larger non-axisymmetric displacements before reaching a limit pressure of lower value. The extent of this interaction depends on the material and geometric properties of the tube. This response is illustrated in Figures 3.2a and 3.2b. These Figures represent the limit point load-displacement behavior of an initially imperfect tube characterized by a typical set of geometrical and material parameters observed in the experiments.

1.3. Research Background.

The problem of collapse of thick-walled tubes under external pressure alone has been extensively studied. The classical result for the buckling of a thin elastic ring, which is essentially same as a long circular cylinder with no end effects, was developed by Levy [11], in 1884, and by Bryan [12], in 1888, through different approaches. Southwell [13], in 1915, developed simple expressions for the pressure at which yielding occurs to approximate the collapse pressure of a geometrically perfect tube. Timoshenko [14], in 1933, included the effect of imperfections on collapse strength by deriving the pressure at which yielding begins at the inner wall of an initially ovalized tube, to approximate the collapse pressure. Investigations that followed [15-17] assessed the importance of parameters such as inelastic material properties and initial geometric imperfections.

For combined axial tension and pressure loading, some of the earliest experiments were conducted by Edwards and Miller [18] in 1939. They covered a D/t range of 22 to 11 to develop an empirical design criterion for oil well casing under combined loading. Their

experimental results applied a loading path of T→P (see Figure 2.12). They did not measure the initial geometric imperfections of the specimen. In spite of this, later investigators seem to have used this data widely in supporting their design criteria for combined loading.

In 1959, Stuiver and Tomalin [19] carried out a group of collapse tests under combined pressure and axial loads. Their specimens covered a D/t range of 28-23. They used tubes of nearly perfect geometry obtained by careful machining of their specimen, but did not address the influence of imperfections on the collapse strength. The experimental results were then used to check the possibility of using the yield envelope under combined loads as an approximate collapse envelope. Lubinski [20], in 1975, in a very similar vein, addressed the possibility of using the yield envelope based on distortional energy theory as the collapse envelope under combined loading for the design of oil well casings.

An elastic bifurcation analysis, to get the critical loads of a thick tube under the combined loading of tension, pressure and bending, was developed by Fabian [21] in 1977. Shallow shell equations were used in the analysis, which took into account the variation of strain through thickness. The results from the initial postbuckling analysis clearly showed the imperfection sensitivity of the tubes.

The current approach for the design of casings, line and drill pipes under combined tension and pressure, as recommended by the American Petroleum Institute (API) [22], defines the yield envelope as the collapse strength envelope. This may be considered meaningful only in the limited cases where the collapse strength is proportional to the yield strength. Also, this procedure is not applicable for design, when axial tensile loads exceeding the yield tension of the tube are present. Kyogoku et al. [23], in 1981, reported a series of tests on full size commercial casings and used the results to support the API design equations. Along similar lines, Tamano et al. [24], in 1982, reported another series of experiments on commercial grade casings to check the API recommendations. However their test specimen had a length to diameter ratio of 7, and is not considered long enough to eliminate any end effects on collapse strength. These test results suggested that, for commercial casings, the API recommended design formula gives conservative estimates for collapse strength.

Huang and Pattillo [25,26] suggested the use of a tangent modulus approach to obtain the bifurcation loads. They used thin shell equations to derive an expression for the critical pressure when axial tension also is present. They noted the difference in collapse envelopes predicted with the incremental and deformation theories of plasticity. Bifurcation loads obtained using deformation theory gave better agreement with the experiments. Later, Pattillo [27] reported a new formulation in which the effect of initial geometric imperfections in the form of an ovality was included.

1.4. Objective and Scope.

Most of the previous studies on the collapse under combined loads concentrated on generating empirical equations for design purposes. The simplest way to predict the critical load of a thick-walled tube is to approximate it with the tube's bifurcation load. This obviously implies neglecting the effect of initial geometric imperfections on the collapse strength.

The purpose of the present investigation is to use a combined experimental and analytic approach to study the collapse phenomenon of thick-walled tubes under external pressure and axial tension. The diameter to thickness ratio (D/t) range studied is 10-40. This D/t range is also of interest to the oil industry. The possibility of using a simple two dimensional model to predict the collapse strength is investigated in detail. A series of collapse experiments under combined tension and external pressure loading were carried out using different materials and different loading paths. The test data thus obtained were then used to check the accuracy of the model. An anisotropic material model was implemented for better predictions of the collapse strength. The deteriorating effect of initial ovality imperfections on collapse strength was established. The effect of primary creep on the collapse strength was also studied. A simple model was developed to assess this effect for tube materials that show less dominant creep characteristics. The model was then used to study the sensitivity of the collapse strength to the various parameters involved.

A detailed description of the experimental setup and procedures is given in Chapter 2. Some of the details of the problem formulation and the assumptions involved are given in Chapter 3. In Chapter 4, the accuracy of the model is assessed by comparing the numerical predictions with the experimental results. The sensitivity of collapse strength to material

parameters, geometric parameters and residual stresses in the initial configuration is evaluated using the model. The results of this parametric study are given in Chapter 5. In Chapter 6, the effect of primary creep on collapse strength is studied.

Chapter 2

COLLAPSE EXPERIMENTS AND EXPERIMENTAL RESULTS

In this chapter, the details of the experimental procedure are described, and the results obtained are illustrated with tables and figures. Thick-walled tubes of small diameter were used to prepare the specimens in the collapse tests. The experimental facility developed for these tests had a pressure rating of 10,000 psi and a tensile load capacity of 20,000 lbs. The setup allowed very fine control over the loads so that different combinations of axial tension and pressure for collapse could be tested. The experimental effort consisted of initial ovality measurements, material property testing and collapse testing. The details are explained in the following sections.

2.1. Description of Experiments.

2.1.1. *Initial Ovality Measurements.* The collapse strength of a long tube is strongly influenced by its initial geometric imperfections, especially its initial ovality. An experimental rig was therefore developed to measure these initial imperfections with sufficient accuracy. A photograph of the setup is shown in Figure 2.1. The concept applied in this imperfection measuring device was developed by Arbocz and Babcock [28,29]. The setup could accommodate test specimens of up to 45 inches in length and the accuracy of displacement measurements was within 3×10^{-5} inches (~ 0.001 mm).

A test specimen was first prepared by bonding an appropriate length of the tubing to the end plugs as shown in Figure 2.9. A schematic of the test specimen is given in Figure 2.10. The specimen was then mounted between two centers in the setup. A high resolution Linear Variable Differential Transducer (LVDT) was used for out-of-roundness measurements. Its spring loaded probe (see Figures 2.1, 2.2) touched the tube surface, as the tube was rotated about an axis between the two centers. One of the centers was attached to a disk which carried a tape with black and silver stripes along its circumference. This disk rotated with the tube and the angular position of the tube relative to some initial fixed axis was determined with the help

of a light emitting diode - photo sensitive diode combination. This diode circuit generated a short duration square pulse, every time a silver graduation passed by it and triggered the data acquisition system. The voltage readings corresponding to radial movements of the LVDT probe were recorded with this setup at 140 points around the circumference. These measurements were repeated at different axial locations along the specimen.

Referring to Figure 2.2 the data obtained with each circumferential scan could be interpreted as giving the outer radius of the tube $R(\theta)$ as a function of the angular position θ.

$$R(\theta) = R(0) + (V(\theta) - V(0))K \tag{2.1}$$

where

$$
\begin{aligned}
R(0) \quad &= \text{Zero setting position of the LVDT probe} \\
V(\theta) \quad &= \text{Voltage output at angular position } \theta \\
K \quad &= \text{Calibration constant of LVDT (inches (cm)/volt)}
\end{aligned}
$$

The measured data $R(\theta)$ was then fitted with a Fourier series as

$$R(\theta) = A_o + \sum_{n=1}^{m}(A_n \sin n\,\theta + B_n \cos n\,\theta) \ . \tag{2.2}$$

Since the collapse behavior of long tubes is studied, the most significant imperfection is the two wave imperfection. Here it is termed ovality and is quantified in two ways by $\Delta_o{}' = (D_{max} - D_{min})/2D$ or by the amplitude of the second harmonic in the fitted Fourier series $\Delta_o{}'' = 2(A_2^2 + B_2^2)^{1/2}/D$. If ovality has to be quantified in the field, then the first measure given by $\Delta_o{}'$ is easier to obtain. In the event that the tube section has only a two wave imperfection, the above two definitions coincide.

The term $A_1 \sin\theta + B_1 \cos\theta$ represents the rigid body part, which is an error in the data for $R(\theta)$. This error was due to the axis of rotation of the tube being different from the axis of the tube. This contribution was removed from $R(\theta)$ and the true initial deviation from circularity was obtained. Other errors in the measurements could be minimized by using a pointed probe

and by making sure that it was directed towards the axis of rotation while performing the measurements. Since these measurements were not used to construct the axial imperfection profiles of the tube, it was not necessary to establish a reference axis along the length of the specimen, relative to which the zero reading of the LVDT (for each circumferential scan) could be obtained.

Figure 2.3 gives a typical case of a measured profile and the deduced true imperfection profile. It can be seen that in this case the tube section had a predominant three wave imperfection. These measurements were taken at 5 to 10 locations along the length of each specimen. The variation of imperfection profile and ovality along the length of the specimen as observed in a typical case is given in Figure 2.4. In this figure, imperfection profiles at 5 locations along the length of the specimen are given in which the Section 0 is the tube midsection and any two successive sections are separated by a distance of 4 inches (10 cm).

In Tables 1-8, the initial ovality measures $\Delta_o{'}$ and $\Delta_o{''}$ for each of the tubes tested are also given. These values correspond to sections nearest to where the collapse pattern appeared, for which circumferential scans were taken. It was observed that, in most of the test specimens, the collapse pattern appeared close to that section which gave the largest initial ovality value. These measurements showed that the initial ovality of the tubes tested was quite small. The closeness of the two measures $\Delta_o{'}$ and $\Delta_o{''}$ suggest that the tube section had a predominantly two wave initial shape. Some of the specimens showed initial shapes corresponding to higher wave numbers and this is illustrated by differing $\Delta_o{'}$ and $\Delta_o{''}$ measures. The data also showed that the ovality variation along the length on any test specimen was fairly small.

2.1.2. *Material Property Testing.* Tensile specimens were machined from both ends of each tube in the lot from the supplier. The setup as shown in Figure 2.5 was used to pull each specimen up to 3% strain (at a strain rate of ~ 10^{-5} per second), and the stress-strain behavior was recorded. A comparison between results obtained with strain gages (0.09 inch gage length) and an extensometer (1 inch gage length) on the same specimen is shown in Figure 2.6. At strain levels below 0.5%, where yielding occurs, the two curves were found to be very close to each other. At higher strain levels (above 1%), the difference seems to increase. Due to possible slip of bond between the strain gage and specimen, the data from the extensometer

should be considered to be more reliable at higher strain levels. This data also showed that the extensometer could be reliably used for the testing of material properties, especially the yield behavior, the most important part of the analysis comparison. Once this reliability was established, most of the stress-strain tests were carried out using the extensometer.

The 304 stainless steel and aluminum 6061-O materials showed a smooth stress-strain behavior. Each of these experimental curves could be well fitted with a 3 parameter Ramberg-Osgood relation defined by

$$\varepsilon = \frac{\sigma}{E} \left[1 + \frac{3}{7} (\frac{\sigma}{\sigma_y})^{n-1} \right] . \qquad (2.3)$$

The parameters E - Young's modulus, n - hardening parameter, σ_y - Ramberg-Osgood yield stress were obtained from a least square fit. Figures 2.7a and 2.7b present experimental stress-strain curves with the best Ramberg-Osgood fit. The material properties of the various tubes tested are listed in Table 9.

For higher strains, well above the 2% - 3% level, a modified fit [16] was used for the 304 stainless steel material. In this modified fit, which is illustrated in Figure 2.8, the Ramberg-Osgood fit is used up to a strain of 1.5%. Above this 1.5% strain level, the stress-strain curve is approximated with a straight line which is tangential to the Ramberg-Osgood fit that ends at a strain of 1.5%. The slope of this straight line part is given by

$$\frac{d\sigma}{d\varepsilon} = \frac{E}{\left[1 + \frac{3n}{7} (\frac{\sigma'}{\sigma_y})^{n-1} \right]} \qquad (2.4)$$

where $\sigma' = \sigma|_{\varepsilon = 1.5\%}$ For higher strains, the modified fit approximates the stress-strain behavior of the material much better than the Ramberg-Osgood fit.

If the tube material is isotropic then a stress-strain curve obtained from an axial tensile specimen as described above will completely characterize the material. Very often manufacturing processes, such as rolling and drawing render the tube anisotropic. This will

show up as a different yield behavior in the axial and hoop directions. A simple way of characterizing these anisotropies was developed in Reference 31. In Appendix B, the measuring and modeling of these anisotropies is described in detail.

2.1.3. *Collapse Testing.* A series of collapse tests were conducted using seamless, cold drawn, 304 stainless steel and 6061-O aluminum tubes. Small diameter tubing which covered a D/t range of 10 to 40 was used for the tests. 304 stainless steel material was chosen because of its commercial availability and its similarity to the material behavior of typical pipe line grade steel. The annealed 304 stainless steel that was used showed very high ductility and it was found to creep at high stress levels. The 6061-O aluminum material was chosen for its relatively low tendency to creep and its better isotropic characteristics with respect to yielding. These tests gave a data base for correlation with analysis on the collapse of thick walled pipes under combined loading.

A picture of the test specimens is given in Figure 2.9, and the schematic of a test specimen is shown in Figure 2.10. The specimen consisted of an appropriate length of the tubing bonded to end plugs with high strength epoxy (such as the CYANAMID BR 38 & BR 95 adhesives). This resulted in a length of about 20 times the diameter of free tube between the end plugs. These end plugs were designed to give proper gripping in applying axial tension to the tubes.

The threaded plug "a" bonded to one end of the tube connected with the pressure chamber (see Figure 2.10). The plug "b" at the other end had a projecting surface of very fine surface finish, for sealing purposes. These end plugs slide-fitted into the tubes with sufficient clearance for making the epoxy joints, and they were reusable. They were separated from the specimen after the collapse test by heating with a welding torch and burning the epoxy at the joints.

The part of the end plug "b" that projected from the tube had the same diameter as the tube itself in each specimen. This helped to avoid any axial loading of the tubes through the applied external pressure.

The test chamber consisted of a thick cylinder with end caps as schematically shown in Figure 2.11. End cap "A" had internal threads that connected with plug "a". End cap "B" had a through hole of very fine surface finish and also the grooves for the seals. When assembled

only the end plug "b" projected out of the pressure chamber through end cap "B". To deal with the high testing pressures, very close tolerances were provided between plug "b" and end cap "B". "O" rings with teflon backup rings were used for sealing purposes. Face seals were also accommodated at the threaded joints between end caps "A" and "B" and the cylinder.

The testing procedure started with careful thickness and diameter measurements of the tube, before bonding in the end plugs. This was followed by imperfection measurements at 5 to 10 locations along the length of the specimen. The average thickness and diameter values along with the initial ovalities for each of the tubes tested are also listed in Tables 1-8. A series of collapse tests which involved two different loading paths were conducted. The loading path in which the specimen was first subjected to a given axial tension and then pressurized until collapse is denoted by T→P (see Figure 2.12). The other loading path used, consisted of loading the specimen to a certain external pressure and then increasing the axial tension until collapse is denoted by P→T (see Figure 2.12). Some tests using initially ovalized tubes to study the sensitivity of collapse strength to initial ovality were also carried out.

The experimental setup is schematically represented in Figure 2.13. The pressure chamber stands vertically in the setup (see Figure 2.14). A hydraulic cylinder fixture was used to pull the specimen from the top. A 62- Series Moog Servovalve system was used to manipulate the axial loading. A picture of the servo-hydraulic system is shown in Figure 2.15. A diaphragm type pump (see Figure 2.16) driven by high pressure air was used to pressurize the chamber. A synthetic fluid-water mixture was used as the pressurizing fluid to minimize any rusting. The bleed valve was initially kept open as the fluid was pumped in to remove all air. For tests involving the loading path P→T, an accumulator was used in series with the pump to keep the pressure steady (see Figure 2.16).

For collapse tests involving initially ovalized tubes, the specimens were crushed between 2 parallel plates of a press (see Figure 2.17) to induce the initial ovality. The loading plates had a dimension of about 14 diameters, and the induced ovality on test specimens varied in the range of 0.05% to 4.0%.

In the second test series with 6061-O aluminum tubes, strain gages were used to measure circumferential and axial strains at suitable locations on the specimen. Film type strain gages of 0.25 inch gage length were used for this purpose. A picture of a test specimen with the strain gages attached is shown in Figure 2.18. The locations for these gages were chosen in accordance with the initial imperfection profile on the specimen. A coating was applied on the strain gages for proper insulation from the pressurizing fluid during the collapse test. This coating had a soft and rubber like consistency, so that its strengthening effect on the tube was minimal. The pressure chamber was modified for this test series to run the lead wires attached to the gages from inside the chamber to the outside through a connector to prevent any leakage during pressurization. Since the strain gage response is sensitive to lateral pressure, it was calibrated, and a correction was applied to all the strain gage readings. This calibration is given in Figure 2.19, and it suggests that, for the pressure range of interest, the sensitivity to lateral pressure of the gages used is small.

Collapse of the tube was characterized by a sudden drop in the pressure. Axial elongation of the tube during loading was measured with an LVDT. A data acquisition system was used to monitor and record axial tension, pressure, axial elongation and strain gage readings until collapse. Results from a typical collapse test are given in Figures 2.20a and 2.20b. The results of these collapse tests are tabulated in Tables 1-8. The data is also plotted in Figures 4.3-4.5,4.8-4.9 with appropriate normalization.

2.2. Experimental Results and Discussion.

The collapse strength of a number of tubes under biaxial loading was obtained using the procedure described in the earlier section. 45 test specimens of 304 stainless steel material, with a D/t range of 10 to 40 were tested applying the loading path T→P. The testing procedure was such that further loading was stopped when collapse was detected through a sudden drop of pressure. This left a local collapse pattern, (see Figures 2.21 and 2.22), which extended over a length of about 3 to 5 diameters. It was observed that for most of the specimen the collapse pattern appeared close to the location which had the maximum initial ovality. Specimen of lower D/t values tested at very high axial tensile loads, showed no collapse failure within the load-displacement capability of the test setup. These data points are referred to as

experimental points with no collapse in Tables 3 and 4. The loads reported in these cases correspond to the highest ones at which the axial elongation reached the maximum value that was possible in the setup. Also, the initial ovalities given for these data points are the maximum values observed along the length of tube.

In the collapse data for 304 stainless steel tubes of $D_o/t = 18.2$, given in Table 3, the experimental point that represents the no collapse point registered a pressure which is much higher than the collapse pressures corresponding to slightly lower tensile loads. Other experimental results obtained in this study as well as the results from the model studies suggest that for the materials considered, such a substantial increase in pressure withstanding capability when tension is slightly increased is unreasonable. During the experiments involving high tensile loads, tubes of low D/t showed a pronounced tendency to elongate axially under increasing pressure. It is suspected that during this experiment, due to large axial elongation of the specimen, some interference occurred between the tube part of the specimen with the seals and the end cap B (see Figures 2.10 and 2.11). This would result in increased frictional resistance between the specimen and the pressure chamber. If this had in fact happened, the tube would experience axial unloading with the total tensile load taken by the specimen remaining the same. With a sufficient reduction in the tensile load on the tube, it would be able to withstand much higher external pressure.

In a second series of experiments, 13 tests were conducted on initially ovalized tubes of $D_o/t = 27$ and 304 stainless steel. The loading path used was T→P. The specimen were crushed between two parallel plates in a hydraulic press, to induce the initial ovality. The results are given in Tables 5,6 and Figures 4.8-4.9. These results clearly show the detrimental effect of initial ovality on the collapse strength. The initial ovalities reported for the above two series of experiments correspond to axial locations nearest to where the collapse pattern appeared, for which circumferential scans were available.

A third set of 7 collapse tests were conducted with 304 stainless steel tubes of $D_o/t = 27.2$ applying the loading path P→T. An accumulator was used in series with the pump to keep the pressure steady while increasing the axial tension. This resulted in the collapse pattern extending over the full length of the specimen (see Figure 2.23). The initial ovality reported for

these tests corresponds to the maximum value observed along the length of the tube. These tests were carried out to study the effect of loading path on the tension-pressure collapse envelope. The experimental results for the two loading paths, as well as the theoretical predictions, show that the effect of load sequence on collapse is not significant. These results are given in Table 7 and Figures 4.5a, 4.5b.

Another set of experiments with 6061-O aluminum tubes was conducted applying different loading paths. Since this material had a low yield stress and modulus compared to 304 steel, the measured collapse pressures were much lower. By using strain gages the strain response of the specimen at different locations of interest could be measured until collapse. These results are used to study the circumferential strain (and hence the displacement) behavior with load and to check how uniformly the specimen is deforming along the length. The load-strain response thus measured could be used to compare with the predictions from the model (see Figures 4.12 and 4.13). The collapse data for the Aluminum tubes are given in Table 8. In Figures 4.11a and 4.11b, the experimental results for the collapse envelopes for $D_o/t=12.2$ are compared with the theoretical predictions.

For each long tube in the lot from the supplier, tensile coupons were cut out from either end of the tube. 4 to 6 stress-strain tests were conducted for each tube. The average values of material parameters from these stress-strain curves from each tube is termed a material group. The various material groups are listed in Table 9. This shows how material parameters for cold drawn tubes of the same material and heat treatment can vary.

Tests were conducted on some of the tubes to characterize the anisotropic parameters. The details of these test procedures are given in Appendix B. The results of these tests are also given in Table 9. They show that for cold drawn tubes the anisotropy can be very significant.

All the axial tensile data reported in Tables 1-8 were subjected to a frictional correction. Figure 2.24 shows a schematic of the setup used to measure the frictional resistance at the seals, through which the test specimen projected out of the pressure chamber. A certain length of tube was bonded with end plugs of type "a" (see Figure 2.10) at both ends. The force required to slide this specimen through the seals at a slow and steady rate was measured for a wide range

of pressures. The seals used consisted of "O" rings made of a very hard type of rubber and teflon backup rings. This combined with the very fine gap between the sealing parts allowed for very little extrusion of the seals under increasing pressure. Hence, the frictional force measured was found to fluctuate within 10% variation for the range of pressures tested. These measurements were repeated to verify the range of these fluctuations and finally an average value of the force measured was applied as a frictional correction.

Chapter 3

ELASTIC-PLASTIC COLLAPSE: FORMULATION AND PREDICTED RESULTS

The problem studied here is the instability of long tubes under external pressure and axial tension. For tubes of D/t range 10-40, the collapse strength under biaxial loading is strongly influenced by the initial geometric imperfections and the yield behavior. A two dimensional formulation of the problem is given here. This effort is an extension of the previous work done on the problem of inelastic collapse under external pressure [8,16,30]. The numerical scheme developed in [30] is used here. Some of the details on the formulation and numerical implementation are given in Appendix A.

3.1. Problem Formulation.

The analysis models a long tube of mean radius R_o and mean wall thickness t, under external pressure P and axial tension T (see Figure 3.1a). The most significant imperfection for a long tube which collapses into a two wave mode under load is the two wave imperfection called the ovality. The imperfection profiles measured, showed a predominant two wave mode shape on most of the specimens. Hence, numerical results are obtained for a tube of initial geometry which includes an ovality defined by $\dfrac{R_\theta}{R_o} = (1 - \Delta'_o \cos 2\theta)$ (see Figure 3.1b). However, any initial geometric imperfection of the tube could be included in the numerical analysis with minor modifications. The tube considered is under generalized plane strain conditions, and the initial ovality $\Delta'_o = \dfrac{w_o}{R_o}$ is not allowed to vary along the length of the tube. The formulation is general enough to model the effect of anisotropic material behavior on collapse strength. The effect of residual stresses (in the initial configuration of the tube), on the collapse strength can also be studied with this model.

A principle of virtual work type procedure is applied here to derive the nonlinear equilibrium equations. These equations are then solved using the Newton-Raphson method. For a tube with initial geometric imperfections, a limit load type of behavior characterizes the response. In this case, the equilibrium load-displacement profile is solved using an incremental

procedure, and the limit load is taken as the critical load. A tube having a perfect initial geometry would exhibit a bifurcation instability.

3.1.1. *Constitutive Relations*. To study the collapse behavior of thick tubes with a D/t range of 10-40, it is important to properly model the inelastic behavior of the material. In general, the load paths followed by the material points in the tube cross section under biaxial loading are not proportional. Hence, an incremental method is incorporated to solve the equilibrium equations which represent a two-dimensional state of stress. Only the axial stress, σ_x, and the circumferential stress, σ_θ, are included, and the radial stresses are neglected.

Very often tube manufacturing processes, such as rolling and drawing, introduce anisotropies in the tube. These will show up as differing yield behavior in the axial and hoop directions. A simple way to characterize these anisotropies was developed in Reference 31. The effect on collapse strength by such anisotropies is modeled with Hill's anisotropic plasticity theory. In this theory, the yield function represents an initially anisotropic yield surface uniformly expanding [32].

In this framework the yield function is given by

$$f(\sigma_{ij}) = \left\{ \sigma_x^2 - (1 + \frac{1}{S_\theta^2} - \frac{1}{S_r^2})\sigma_x \sigma_\theta + \frac{1}{S_\theta^2} \sigma_\theta^2 \right\}^{1/2} = \sigma_{e,max} \quad , \quad (3.1)$$

where $S_\theta = \dfrac{\sigma_{o\theta}}{\sigma_{ox}}$ and $S_r = \dfrac{\sigma_{or}}{\sigma_{ox}}$ are the anisotropic parameters. $\sigma_{e,max} = \sigma_{e,max}(\varepsilon_e^p)$ is the maximum value of σ_e in (4.9), and $\sigma_{e,max}$ is made to go along the uniaxial stress-strain curve in the axial, (x), direction.

The appropriate definitions for equivalent stress and plastic strain increments [32] are given by

$$\sigma_e = \left\{ \sigma_x^2 - (1 + \frac{1}{S_\theta^2} - \frac{1}{S_r^2}) \sigma_x \sigma_\theta + \frac{1}{S_\theta^2} \sigma_\theta^2 \right\}^{1/2} \quad (3.2)$$

and

$$d\varepsilon_{ij}^p = \frac{1}{H} \left[\frac{\partial f}{\partial \sigma_{mn}} d\sigma_{mn} \right] \frac{\partial f}{\partial \sigma_{ij}} \qquad . \tag{3.3}$$

An expression for the equivalent plastic strain increment can be obtained from the work equality $\sigma_e d\varepsilon_e^p = \sigma_{ij} d\varepsilon_{ij}^p$.

The relation between stress and strain increments is given by

$$\left\{ \begin{array}{c} d\varepsilon_\theta \\ d\varepsilon_x \end{array} \right\} = \left[\begin{array}{cc} \dfrac{1}{E} + \dfrac{\Lambda B^2}{H\Sigma} & \dfrac{-v}{E} + \dfrac{\Lambda AB}{H\Sigma} \\[2mm] \dfrac{-v}{E} + \dfrac{\Lambda AB}{H\Sigma} & \dfrac{1}{E} + \dfrac{\Lambda A^2}{H\Sigma} \end{array} \right] \left\{ \begin{array}{c} d\sigma_\theta \\ d\sigma_x \end{array} \right\} \qquad , \tag{3.4}$$

where

$$A = 2\sigma_x - (1 + \frac{1}{S_\theta^2} - \frac{1}{S_r^2})\sigma_\theta$$

and

$$B = \frac{2}{S_\theta^2} \sigma_\theta - (1 + \frac{1}{S_\theta^2} - \frac{1}{S_r^2})\sigma_x \qquad .$$

H is derived from a uniaxial stress-strain curve in the axial (x-axis) direction as

$$H = \frac{d\sigma_x}{d\varepsilon_x^p} \qquad ,$$

$$\Sigma = 4\sigma_e^2$$

and

$$\Lambda = 0 \quad \text{if} \quad f(\sigma_{ij} + d\sigma_{ij}) - \sigma_{e,max} < 0$$
$$\Lambda = 1 \quad \text{if} \quad f(\sigma_{ij} + d\sigma_{ij}) - \sigma_{e,max} = 0 \qquad .$$

For the current load step, the stress and strain increments induced are found iteratively by applying the equation (3.4). In applying this constitutive model, one needs to know the stress-strain behavior of the tube in the axial direction along with the anisotropic parameters S_θ and S_r to completely characterize the tube material. By giving a value of unity to S_θ and S_r, the above plasticity model reduces to the classical J_2 theory with isotropic hardening.

Experiments to characterize the anisotropic parameters were carried out for some of the tubes. Some of the details on the experimental procedure and the interpretation of the data are given in Appendix B. The results from these tests (see Table 9) showed that the values for the parameters S_θ and S_r are very nearly equal.

3.2. Numerical Results.

It has been shown that a two-dimensional model with an anisotropic formulation is feasible. The experimental data base, obtained with procedures explained in the previous chapters, verifies the suitability of the analysis. The radial stresses and shear strains in the tube cross section are neglected in the formulation. These are the usual shell theory assumptions, and it has been shown that this results in relatively small errors. For example, it is shown in Reference [33] that the effect of neglecting shear strains on the collapse of an elastic ring under external pressure is less than 5% for D/t as small as 10.

The response of a tube of perfect circular section is characterized by a bifurcation point. Presence of initial geometric imperfections in the form of thickness variations and initial ovality change the response to a limit load type of behavior. The effect of thickness variations up to 10% of mean wall thickness on the collapse strength (under external pressure) is shown to be insignificant in Reference 30. The thickness variations measured on the test specimen were less than 5% of the mean wall thickness. The measured initial imperfection profiles show that most of the specimens have a predominant two wave mode shape. Hence, numerical results were obtained, considering only the initial ovality imperfections. Collapse strength is found to be highly influenced by the initial ovality of the tube, and the analysis is capable of modeling this effect. In Figures 3.2a and 3.2b, the limit point load-displacement behavior as predicted by this model for a typical case is given. These figures also illustrate the interaction between axial tension and pressure, the extent of which depends on the material and geometric properties of

the tube.

The variations of geometric and material properties along the axial direction are not considered in this analysis. For a long string of tubing sitting on the ocean floor, a two dimensional formulation based on the assumption of generalized plane strain conditions seems to be very reasonable. In chapter 5, an assessment of the importance of various material and geometric parameters is given.

Chapter 4

COMPARISON OF EXPERIMENTAL RESULTS AND NUMERICAL PREDICTIONS

The solution procedure described in the previous chapter is used to predict the collapse strength, for correlation with the experimental results. For convenience, the experimental results are divided into seven groups. For each of these groups, analytic predictions based on average material and geometric parameters were obtained. For those groups of tests for which no anisotropic measurements were carried out, an average value was assumed for the anisotropic parameters ($S_\theta = S_r = 0.85$) to get the anisotropic predictions. In Figures 4.1-4.5, 4.8-4.9 and 4.11, predictions based on isotropic and anisotropic material behavior are correlated with experimental results. The material and geometric parameters used for the predictions are referred to by a group number (S1-S8) in these figures. These eight parameter groups used in the predictions are listed in Table 10. The anisotropic parameters used to obtain these predictions are given in the figures.

In Figures 4.1-4.4, results for the loading path T→P for four different D_o/t (304 steel) are given. In spite of using average material and geometric parameters, there is good agreement between the predicted and experimental collapse envelopes. Predictions for the tension-pressure collapse envelopes, based on the anisotropic formulation, are in better agreement with the experimental results. The 304 stainless steel material was found to creep during the experiments in which the loads were high enough to yield the material. Tubes of D_o/t values 18.2 and 12.2 showed no experimental collapse at high tensile loads within the displacement capability of the test setup. The agreement between experimental and predicted axial strain values at collapse was found to be very good for higher D_o/t tubes. For tubes of lower D_o/t, experimentally obtained axial strains were found to be higher than the predictions. Some of this discrepancy could be attributed to the creep behavior shown by the 304 steel, and this has been established through a model study in Chapter 6.

Figures 4.2a and 4.3a give the tension-pressure collapse results for D_o/t=24.5 and D_o/t=18.2. It is observed that at higher axial loads, (above $T_c/T_o' = 0.9$ for D_o/t=24.5 in

Figure 4.2a and above $T_c/T_o' = 0.8$ for $D_o/t = 18.2$ in Figure 4.3a), experimental collapse pressures are not significantly affected by increasing the axial tension. The theoretical predictions given in Figures 4.2a and 4.3a do not show such a flat collapse pressure-tension behavior at higher axial loads. These predictions are obtained by using Ramberg-Osgood representation for the stress-strain behavior of the material. From Figure 2.8, it can be seen that the Ramberg-Osgood fit does not give a good approximation of the stress-strain behavior for 304 steel at higher strains. The modified fit given in Figure 2.8 approximates the stress-strain behavior better than the Ramberg-Osgood fit at higher strains. Hence, predictions for tension-collapse pressure interaction curves were obtained with the modified fit representation of the stress-strain behavior. In Figure 4.2c, the experimental results compared with predictions based on Ramberg-Osgood fit and Modified fit representations for the stress-strain curve are shown. It is observed that, (see Figure 4.2c), the tension-pressure collapse envelope predicted with the modified fit follows the shape of the experimental profile better. These results also suggest that the shape of the tension-collapse pressure profiles are very sensitive to the shape of the stress-strain curves.

In Figures 4.5a, 4.5b, results for the loading path P→T for a $D_o/t = 27.2$ (304 steel) are given. Predictions given in these figures are based on average material and geometric properties of the tubes. Predicted tension-pressure collapse envelope based on the measured anisotropies compares better with the experiments (see Figure 4.5a). Experimental results correlated with predictions based on the two loading paths are given in Figures 4.6, 4.7. The experimental results given in these plots are obtained from specimens which had initial ovalities in the range 0.0002-0.004 (see Tables 3, 7). These results show that, for tubes of lower initial ovalities, collapse envelopes are hardly affected by changing the loading paths.

For the two groups of tests involving ovalized tubes (304 steel), the predictions compared with the experimental results (given in Tables 5, 6) are shown in Figures 4.8-4.9. Collapse pressure predictions based on anisotropic material behavior are found to be very good (see Figures 4.8a, 4.9b). The agreement shows that the high sensitivity of the collapse strength to imperfections is modeled reliably by this analysis. From the Figures 4.8a and 4.9a, one can see that an ovality of 1% reduces the collapse strength by 40% for both high and low axial tensile

loads tested.

Initial studies, using a constitutive model which can handle different values for S_θ and S_r showed that collapse strength is more sensitive to S_θ than S_r. It can be noted from Table 9 that the values measured for S_θ and S_r are either equal or very nearly equal. In the predictions for the experiments involving those material groups with slightly differing S_θ and S_r, it was assumed that S_r was equal to the measured S_θ value.

An assessment of the current API design formula for collapse strength under combined pressure and tension is given in Figure 4.10. The tension-pressure collapse envelope represented by this formula consists of a polynomial fit between the lowest predictable collapse pressure and the yield tension. For clarity, a value for collapse pressure in the API formula was assumed to be the basic collapse pressure (zero axial tension) from the model. Figure 4.10 clearly illustrates how this API estimate becomes conservative at higher tensile loads.

Experimental results for 6061-O aluminum tubes are given in Table 8 and Figures 4.11-4.13. In Figures 4.11a and 4.11b, the correlation between experimental collapse envelope and predictions based on the two loading paths is given. The tension-pressure collapse profiles given in Figure 4.11a support the earlier conclusion that the effect of load sequence on collapse is not very significant. The agreement between experimental and predicted axial strain response at collapse for 6061-O tubes of D_o/t=12.2 is found to be good (see Figure 4.11b). A similar comparison for 304 steel tubes of D_o/t=12.2 shows a large discrepancy between experimental and predicted axial strain response at collapse (see Figure 4.4b). The improved agreement between experimental and predicted tension-axial strain at collapse profiles (see Figure 4.11b) for 6061-O tubes of D_o/t=12.2 is attributed to the relatively low tendency of 6061-O material to creep.

The pressure-hoop strain response obtained in two cases is given in Figures 4.12 and 4.13. In the first case, results for a 6061-O tube of D_0/t=21.4 that showed very small variations of the imperfection profiles along the length are given. In the second case, a 6061-O tube of D_o/t=12.2 that showed a relatively large variation of the imperfection profile along the length is chosen to illustrate the pressure-hoop strain results. The strain measurements were obtained

using strain gages of gage length 0.25 inches.

The following designation for the locations on the tube surface is chosen to better represent the results. Referring to Figure 3.1b, the location corresponding to angle $\theta = 90^o$ or $\theta = 270^o$ is denoted by θ_{max}. The location corresponding to $\theta = 0^o$ or $\theta = 180^o$ is denoted by θ_{min}. These two locations, θ_{max} and θ_{min}, represent the circumferential points of interest in the hoop strains-pressure measurements. For the geometry of interest, a local collapse pattern (see Figure 2.22) extends over a length of 3-4 diameters (4-5 inches). The axial location corresponding to the middle section of a local collapse pattern is denoted by "L". A location which is "x" inches to one side of "L", along the length of the tube is designated by "L+x". A point "x" inches to the other side of "L" is denoted by "L-x".

In Figures 4.12a, the comparison between measured and predicted hoop strain-pressure response at axial location "L" and circumferential locations θ_{max} and θ_{min} for a tube of $D_o/t = 21.4$ is given. For this tube of $D_o/t = 21.4$, a well defined limit point type of pressure-hoop strain behavior could not be measured due to some problems with data acquisition. The agreement between measured and predicted response is reasonable, with the model over predicting the collapse pressure by more than 30% (see Figure 4.12a). In Figure 4.12b, the strain response for different axial locations at the circumferential position θ_{max} is given in comparison with the theoretical prediction. The initial ovality measured at each of the axial locations is also given in Figure 4.12b. It is observed that (see Figure 4.12b) the variation in the initial ovality along the axial direction is negligible. The agreement between the measured hoop strain-pressure response at different axial locations is good (see Figure 4.12b).

In Figure 4.13a, the measured hoop strain-pressure response for axial location "L" and circumferential points θ_{max} and θ_{min} for a tube of $D_o/t = 12.2$, is compared with the predictions. The measured strain response given in Figure 4.12a clearly illustrates the limit point type of behavior shown by initially imperfect tubes. Measured strain response for different axial locations at the circumferential position θ_{max} is given in comparison with the theoretical prediction in Figure 4.13b. The initial ovalities corresponding to different axial locations reported in Figure 4.13b suggest the relatively larger variation of the initial imperfection profiles along the length of the tube. The measured strain responses at different axial locations

(see Figure 4.13b) suggest that the pressure-hoop strain response is very sensitive to the initial imperfection profile. These results (see Figures 4.12-4.13) also suggest that for a tube of relatively small variation of initial imperfection profiles along the length the assumption invoked in the two-dimensional model, that the tube ovalizes uniformly under the action of the loads, is reasonable.

Chapter 5

PARAMETRIC STUDY

The solution procedure that was developed and the various assumptions that were involved are described in detail in Chapter 3. In this section, a parametric study is conducted to establish the sensitivity of collapse strength to various material and geometric parameters. A tube of $D_o/t=18.2$ was chosen for obtaining the numerical results.

5.1. Initial Ovality.

Collapse strength is found to be highly sensitive to initial geometric imperfections of the form of an ovality. Load-displacement responses under combined loading for different initial ovalities are given in Figures 5.1a, 5.1b. In Figure 5.1a, the pressure-displacement response for a tube of $D_o/t = 18.2$, under a loading path of $T \rightarrow P$ is shown. The tension-displacement response of the same tube for a loading path of $P \rightarrow T$ is given in Figure 5.1b. These Figures illustrate how the limit load (which represents the collapse strength) is lowered when the initial ovality imperfection is increased.

For example, one can see from Figure 5.1a that the limit pressure is reduced by 25% when the initial ovality is increased from 0.0008 to 0.01. For a tube of $D_o/t = 18.2$, under the loading path $T \rightarrow P$, the collapse pressure-initial ovality dependence is illustrated in Figure 5.2. The results, plotted in Figure 5.2, clearly show the detrimental effect of initial ovality on collapse strength under combined loading. These results also suggest that the rate at which collapse pressure reduces with initial ovality (slope of the collapse pressure-ovality curve) decreases with increasing initial ovality. From the Figure 5.2, one can see that for low initial ovality imperfections (for Δ_o' less than 0.005) this rate is higher at higher axial tension. For higher initial ovality imperfections (for Δ_o' above 0.01), this rate is lower at higher axial tension. The results shown in Figures 4.8a and 4.9a for tubes of $D_o/t=27$, also suggest similar behavior.

The sensitivity of collapse strength to initial ovality imperfections depends also on the geometric parameter D/t. Predicted collapse pressures (T=0) for tubes from a range of D/t

values for 3 different values of initial ovalities are plotted in Figure 5.3. These results show that thinner tubes are more sensitive to initial ovality imperfections than thicker tubes in the D_o/t range 10-40. For example, one can observe in Figure 5.2 that by increasing the ovality from 0.0008 to 0.03 the collapse pressure for a tube of D_o/t =40 is reduced by 51%. Whereas for a tube of D_o/t=18.2 and same material properties the collapse pressure is reduced only by 40%.

5.2. Material Parameters.

Collapse strengths are obtained by varying the material parameters n - the hardening parameter, σ'_o - the yield stress and S_θ, S_r - the anisotropic parameters. Stress-Strain Curves as represented by the Ramberg-Osgood Fit for three different values (n=5.0, 10.0, 40.0) of the hardening parameters are given in Figure 5.4. Stress-Strain representation for n=5.0 in the Figure 5.4, can be be interpreted as the behavior of a brittle material. On the other hand, the curve for n=40.0 typically stands for a very ductile material. Collapse pressures (T=0) for these three stress-strain curves for a range of D/t values are plotted in Figure 5.5. For clarity, the collapse pressures are plotted in their absolute values (psi). It is observed (see Figure 5.5) that collapse pressures for relatively thinner tubes (D_o/t above 20) are not significantly affected by chosing these three stress-strain representations. Relatively thicker tubes (D_o/t below 20) are more affected by this choice , with the stress-strain represented by n=5.0 giving a higher collapse pressure. In Figure 5.6, tension-pressure collapse envelopes for the three different n values are given. Absolute values of the collapse pressures are used in this plot. These results illustrate how the collapse envelope is affected by the shape of the stress-strain curves. From Figure 5.6, one can observe that by having a material of high hardening parameter collapse strength is more affected by axial tension.

For thicker tubes, σ'_o, the yield stress, turns out to be the most important material parameter. Stress-Strain curves for three different yield stresses are shown in Figure 5.7. Predicted collapse pressures for these three different stress-strain behaviors , for a range of D/t, are plotted in Figure 5.8. These results show that collapse strength of thicker tubes are more affected by changing the yield stress. The effect of varying the yield stress on the tension-pressure collapse envelope is illustrated in Figure 5.9.

The constitutive model used is the Hill's anisotropic plasticity theory. In this model, anisotropy is characterized by two parameters S_θ and S_r. By giving a value of unity to S_θ and S_r, the above plasticity model reduces to the classical J_2 theory with isotropic hardening. Collapse pressures for a range of D/t, for three sets of $S_\theta = S_r$ values are given in Figure 5.10. These results suggest that by changing the anisotropic parameters which effectively changes the yield stress collapse strength of thicker tubes are more affected. Predicted tension-pressure collapse envelopes for three sets of $S_\theta = S_r$ values are plotted in Figure 5.11. Figure 5.12 illustrates the sensitivity of collapse pressure to $S_\theta = S_r$ values.

5.3. Residual Stresses.

Manufacturing processes which do not involve complete annealing leave residual stresses in the tube. If a small length of the tube is taken and cut open axially, the presence of residual stresses will show up as an opening or closing up tendency of the tube. The exact nature of the residual stress distribution depends on the type of manufacturing process involved.

A parametric study was conducted assuming the elasticity solution of pure bending of a curved bar [34] for the residual stress distribution. The hoop stress distribution is given by

$$\sigma_\theta = -4k \left[-\frac{R_i^2 R^2}{r^2} \ln(\frac{R}{R_i}) + R^2 \ln(\frac{r}{R}) + R_i^2 \ln(\frac{R_i}{r}) + R^2 - R_i^2 \right] \quad , \quad (5.1)$$

where $R_i \leq r \leq R$, $R_o = R - t/2$ and k is a constant.

The maximum value of σ_θ appears on the tube inner wall ($r = R_i$) given by

$$\sigma_R = -4kR_i^2 \left[(\frac{R}{R_i})^2 - 2(\frac{R}{R_i})^2 \ln(\frac{R}{R_i}) - 1 \right] \quad , \quad (5.2)$$

σ_R is referred to as the bending residual stress at the tube inner wall. In the parametric study, σ_R is varied, and the stress distribution is obtained from the above equations. In the solution procedure, these are treated as the initial stresses in the tube cross section.

Collapse stress sensitivity to σ_R for different D/t is well illustrated by Figure 5.13. These results suggest that for tubes of lower D/t values, the effect of residual stresses is insignificant.

In Figures 5.14 and 5.15, tension-pressure collapse envelopes predicted by including residual stresses are given. They (see Figures 5.14, 5.15) show that the effect of including residual stresses becomes negligible at higher tensile loads.

5.4. Loading Path.

For tubes of lower initial ovalities considered, changing the loading path had little effect on the collapse envelope. The collapse envelope obtained for the loading path P→T seems to fall below the one for the load path T→P. This difference is illustrated by the results in Figures 4.6,4,7 and 4.11.

5.5. Other Parameters.

Material and geometric parameters which are not considered in the above sections have negligible influence on the collapse strength. Thickness variations up to 10% of the mean wall thickness are shown to have negligible effect on collapse strength under external pressure [30]. For the D/t range of 10 to 40 considered, collapse occurs in the post yield region of the material, and the effect of varying E, the Young's modulus, becomes less pronounced towards the lower D/t range. The effect of creep behavior of the tube material on the collapse strength is addressed in detail in Chapter 6. In essence, the effect of primary creep at room temperature on collapse strength is shown to be not very significant for the type of materials used.

Chapter 6

AN ASSESSMENT OF THE EFFECT OF PRIMARY CREEP ON COLLAPSE

Collapse of a long and thick-walled tube subjected to external pressure and axial tension, made of a material that shows elastic-plastic and primary creep behavior is addressed in this chapter. Elastic-plastic behavior is modeled with the classical J_2 incremental theory of plasticity. An equation of state approach with a power law is used to model the primary creep. A subincremental scheme has been adopted for the proper modeling of the primary creep behavior. The initial strain method is used in the numerical implementation of the creep behavior.

6.1. Introduction.

Many structural components are made of materials that show time dependent load-displacement relationship under service conditions. For most of the metals, this behavior invariably shows up at higher temperatures. Creep is a generic term that stands for this time dependence of load-displacement relationship shown by the material in a deformed body, and extensive investigations have been carried out in order to better understand and predict creep behavior. It has been realized [35] that, depending on the material, a different mechanism may be responsible for the creep behavior.

Very often it becomes necessary to carry out creep calculations, of structural components to make sure that they are failsafe in the expected service period. In the case of a long tube with initial imperfections under external pressure and tension, creep will result in increasing its non-axisymmetric deflection or ovalization with time. The objective of the following formulation is to assess the effect of primary creep behavior on the collapse strength or the load carrying capacity of the tube.

Many creep theories are in use today, and they have been reviewed by many authors: for example, Rabotnov's assessment of various creep theories [36], Nickell's survey [37] on the implementation of creep models in some of the widely used numerical codes, and Hoff's survey

[38] on the creep buckling of plates and shells. Many of the investigations in the literature on creep buckling address the problem of columns, plates and shells under axial compressive loading.

Hoff et al. [39] also studied the collapse of a thin-walled tube under external pressure. They modeled a shell of sandwich construction with initial imperfections. Their results showed growth of ovalization of the shell with time until collapse occurs after a finite time designated as the critical time. By modeling only the secondary (steady state) creep behavior, a relatively simple scheme to obtain the critical time is obtained. Some observations on the effect of initial imperfections in the form of an ovality on the critical time are also presented in Reference 39.

Bushnell [40] has implemented a scheme to analyze shells of revolution involving plasticity and creep behavior in a computer program named BOSOR. Some of his suggestions have been followed in the following formulation.

6.2. Creep Formulation.

6.2.1. *Creep Law.* An equation of state approach in which the creep strains are represented by a power law, as shown in equation (6.1), is adopted to model [40] the creep behavior. The coefficients A, m and n in the equation can be obtained through constant stress creep tests or by constant total strain relaxation tests on uniaxial specimens.

$$\varepsilon_e^c = A \ \sigma_e^m \, t_e^n \quad , \tag{6.1}$$

where ε_e^c is the equivalent creep strain as defined in equation (6.2) and t_e the effective time.

$$\varepsilon_e^c = \left[\frac{2}{3} \ \varepsilon_{ij}^c \ \varepsilon_{ij}^c \right]^{1/2} \quad . \tag{6.2}$$

6.2.2. *Flow Rule.* For relating to multiaxial states of stresses and creep strains, a flow rule very similar to the ones in plasticity theory is applied here. A yield locus, $f(\sigma_{ij})$, associated with the J_2 invariant, as given in equation (6.4), is assumed here, and the creep strain rate at any instant is taken to be normal to this yield locus. The normal to the above yield locus (equation 6.6) is proportional to the deviatoric stresses, and this results in modeling the creep

strains as incompressible. The definition for the J_2 invariant is given by

$$J_2 = \frac{1}{2} S_{ij} S_{ij} \quad . \tag{6.3}$$

By simplifying the expression for J_2, the yield locus and the equivalent stress are given by

$$f(\sigma_{ij}) = (3 J_2)^{1/2} = \left\{ \sigma_x^2 - \sigma_x \sigma_s + \sigma_s^2 \right\}^{1/2} \quad . \tag{6.4}$$

Once the equivalent creep strain rate is known, its components can be obtained as follows:

$$\dot{\varepsilon}_{ij}^c = \dot{\varepsilon}_e^c \, n_{ij} \quad , \tag{6.5}$$

where n_{ij} is the unit normal to the yield locus $f(\sigma_{ij})$ given by

$$n_{ij} = \frac{df}{d\sigma_{ij}} \Bigg/ \left[\frac{df}{\sigma_{mn}} \frac{df}{\sigma_{mn}} \right]^{1/2} \quad . \tag{6.6}$$

6.2.3. *Hardening law.* The instantaneous creep strain rates are related to the stress states through a hardening rule. Extensive studies on creep behavior in metals [36] have led to the development of the two simple hardening models, namely the strain hardening model and the time hardening model. In the strain hardening model, for isothermal cases, the creep strain rate at any instant is given by a function of the stress, σ_e, and the accumulated creep strain, ε_e^c.

$$\dot{\varepsilon}_e^c = f(\sigma_e, \varepsilon_e^c) \quad . \tag{6.7}$$

This is very similar to the hardening laws that are used in the plasticity theories. The accumulated creep strain can be considered as the strain hardening parameter.

In the time hardening model, creep strain rate is given by a function of the stress, σ_e, and time, t.

$$\dot{\varepsilon}_e^c = f(\sigma_e , t) \quad . \tag{6.8}$$

Existing results [37,38] suggest that the strain hardening model is better suited than the time hardening model for modeling creep in metals. The time hardening model is shown [37,38] to be good for modeling steady state (secondary) creep, and its functional form makes the numerical implementation very convenient. In this formulation, the strain hardening model modified [40] with an element of the time hardening approach is used. This modification made the numerical implementation more convenient, and its effect on the accuracy of the strain hardening model can be made minimal. In the subsection 6.2.6, the details of implementing this modified approach are given.

6.2.4. *Adequacy of the above creep model.* It has been shown [37,38] that, for metals, strain hardening theory performs better than other models in predicting both creep and relaxation experimental results as well as tests under step changes in stress. But, predictions based on strain hardening theory showed increasing deviation from experimental results when considerable plastic deformation occurred. This model, without proper modifications, is also not suitable if total reverse loading occurs. However, the agreement between experimental results and the predictions based on time independent constitutive theory, as described in the earlier chapters, suggest that the effect of creep on collapse strength is not very significant. This prompted the use of a simple creep law to model the less dominant creep behavior shown by materials such as 304 stainless steel for assessing the magnitude of the influence of creep. The results from this model could be seen as a first order estimate for the effect of creep on collapse strength. If the effect appeared to be large, an analysis with a more precise creep law would be essential.

6.2.5. *Subincremental Scheme.* Proper modeling of primary creep requires the use of very small time steps. If the timestep, Δt, prescribed is found to be large, it is subdivided into smaller timesteps, dt^i, through an iterative scheme,

$$\Delta t = \sum_i dt^i \quad . \tag{6.9}$$

Each subincrement is chosen in such a way that it results in a change in equivalent stress and

total strain within a certain prescribed limit as given below.

$$\frac{d\sigma_e^i}{\sigma_e^{(i-1)}} < K^\sigma$$
(6.10)

and

$$d\varepsilon_e^i < K^\varepsilon \quad ,$$
(6.11)

where $\sigma_e^{(i-1)}$ is the equivalent stress at the material point corresponding to the previous time step $(i-1)$, $d\sigma_e^i$ and $d\varepsilon_e^i$ are the changes in the equivalent stress and equivalent creep strain during the current time subincrement, dt^i. The limit values, K^σ and K^ε, are obtained through numerical convergence studies. In the examples presented in this section, these values were K^σ = 0.01-0.02 and K^ε = 0.0002-0.0005. A subincremental procedure, described as above, leads to a large number of iterations to satisfy the material behavior and thereby makes the method more reliable.

6.2.6. *Numerical Procedure.* In this framework, the incremental change in total strain at any material point during an interval dt^i consists of three components, namely the elastic, the plastic and the creep parts.

$$d\varepsilon_e^i = (d\varepsilon_e^e)^i + (d\varepsilon_e^p)^i + (d\varepsilon_e^c)^i \quad .$$
(6.12)

The plastic part is modeled with the associated J_2 incremental theory with isotropic hardening and the creep part is modeled with an initial strain method as described below.

Let dt^i be a subincrement chosen at a material point where the stress and the accumulated creep strain corresponding to the previous time step (i-1) are $\sigma_e^{(i-1)}$ and $(\varepsilon_e^c)^{(i-1)}$. From equation (6.1) for the creep law, the value for the effective time, $t_e^{(i-1)}$, can be obtained as

$$t_e^{(i-1)} = \left[\frac{(\varepsilon_e^c)^{(i-1)}}{A \, (\sigma_e^{(i-1)})^m} \right]^{1/n} \quad .$$
(6.13)

Since t_e is obtained from the accumulated creep strain, ε_e^c, it can be considered as the strain hardening parameter. During the time subincrement, dt^i, the equivalent stress and creep strain at the material point change to their new values as defined below.

$$\sigma_e^i = \sigma_e^{(i-1)} + d\sigma_e^i \quad . \tag{6.14a}$$

$$(\varepsilon_e^c)^i = (\varepsilon_e^c)^{(i-1)} + (d\varepsilon_e^c)^i \quad . \tag{6.14b}$$

It is assumed that the creep strain increment, $(d\varepsilon_e^c)^i$, during the interval dt^i can be obtained from a constant stress creep curve corresponding to ($\dfrac{\sigma_e^i + \sigma_e^{(i-1)}}{2}$). This procedure is illustrated in Figure 6.1. Using the creep law, in equation (6.1), and the hardening rule, the creep strain increment could be written as

$$(d\varepsilon_e^c)^i = A \left[\frac{\sigma_e^i + \sigma_e^{(i-1)}}{2} \right]^m \left[\left(t_e^{(i-1)} + dt^i \right)^n - \left(t_e^{(i-1)} \right)^n \right] \quad . \tag{6.15}$$

The use of an effective time, t_e, based on the accumulated creep strain in equation (6.15) shows the strain hardening approach adopted in this procedure. However, the way in which the time increment, dt^i, has been used, in equation (6.15), to define the creep strain increment illustrates the modification on the strain hardening method with an element of the time hardening law. This modification helps to define the creep strain increment explicitly and makes the numerical implementation convenient. It can be observed that (see Figure 6.1) by using a time subincrement that complies with the conditions (6.10) and (6.11) and is therefore small, the hardening law applied in equation (6.15) becomes closer to a strain hardening law.

Creep strains are implemented through an initial strain method. The creep strain rate at any instant depends on the stresses at the material point. At the beginning of each iteration for the interval dt^i, an approximate value for the creep strain increment can be obtained from equation (6.15) using the stress σ_e^i.

6.2.7. *Load-Time History.* In practice, the loads of external pressure and tension are gradually applied on the tube reaching their final values after a certain period of time. The structure is expected to deform, exhibiting elastic, plastic and creep behavior during this period. Numerical results were obtained with the following load-time history formulation. The loads were first applied on the structure instantaneously without invoking any inertial effects . After application, the loads were kept constant and the structure was allowed to creep for a time period of interest, t. This load-time history was illustrated in Figure 6.2. Even though any load-time history could be simulated in this numerical scheme, this particular time history is used for its convenience in representing the results. The results using this time history are expected to predict a larger effect of creep on collapse strength than will actually occur.

6.2.8. *Collapse Criterion.* The response of a tube with initial imperfections shows a load-displacement behavior with a limit point. Loads which consist of pressure and tension are applied to the tube based on the time history as described above. In Figure 6.3, the graphical representation of the equilibrium load-displacement curves with limit points is given. In these plots, the load λ axis represents external pressure or pressure and tension and the displacement, δ, is a measure of the non-axisymmetric deformation such as ovalization.

In Figure 6.3, the curve denoted by O A_0 B_0 represents the load-deflection behavior of the tube without creep. The load λ_0 corresponding to the limit point B_0 is the prediction for the collapse strength if no creep exists. If the tube exhibits creep behavior when subjected to a load-time history as described above, then the curve O A_0 B_0 represents the instantaneous (time t=0) response of the structure. For a load λ (see Figure 6.3), the displacement corresponding to point A_0 gives the instantaneous response. If the structure is left to creep for a period of t_c with loads held at λ, the displacement changes to a value corresponding to the point A_c. Now the load λ can be varied and the load-deflection curve O A_c B_c is constructed. This curve O A_c B_c is interpreted as the equilibrium load-displacement behavior of the tube corresponding to time t_c.

For a load λ (see Figure 6.3), the tube will collapse at time t_c if the point A_c happens to be a limit point characterized by the slope of the load-displacement curve going to zero.

$$\frac{d\lambda}{d\delta} = 0 \qquad . \tag{6.16}$$

It can be seen that by gradually increasing the load λ to a value such as λ_c, the corresponding equilibrium point B_c becomes a limit point satisfying condition (6.16). The load λ_c is defined as the collapse load of the tube corresponding to time t_c. λ_c can also be interpreted as either the minimum load that should be put on the structure so that it just collapses by time t_c or the maximum load the structure can carry so that it collapses just after time t_c.

6.3. Numerical Predictions.

In the earlier chapters, results from a series of experiments with 304 stainless steel tubes were discussed. During the experiments, this material was found to creep especially at loads close to yield loads, prompting collapse strength predictions for a creep model using creep properties of 304 stainless steel tubes. Experimental results reported by Krempl [41] on the creep behavior of 304 steels at room temperature were used. The coefficients of the power law for creep were obtained through a least square fit on these experimental results.

The equilibrium equations are obtained in the same way as described in the earlier chapters using the principle of virtual work method. The tube is assumed to be under generalized plane strain conditions, showing uniform ovalization under the action of the loads. The difference in the numerical procedure from the previous sections is in the constitutive part. Once the geometry and the material properties are known, collapse loads corresponding to a suitable time t_c, can be obtained according to the procedure outlined in section (6.2.8).

Load-deflection response for a tube of $D_o/t = 24.5$ under external pressure (T=0) is given in Figure 6.4. The equilibrium curves for time periods $t_c = 60$ and 300 seconds are given in this figure in comparison with the no creep equilibrium ($t_c = 0$) response. These equilibrium curves clearly illustrate, how the limit point pressure shifts with the inclusion of creep. The corresponding pressure-axial strain response given in Figure 6.5 shows, how the axial strain at collapse increases when creep is included. The effect of creep on predicted tension-pressure collapse envelope is shown in Figure 6.6 for this tube of $D_o/t = 24.5$. These results show that the effect of creep on collapse strength is not very significant, and that this effect becomes negligible at higher tensile loads.

Chapter 7

DISCUSSION AND CONCLUSIONS

The results from a combined experimental and analytical study on the collapse strength of thick tubes under combined loading are presented here. Collapse tests involved tubes of D/t range 10 to 40. Tension-pressure collapse envelopes were obtained for different loading paths. Collapse tests involving initially ovalized tubes were also carried out. The analytic tool developed models a long tube under generalized plane strain conditions. A suitable plasticity model and nonlinear kinematic relations were applied in the formulation. For a tube having initial geometric imperfections, the limit point load displacement response is solved, the limit loads being the collapse loads.

The analytic results obtained were correlated with the experimental results. The analysis was also used to conduct a parametric study and assess the collapse load sensitivity to various parameters. The main conclusions of the study are as follows:

1. Accurate prediction of the tension-pressure collapse envelope depends on how well the material and geometric parameters are measured. Presence of axial tension reduces the collapse pressure. The extent of this reduction of collapse pressure by tension depends strongly on the stress-strain behavior of the tube material. Tubes of lower D/t tested at high axial loads, show no collapse failure within the axial displacement capability of the test setup.

2. The study conducted with tubes of low initial ovalities shows that changing the loading sequence has very little effect on the tension-pressure collapse envelope.

3. For tubes of lower D/t, collapse occurs after the tube has deformed well into the plastic regime. Results show the yield stress of the tube material to be the most important material parameter. Characterizing any anisotropy in material yielding that is present becomes important for thicker tubes.

4. Initial ovality is a very important geometric parameter which reduces the collapse strength. The analysis also demonstrates the high sensitivity to initial ovality.

5. The analysis shows that residual stresses can affect the collapse strength of higher D/t tubes. Higher tensile loads reduce this effect on collapse strength.

6. Effect of primary creep on collapse strength is not very significant for the type of materials considered. Higher tensile loads reduce this effect.

References

[1] Langner, C. G. and Ayers, R. R.,"The feasibility of Laying Pipelines in Deep Water," *Proceedings of the 4th Offshore Mechanics and Artic Engineering Symposium,* Dallas, Texas, Vol. 1, pp. 478-489, Feb. 1985.

[2] Verner, E. A., Langner, C. G. and Reifel, M. D., "Collapse of Thick Wall Pipe in Ultra Deep Water," *Proceedings of the conference on Pipelines in Adverse Environments,"* Pipeline Division, ASCE, San Diego, California, pp. 159-187, 1973.

[3] Mesloh, R., Johns, T. G. and Sorenson, J. E., "The Propagating Buckle," *Proceedings of the International Conference on the Behavior of Offshore Structures (BOSS),* Vol. 1, pp. 787-797, 1976.

[4] Kyriakides, S. and Babcock, C. D., "Experimental Determination of the Propagation Pressure of Circular Pipes," *ASME Journal of Pressure Vessel Technology,* Vol. 103, pp. 328-336, 1981.

[5] Kyriakides, S. and Babcock, C. D., "On the Dynamics and Arrest of the Propagating Buckle in Offshore Pipelines," *OTC 3479, Proceedings of the 11th Offshore Technology Conference,"* pp. 1035-1045, May 1979.

[6] Kyriakides, S. and Babcock, C. D., "Prediction of Wet Buckles in Offshore Pipelines," *Proceedings of the Marine Technology Conference,* Washington D.C. pp. 439-444, Oct. 1980.

[7] Budiansky, B. and Amazigo, J. C., "Initial Post-buckling Behavior of Cylindrical Shells under External Pressure," *Journal of Mathematics and Physics"* Vol. 47, pp. 223-235, 1968.

[8] Yeh, M. K. and Kyriakides, S., "On the Collapse of Inelastic Thick-Walled Tubes under External Pressure," *ASME Journal of Energy Resources Technology,* Vol. 108, pp.35-47, 1986.

[9] Hutchinson, J. W., "On the Postbuckling Behavior of Imperfection-Sensitive Structures in the Plastic Range," *ASME Journal of Applied Mechanics,* Vol. 39, pp. 155-162, 1972.

[10] Tvergaard, Vol., "Buckling of Elastic-Plastic Cylindrical Panels under Axial Compression," *International Journal of Solids and Structures,* Vol. 13, pp. 957-970, 1970.

[11] Levy, M. M., "Memoire sur un nouveau cas Integrable du Probleme de l'elastique et l'une de ses Applications," *Journal de Mathematiques Pures et Appliquees (Liouville),* Series 3, Vol. 10, pp.5-42, 1884.

[12] Bryan, G. H., "Application of the Energy Test to the Collapse of a Long Thin Pipe under External Pressure," *Proceedings of the Cambridge Philosophical Society,* Vol. 6, pp. 287-292, 1888.

[13] Southwell, R. Vol., "On the Collapse of Tubes by External Pressure," *Philosophical Magazine,* Series 6, Vol. 29, pp. 67-77, Jan 1915.

[14] Timoshenko, S. P., "Working Stresses for Columns and Thin-Walled Structures," *Transactions of the ASME, Applied Mechanics Division,* Vol. 1, pp. 173-183, 1933.

[15] Kyriakides, S. and Babcock C. D., "Large Deflection Collapse Analysis of an Inelastic Inextensional Ring Under External Pressure," *International Journal of Solids and Structures,* Vol. 17, pp. 981-993, 1981.

[16] Yeh, M. K., "Buckling and Postbuckling Behavior of Long Elastoplastic Circular Tubes under External Pressure," *Ph.D. Thesis, Department of Aerospace Engineering and Engineering Mechanics,* The University of Texas at Austin, 1986.

[17] Simonen, F. A. and Shippell, R. J. Jr., "Collapse of Thick-walled Cylinders under External Pressure" *Experimental Mechanics,* Vol. 22, pp. 41-48, 1982.

[18] Edward, S. H. and Miller, C. P., "Discussion on the Effect of Combined Longitudinal Loading and External Pressure on the Strength of Oil-Well Casing," *Drilling and Production Practice,* American Petroleum Institute, pp. 483-502, 1939.

[19] Stuiver, W. and Tomalin, P. F., "The Failure of Tubes under Combined External Pressure and Axial Load," *SESA Proceedings,* Vol. 16(2), pp. 39-48, 1959.

[20] Lubinski, A., "Influence of Neutral Axial Stress on Yield and Collapse of Pipe," *ASME Journal of Engineering for Industry,* Vol. 97, Series B, No. 2, pp. 400-407, May 1975.

[21] Fabian, O., "Collapse of Cylindrical, Elastic Tubes under Combined Bending, Pressure and Axial Loads," *International Journal of Solids and Structures,* Vol. 13, pp. 1257-1270, 1977.

[22] API, "Bulletin on Formulas and Calculations for Casing, Tubing, Drill Pipe and Line Pipe Properties," *API BUL 5C3, 3rd ed.,* American Petroleum Institute, 1980.

[23] Kyogoku, T., Tokimasa, K., Nakanishi, H., Okazawa, T., "Experimental Study on the Effect of Axial Tension Load on the Collapse Strength of Oil Well Casing," *OTC 4108,* pp. 387-395, 1981.

[24] Tamano, T., Mimura, H., Yanagimoto, S., "Examination of Commercial Casing Collapse Strength under Axial Loading," *Proceedings of the First Offshore Mechanics/Artic Engineering/Deep Sea Systems Symposium,* ASME 1, pp. 113-118, 1982.

[25] Pattillo, P. D. and Huang, N. C., "The Effect of Axial Load on Casing Collapse," *Journal of Petroleum Technology,* Society of Petroleum Engineers of AIME, pp.159-164, 1982.

[26] Huang, N. C. and Pattillo, P. D., "Collapse of Oil Well Casing" *ASME Journal of Pressure vessel Technology,* Vol. 104, pp. 36-41, 1982.

[27] Pattillo, P. D. and Huang, N. C. "Collapse of Oil Well Casing with Ovality," *ASME Journal of Energy Resources Technology,* Vol. 107, pp. 128-134, 1985.

[28] Arbocz, J. and Babcock, C. D., "The Effect of General Imperfections on the Buckling of Cylindrical Shells," *ASME Journal of Applied Mechanics,* Vol. 36, pp. 28-38, 1969.

[29]   Arbocz, J. and Williams, J. G., "Imperfections Surveys on a 10 ft. Diameter Shell Structure," *AIAA Journal*, Vol. 15, pp. 949-956, 1977.

[30]   Yeh, M. K. and Kyriakides, S., "Collapse of Deep Water Pipelines," *OTC 5215, Proceedings of The 18th Annual Offshore Technology Conference*, Houston, Texas, pp. 511-520, May 1986.

[31]   Kyriakides, S. and Yeh, M. K., "Plastic Anisotropy in Drawn Metal Tubes," *Engineering Mechanics Research Laboratory, EMRL Report No. 86/11*, The University of Texas at Austin, Dec. 1986.

[32]   Hill, R., "The Mathematical Theory of Plasticity," Oxford University Press, 1950.

[33]   Reissner, E., "On One-dimensional Finite-Strain Beam Theory: The Plane Problem," *ZAMP*, Vol. 23, pp. 798-804, 1972.

[34]   Timoshenko, S. P. and Goodier, J. N., "Theory of Elasticity," 3rd edition, McGraw Hill, 1970.

[35]   Orowan, E., "Creep in Metallic and Non-Metallic Materials," *Proceedings of the First U. S. National Congress of Applied Mechanics,"* ASME, pp. 453-472, 1952.

[36]   Rabotonov, Y. N., "Creep Problems in Structural Members," English Translation Edited by Leckie, F. A., North-Holland Publishing Company, 1969.

[37]   Nickell, R. E., "Thermal Stress and Creep," *Structural Mechanics Computer Programs*, (Ed. Pilkey, W., Saczalski, K. and Schaeffer, H.), University Press of virginia, Charlottesville, pp. 103-122, 1974.

[38]   Hoff, N. J., "Creep Buckling of Plates and Shells," *Applied Mechanics, Proceedings of the Thirteenth International Congress of Theoretical and Applied Mechanics, Moscow, Aug. 1972,"* eds. Becker, E. and Mikhailov, G. K., Springer-Verlag, pp. 124-140, 1973.

[39]   Hoff, N. J., Jahsman, W. E. and Nachbar, W. J. "A Study of Creep Collapse of a Long Circular Cylindrical Shell under Uniform External Pressure," *Journal of Aero/Space*

Sciences, Vol. 26, No. 10, pp. 663-668, 1959.

[40]   Bushnell, D., "A Strategy for the Solution of Problems Involving Large Deflections, Plasticity and Creep," *International Journal for Numerical Methods in Engineering,* Vol. 11, pp. 683-708, 1977.

[41]   Krempl, E., "An Experimental Study of Room-Temperature Rate-Sensitivity, Creep and Relaxation of AISI Type 304 Stainless Steel," *Journal of Mechanics and Physics of Solids,* Vol. 27, pp. 363-375, 1979.

[42]   Brush, D. O. and Almroth B. O., "Buckling of Bars, Plates and Shells," McGraw Hill, 1975.

[43]   Timoshenko, S. P., "Working Stresses for Columns and Thin-Walled Structures," *Transactions of the ASME, Applied Mechanics Division,* Vol. 1, pp. 173-183, 1933.

[44]   Madhavan, R, Yeh, M. K., Kyriakides, S. and Babcock, C. D., "Pipe Collapse under External Pressure and Axial Tension: Computer Program Manual," *GALCIT SM Report No. 87-12,* Caltech, Pasadena, 1987.

[45]   Klingler, L. J. and Sachs, G., "Dependence of the Stress-Strain Curves of Cold-Worked Metals upon the Testing Direction," *Journal of Aeronautical Sciences,* pp. 151-154, 1948.

Appendix A

PROBLEM FORMULATION AND NUMERICAL IMPLEMENTATION

A two dimensional formulation of the elastic-plastic collapse problem is given. The numerical scheme developed by Yeh and Kyriakides [30] is applied with appropriate modifications. The initial geometry of the tube considered includes an ovality, and it is defined by $R_\theta = R_o \, (1 - \Delta'_o \cos 2\theta)$ (see Figure 3.1b). The tube is assumed to be under generalized plane strain, ovalizing uniformly along the length under the action of the loads. The equilibrium equations are derived by applying the principle of virtual work method. These nonlinear equations are solved using an incremental procedure in which the Newton-Raphson method is applied.

A.1. Kinematics.

A small strain large deflection theory is adopted in the formulation, and this gives the capability to compute the postbuckling response, involving large deflections. Shear deformations are neglected by applying the Kirchoff assumption of plane sections through the thickness remain plane. The tube cross section is allowed to develop membrane strain, e. The strain-displacement relations used [42] are given by

$$\varepsilon_s = e + z \, K_s \qquad \text{(A.1a)}$$

and

$$\varepsilon_x = \varepsilon_o \qquad , \qquad \text{(A.1b)}$$

where

$$e = (\frac{v' + w}{R_o}) + \frac{1}{2} (\frac{v' + w}{R_o})^2 + \frac{1}{2} (\frac{v - w'}{R_o})^2 \qquad ,$$

$$K_s = (\frac{v' - w''}{R_o^2}) / \left[1 - (\frac{v - w'}{R_o})^2 \right]^{1/2} \qquad , \qquad \text{(A.2)}$$

$(') = \dfrac{\partial (\,)}{\partial \theta}$, v and w are displacement variables, and z is the through thickness coordinate as

shown in Figure 3.1a.

A.2. Principle of Virtual Work.

The virtual work relation used in its incremental form is given by

$$\int_V (\underline{\sigma} + \underline{\dot{\sigma}}) \, \underline{\dot{\varepsilon}} \, dV - \dot{W} = 0 \quad , \tag{A.3}$$

where ($\dot{}$) stands for increment, and $\underline{\sigma}$ and $\underline{\varepsilon}$ are the stress and strain tensors. The first term, which is an integral over the tube cross section, represents the increment in the strain energy. The second term, $\dot{W}$, stands for the incremental work done by the external forces.

For the problem of a long tube subjected to external pressure and axial loading, this equation reduces to the following expression. Hence, for a segment of unit length applying the symmetry about the line through $\theta = 0$ and $\theta = \pi$ (see Figure 3.1b),

$$2R_o \int_0^\pi \int_{-t/2}^{t/2} (\bar{\sigma}_\theta \dot{\varepsilon}_s + \bar{\sigma}_x \dot{\varepsilon}_x) \, dz \, d\theta$$

$$+ \bar{P} R_o \int_o^{2\pi} \left[(1 + \frac{\bar{w}}{R_o} + \frac{\bar{v}'}{2R_o}) \dot{w} + (\frac{\bar{v}}{R_o} - \frac{\bar{w}'}{2R_o}) \dot{v} - (\frac{\bar{v}}{2R_o}) \dot{w}' + (\frac{\bar{w}}{2R_o}) \dot{v}' \right] d\theta$$

$$- 2R_o \int_0^\pi \int_{-t/2}^{t/2} (\frac{\bar{T}}{2\pi R_o t}) \dot{\varepsilon}_x \, dz \, d\theta = 0 \quad , \tag{A.4}$$

where

$$\bar{\sigma} = \sigma + \dot{\sigma} \qquad \bar{P} = P + \dot{P} \qquad \bar{T} = T + \dot{T}$$
$$\bar{v} = v + \dot{v} \qquad \bar{w} = w + \dot{w} \qquad .$$

In this equation, the first term stands for the increment in the strain energy obtained from the biaxial state of stress in the tube cross section, the second term gives the incremental work done by the external pressure [42], and the third term defines the incremental work done by the axial tension. The sign convention adopted in equation (A.4) is consistent with Figure 3.1a.

A.3. Numerical Solution Procedure.

The displacements v and w are assumed to be given by the following trigonometric series (see Figure 3.1a).

$$w = R_o \sum_{n=0}^{N} a_n \cos n\theta \quad \text{and} \quad v = R_o \sum_{n=2}^{N} b_n \sin n\theta \quad . \tag{A.5}$$

These expressions are substituted in equation (A.4). Since the increments $\dot{a}_n, \dot{b}_n, \dot{\varepsilon}_x$ are arbitrary, the virtual work expression (A.4) gives rise to 2N+1 nonlinear equations represented by

$$\underline{f}(\underline{U}, \dot{\underline{U}}, \underline{Q}, \dot{\underline{Q}}) = 0 \quad , \tag{A.6}$$

where

$$\underline{U} = (\underline{a}, \underline{b}, \varepsilon_x) \qquad \underline{Q} = (P, T)$$
$$\dot{\underline{U}} = (\dot{\underline{a}}, \dot{\underline{b}}, \dot{\varepsilon}_x) \quad \text{and} \quad \dot{\underline{Q}} = (\dot{P}, \dot{T}) \quad .$$

The material behavior is modeled with the constitutive relations as detailed in Chapter 3. Once the material and geometric parameters are known, the solution procedure is started by initializing the state of stress and strain at the Gaussian integration points. The elastic small deflection solution of Reference 43 is used to initiate the iterative procedure.

The Newton-Raphson method is used to solve for $\dot{\underline{U}}$ for a given $(\underline{U}, \underline{Q}, \dot{\underline{Q}})$ or for $\dot{\underline{Q}}$ for a given $(\underline{U}, \underline{Q}, \dot{\underline{U}})$ from the set of equations (A.6). For each load step, the converged solution corresponding to the previous load step is used as the initial guess. The stability of the converged solution at each stage, in the load incrementing mode, is determined by the change in sign of (A.7)

$$\det \left[\frac{\partial \underline{f}}{\partial \underline{U}} \right] \quad . \tag{A.7}$$

In solving for the limit point, the load incrementing mode gives convergence problems in the numerical procedures. Hence, a switch to displacement incrementing mode is highly desirable,

and the maximum load obtained by increasing the displacements is taken as the critical load. This numerical procedure is explained in more detail in Reference 44.

Appendix B

ANISOTROPIC CHARACTERIZATION IN TUBES

Processes such as cold rolling and drawing on plates [45] are known to introduce anisotropies. Hence, the measured stress-strain relation may depend on the orientation of the uniaxial test specimen with respect to the direction of rolling or drawing. In cold or hot drawn tubes, these anisotropies will show up as different yield behavior in the axial and circumferential directions. Collapse strength of thick-walled tubes is strongly influenced by the yield behavior of the tube material. If anisotropies in yield exist, then it becomes important to characterize them for a better prediction of the collapse strength. Hill's anisotropic plasticity model is adopted to model this material yield behavior. A simple way of characterizing the anisotropic parameters in this model is developed in Reference 31. Following this procedure, tests were conducted on some of the tubes to measure the anisotropy.

The yield function in Hill's theory reduces to the following form (see Chapter 3) for the biaxial state of stress in the tube cross section.

$$f(\sigma_{ij}) = \left\{ \sigma_x^2 - (1 + \frac{1}{S_\theta^2} - \frac{1}{S_r^2})\sigma_x \sigma_\theta + \frac{1}{S_\theta^2} \sigma_\theta^2 \right\}^{1/2} = \sigma_{e,max}(\varepsilon_e^p) \quad . \tag{B.1}$$

The parameters S_θ and S_r in this equation quantify the anisotropy in the tube. They are given by $S_\theta = \dfrac{\sigma_{o\theta}}{\sigma_{ox}}$ and $S_r = \dfrac{\sigma_{or}}{\sigma_{ox}}$, where σ_{ox}, $\sigma_{o\theta}$ and σ_{or} are the initial yield stresses in the axial, circumferential and radial directions.

B.1. Experimental Procedure.

Three test specimens are cut from the tube in which each of them have a length of 6 to 8 times the diameter, and the following tests are conducted (see Figure B.1).

B.1.1. *Uniaxial test.* Thin strips are machined from one of the specimens and stress-strain tests are carried out by following the procedure in Chapter 2(2.1.2). This gives the stress-strain behavior of the tube in the axial direction.

B.1.2. *Lateral pressure test.* A servo-hydraulic setup [31] is used to carry out an internal pressure test on one of the specimens (see Figure B.1). Strain gages are bonded on the specimen to measure the axial and circumferential strains. Since pure lateral pressure does not lead to axial loading of the specimen, the stress state [34] in the tube cross section away from the edges is given by

$$\sigma_x = 0 \ , \ \sigma_\theta = \frac{2PD_i{}^2}{(D^2 - D_i{}^2)} \quad , \tag{B.2}$$

where P is the pressure, D the tube outer diameter and D_i the tube inner diameter. Using equation B.2, the stress-strain relation in the hoop direction is obtained from the measured pressure-hoop strain response.

B.1.3. *Hydrostatic pressure test.* In this test, the specimen is sealed at the ends and internally pressurized to generate a hydrostatic state of loading (see Figure B.1). This loading can also be obtained with a hydraulic test setup as described in [31]. The pressure loading in this test results in developing both axial and hoop stresses. Strain gages are used to measure the axial and hoop strains. The stress state in the tube section is given by

$$\sigma_x = \frac{PD_i{}^2}{D^2 - D_i{}^2} \ , \ \sigma_\theta = \frac{2PD_i{}^2}{D^2 - D_i{}^2} \quad . \tag{B.3}$$

The parameters S_θ and S_r are obtained from the pressure-strains data as follows.

B.2. Deriving the Anisotropic Parameters.

From the uniaxial test results, σ_{ox}, which is the initial yield stress in the axial direction, is obtained. The initial yield stress in the hoop direction $\sigma_{o\theta}$ is obtained from the measured hoop stress-strain behavior. These two initial yield stresses define the parameter S_θ. In Figure B.2a, stress-plastic strain relations obtained from uniaxial and lateral pressure tests for a typical case

are given. In this example, the value of S_θ is found to be 0.77.

The results from the hydrostatic pressure test are used to derive an equivalent stress-strain relation. Applying equation (B.3), the stresses σ_x and σ_θ are obtained. The definition of the equivalent stress here is

$$\sigma_e = \left\{ \sigma_x^2 - (1 + \frac{1}{S_\theta^2} - \frac{1}{S_r^2})\, \sigma_x \sigma_\theta + \frac{1}{S_\theta^2}\sigma_\theta^2 \right\}^{1/2} \quad . \tag{B.4}$$

An incremental change in pressure leads to changes in the stresses given by $d\sigma_x$ and $d\sigma_\theta$. The corresponding change in plastic strains, $d\varepsilon_{ij}^p$, is then defined according to equation (3.3) in Chapter 3. Once the $d\varepsilon_{ij}^p$ are known, the equivalent plastic strain is obtained from the work equality $\sigma_{ij}d\varepsilon_{ij}^p = \sigma_e d\varepsilon_e^p$. From this work equality, the definition for the equivalent plastic strain increment becomes (after some algebraic manipulations)

$$d\varepsilon_e^p = \left[\frac{2A}{B} \right]^{1/2} \quad , \tag{B.5}$$

where

$$A = \frac{1}{S_\theta^2}(d\varepsilon_x^p)^2 + (d\varepsilon_\theta^p)^2 + (1 + \frac{1}{S_\theta^2} - \frac{1}{S_r^2})d\varepsilon_x^p d\varepsilon_\theta^p$$

and

$$B = \frac{1}{S_\theta^2} + \frac{1}{S_r^2} - \frac{1}{2} - \frac{1}{2}(\frac{1}{S_\theta^2} - \frac{1}{S_r^2})^2 \quad .$$

Once the parameters S_θ and S_r are known, by using equations (B.4) and (B.5), the pressure-strains data from the hydrostatic pressure test are reduced to get the equivalent stress-strain $(\sigma_e - \varepsilon_e^p)$ behavior.

The iterative procedure, through which the parameters S_θ and S_r are obtained, is illustrated in Figure B.2b. By assuming that the tube material is isotropic, $(S_\theta = S_r = 1)$, the hydrostatic

pressure test results are used to get a σ_e-ε_e^p relation. The axial and the hoop stress-strain curves are also reduced to get the corresponding σ_e-ε_e^p relations (see Figure B.2a). These three stress-strain curves obtained in a typical case are also shown in Figure B.2b. If the material is isotropic, these three equivalent stress-plastic strain curves will match. If the material is not isotropic, then the anisotropic parameter S_θ is obtained from the axial and hoop stress-strain curves as described above. Once S_θ is known, the value for S_r is varied until for some value of S_r the resulting σ_e-ε_e^p curve derived from the hydrostatic test data matches the σ_e-ε_e^p relation in the axial direction. In the sample results given (see Figures B.2b), the values for S_θ and S_r are found to be 0.77 and 0.85 respectively.

No.	t (inches)	$\frac{D_o}{t}$	Δ_o''	Δ_o'	Material Group	P_{co} (psi)	T_c (lbs)	ε_{xc} (%)
1	0.0365	36.71	0.0006	0.0006	M-1	923	0	-
2	0.0364	36.81	0.0007	0.0007	M-2	823	2177	-
3	0.0365	36.70	0.0002	0.0003	M-3	852	3054	0.15
4	0.0364	36.80	0.0005	0.0006	M-2	780	3530	0.22
5	0.0366	36.61	0.0017	0.0017	M-2	608	4239	-
6	0.0366	36.59	0.0014	0.0014	M-3	502	4847	0.50
7	0.0365	36.68	0.0001	0.0002	M-3	495	5231	0.93
8	0.0363	36.91	0.0004	0.0005	M-2	559	5440	-
9	0.0365	36.71	0.0006	0.0007	M-1	450	6039	1.96
10	0.0366	36.60	0.0003	0.0004	M-1	452	6267	2.33
11	0.0365	36.66	0.0004	0.0005	M-3	416	6334	2.29
12	0.0365	36.70	0.0004	0.0006	M-2	388	6670	2.89

Table 1.   Collapse Data with Material and Geometric Parameters for 304 Steel Tubes ($D_o/t = 38.3$, T → P).

No.	t (inches)	$\frac{D_o}{t}$	Δ_o''	Δ_o'	Material Group	P_{co} (psi)	T_c (lbs)	ε_{xc} (%)
1	0.0491	24.45	0.0013	0.0014	M-6	2649	0	-
2	0.0491	24.45	0.0012	0.0013	M-6	2608	1539	0.11
3	0.0524	22.85	0.0008	0.0017	M-4	2573	3990	-
4	0.0492	24.41	0.0011	0.0012	M-6	2085	4699	0.40
5	0.0495	24.24	0.0008	0.0009	M-6	2044	4755	0.39
6	0.0488	24.61	0.0009	0.0009	M-5	1713	6031	0.71
7	0.0488	24.62	0.0006	0.0009	M-5	1188	7999	2.17
8	0.0524	22.85	0.0005	0.0016	M-4	1770	8011	0.82
9	0.0490	24.52	0.0013	0.0013	M-5	1058	8967	3.06
10	0.0488	24.61	0.0001	0.0003	M-5	1089	9433	4.53
11	0.0491	24.46	0.0004	0.0005	M-6	1021	10255	5.94
12	0.0488	24.62	0.0016	0.0017	M-5	1035	11120	7.94

Table 2.   Collapse Data with Material and Geometric Parameters for 304 Steel Tubes ($D_o/t = 24.5$, T → P).

No.	t (inches)	$\dfrac{D_o}{t}$	$\Delta_o{}''$	$\Delta_o{}'$	Material Group	P_{co} (psi)	T_c (lbs)	ε_{xc} (%)
1	0.0634	18.75	0.0002	0.0002	M-8	3672	0	-
2	0.0642	18.52	0.0301	0.0321	M-7	1972	0	-
3	0.0642	18.53	0.0005	0.0011	M-7	3355	2042	0.16
4	0.0639	18.62	0.0004	0.0008	M-7	2813	5017	0.65
5	0.0633	18.80	0.0004	0.0008	M-8	2554	5829	0.96
6	0.0639	18.62	0.0007	0.0008	M-7	2267	7262	1.85
7	0.0634	18.75	0.0005	0.0011	M-8	1726	9465	3.17
8	0.0634	18.76	0.0006	0.0006	M-8	1640	9936	3.72
9	0.0638	18.65	0.0002	0.0006	M-7	1673	10606	5.24
10	0.0634	18.76	0.0002	0.0002	M-8	1676	11064	5.38
11*	0.0634	18.76	0.0006	0.0007	M-8	3229	11369	8.83

Table 3. Collapse Data with Material and Geometric Parameters for 304 Steel Tubes (D_o/t = 18.2 , T $\rightarrow$ P).

No.	t (inches)	$\dfrac{D_o}{t}$	$\Delta_o{}''$	$\Delta_o{}'$	Material Group	P_{co} (psi)	T_c (lbs)	ε_{xc} (%)
1	0.0953	12.12	0.0003	0.0004	M-10	7483	0	-
2	0.0954	12.10	0.0002	0.0003	M-9	7130	2040	0.59
3	0.0953	12.12	0.0002	0.0002	M-9	6632	5043	1.42
4	0.0954	12.11	0.0004	0.0004	M-9	6325	8023	3.32
5	0.0953	12.11	0.0003	0.0004	M-10	6593	9989	5.21
6	0.0954	12.10	0.0002	0.0002	M-10	6513	10499	5.72
7	0.0952	12.13	0.0004	0.0004	M-10	6441	10506	5.97
8	0.0953	12.11	0.0007	0.0007	M-9	6146	10910	4.95
9	0.0953	12.11	0.0004	0.0004	M-10	6439	12015	7.41
10*	0.0954	12.10	0.0002	0.0005	M-9	6109	14084	8.92

Table 4. Collapse Data with Material and Geometric Parameters for 304 Steel Tubes (D_o/t = 12.2 , T $\rightarrow$ P).

* Experiments (no collapse)

No.	t (inches)	$\dfrac{D_o}{t}$	$\Delta_o{}''$	$\Delta_o{}'$	Material Group	P_{co} (psi)	T_c (lbs)	ε_{xc} (%)
1	0.0491	24.45	0.0012	0.0013	M-6	2608	1539	0.11
2	0.0441	27.17	0.0041	0.0041	M-11	1715	1370	0.08
3	0.0463	25.90	0.0069	0.0071	M-11	1717	1490	0.06
4	0.0440	27.23	0.0092	0.0091	M-11	1528	1390	0.07
5	0.0460	26.09	0.0180	0.0196	M-11	1140	1442	0.06
6	0.0434	27.64	0.0382	0.0412	M-11	869	1388	0.05

Table 5.   Collapse Data for Initially Ovalized 304 Steel Tubes
$(D_o/t = 26.7 , \text{T} \to \text{P}, T_c/T'_o = 0.160)$

No.	t (inches)	$\dfrac{D_o}{t}$	$\Delta_o{}''$	$\Delta_o{}'$	Material Group	P_{co} (psi)	T_c (lbs)	ε_{xc} (%)
1	0.0524	22.85	0.0005	0.0016	M-4	1770	8011	0.82
2	0.0437	27.40	0.0020	0.0022	M-12	1154	6624	0.65
3	0.0427	28.08	0.0043	0.0046	M-12	988	6483	0.55
4	0.0431	27.79	0.0094	0.0098	M-12	943	6501	0.42
5	0.0438	27.35	0.0130	0.0143	M-12	874	6590	0.44
6	0.0440	27.23	0.0179	0.0191	M-12	773	6665	0.43
7	0.0442	27.11	0.0248	0.0270	M-12	730	6680	0.37

Table 6.   Collapse Data for Initially Ovalized 304 Steel Tubes
$(D_o/t = 26.6 , \text{T} \to \text{P}, T_c/T'_o = 0.725)$

No.	t (inches)	$\dfrac{D_o}{t}$	$\Delta_o{}''$	$\Delta_o{}'$	Material Group	P_{co} (psi)	T_c (lbs)	ε_{xc} (%)
1	0.0440	27.22	0.0014	0.0023	M-13	1857	913	0.03
2	0.0436	27.48	0.0026	0.0032	M-13	1630	3359	0.14
3	0.0438	27.35	0.0033	0.0035	M-13	1335	4832	0.24
4	0.0452	26.50	0.0018	0.0023	M-13	1536	5087	0.25
5	0.0430	27.86	0.0034	0.0040	M-13	1173	5735	0.36
6	0.0435	27.53	0.0035	0.0037	M-13	1020	6309	0.50
7	0.0429	27.93	0.0020	0.0026	M-13	853	6764	0.682

Table 7.   Collapse Data with Material and Geometric Parameters for 304 Steel Tubes ($D_o/t = 27.2$, P $\rightarrow$ T).

NO.	Load Path	t (inches)	$\dfrac{D_0}{t}$	$\Delta_o{}''$	$\Delta_o{}'$	Material Group	P_{co} (psi)	T_c (lbs)	ε_{xc} (%)
1	-	0.0558	21.36	0.0005	0.0006	M-14	592	0	-
2	-	0.0946	12.20	0.0004	0.0004	M-15	1317	0	-
3	-	0.0944	12.23	0.0065	0.0068	M-15	1205	0	-
4	$P \rightarrow T$	0.0944	12.23	0.0012	0.0012	M-15	1219	1258	0.83
5	$T \rightarrow P$	0.0940	12.29	0.0014	0.0014	M-15	1374	2515	3.13
6*	$P \rightarrow T$	0.0943	12.24	0.0002	0.0002	M-15	1131	3705	3.33

Table 8.   Collapse Data with Material and Geometric Parameters for 6061-O Aluminum Tubes.

* *Experiments (no collapse)*

Material Group	σ_o' (ksi)	σ_y (ksi)	E $*10^6$ (psi)	n	s_θ	s_r
M-1	40.5	32.1	30.0	10.0	0.90	0.90
M-2	39.3	34.3	29.4	11.4	0.90	0.90
M-3	39.0	34.8	29.3	12.7	0.90	0.90
M-4	55.8	49.9	29.0	13.8	-	-
M-5	51.4	45.1	28.9	11.2	-	-
M-6	51.8	44.9	28.9	12.0	-	-
M-7	48.3	39.9	26.2	9.7	-	-
M-8	49.6	42.3	27.5	10.5	-	-
M-9	53.3	43.9	27.8	9.4	0.79	0.79
M-10	54.1	44.1	26.6	9.4	0.79	0,79
M-11	52.4	44.9	28.6	11.0	0.77	0.85
M-12	55.3	48.6	26.8	11.8	0.77	0.85
M-13	55.9	49.8	28.0	12.8	0.77	0.85
M-14	12.0	9.8	10.1	9.0	-	-
M-15	8.2	5.4	10.4	5.0	-	-

Table 9.   Data on Material Parameters

No.	t (inches)	$\dfrac{D_o}{t}$	σ_o' ksi	σ_y ksi	E $\times10^6$ (psi)	n	Δ_o'
S-1	0.035	38.29	39.0	34.0	29.5	12.0	0.0006
S-2	0.049	24.51	53.4	46.4	28.9	12.2	0.0010
S-3	0.065	18.23	49.0	40.8	26.7	10.0	0.0008
S-4	0.095	12.16	53.3	44.0	27.3	9.4	0.0005
S-5	0.045	26.67	52.4	44.9	28.6	11.0	-
S-6	0.045	26.62	55.3	48.6	26.8	11.8	-
S-7	0.044	27.23	55.9	49.8	28.0	12.8	0.0030
S-8	0.095	12.16	8.2	5.4	10.4	5.0	0.0010

Table 10.   Average Values for Material and Geometric Parameters used in Theoretical Predictions.
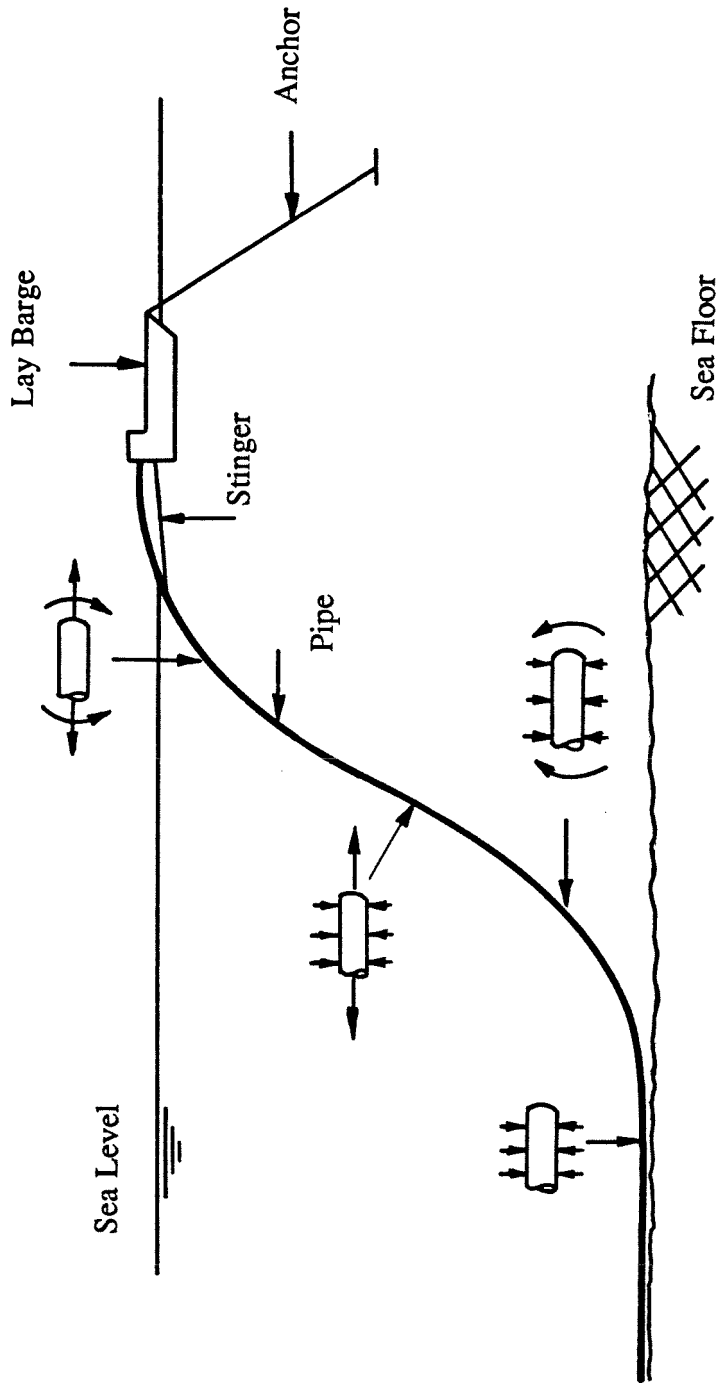
Figure 1.1. Pipelaying Method ('S' Configuration)

-60-
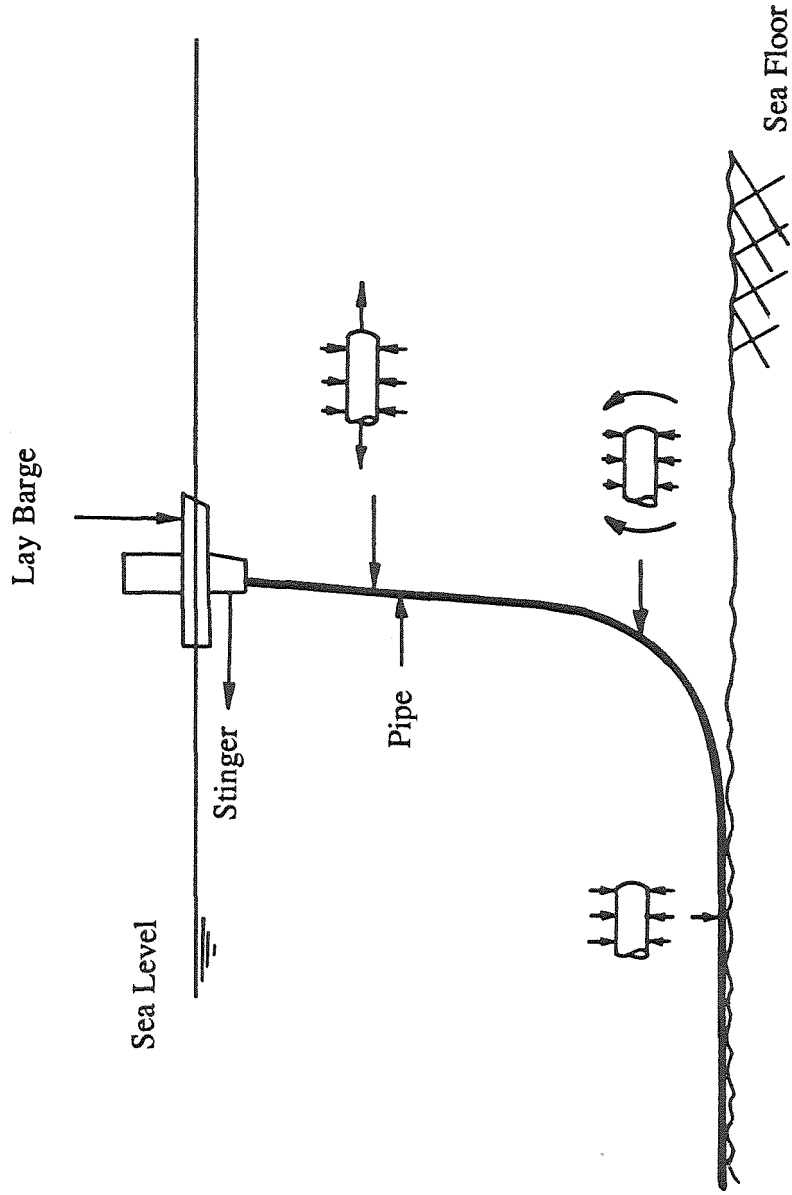
Figure 1.2.   Pipelaying Method ('J' Configuration)
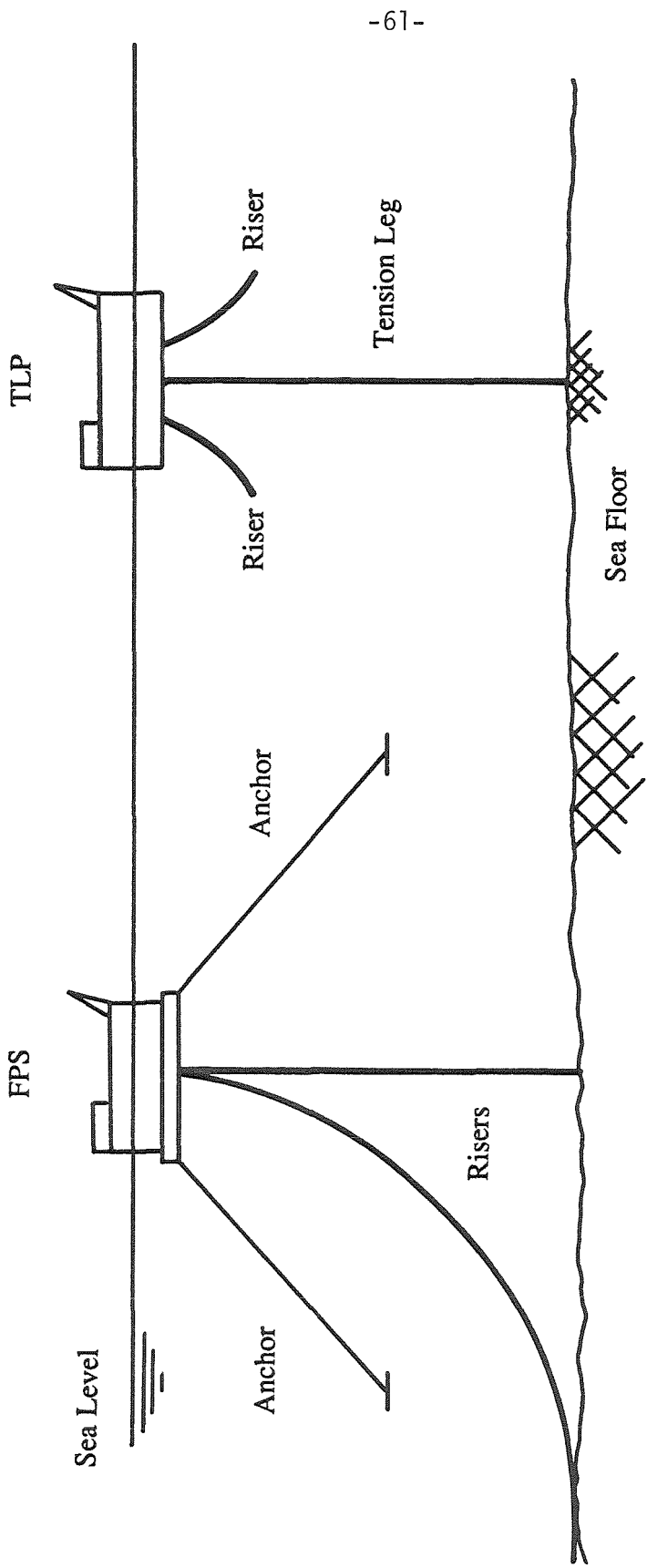
Figure 1.3.   Floating Production System (FPS) and Tension Leg Platform (TLP).
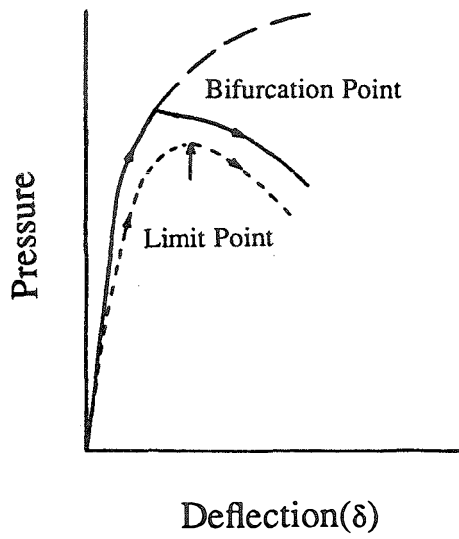
Figure 1.4.   Pressure-Deflection Response of a Thick-Walled Tube under External Pressure
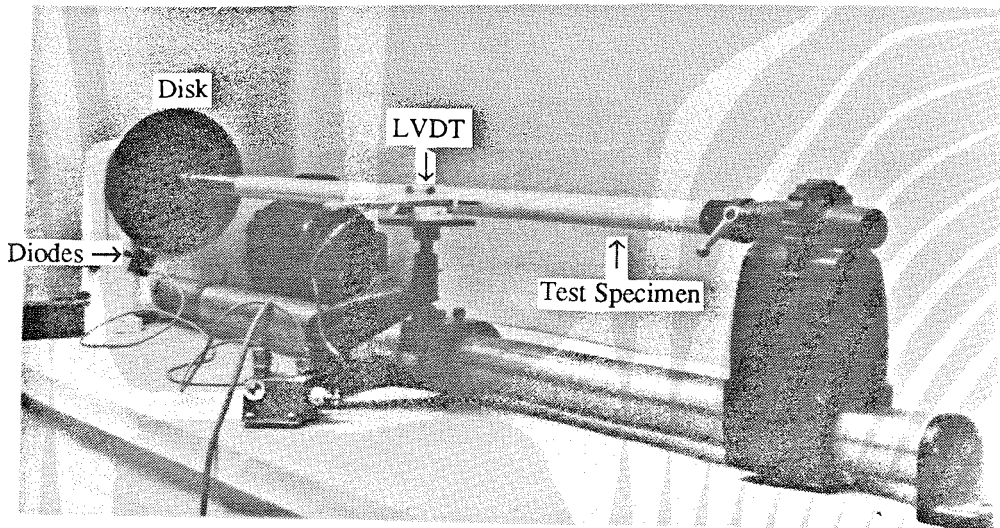
Figure 2.1.   Experimental Facility to Measure Initial Ovality
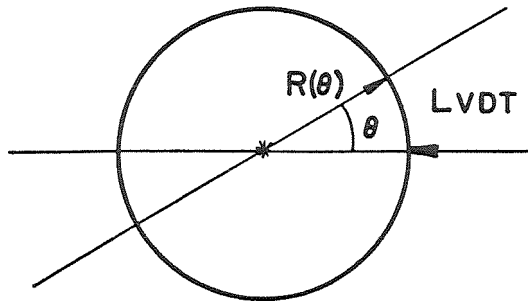
Figure 2.2.   Coordinate System for Initial Ovality Measurements

$$\Delta''_o = 0.0006, \Delta'_o = 0.001$$
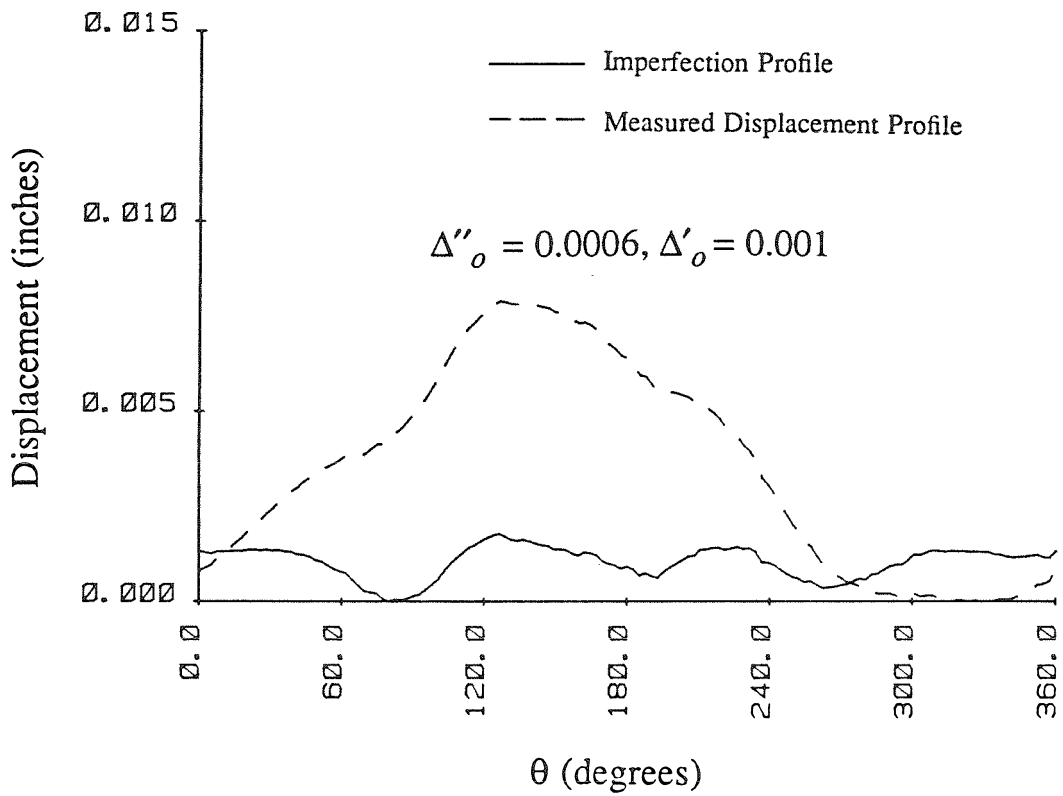
Figure 2.3.   Typical Case of a Displacement Profile as Measured and the Deduced Imperfection Profile.
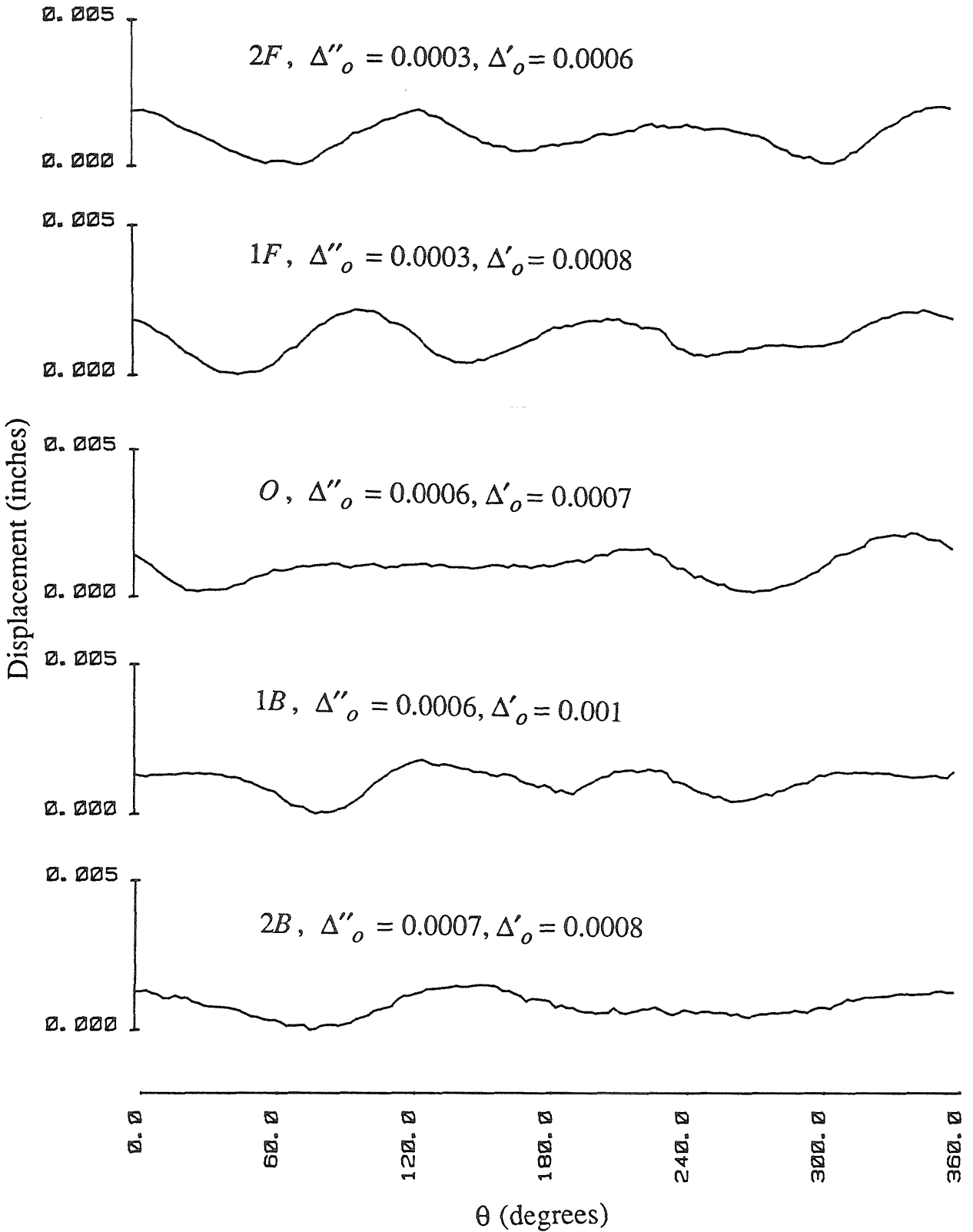
Figure 2.4. Imperfection Profiles at Five Locations along the Length of a Specimen.
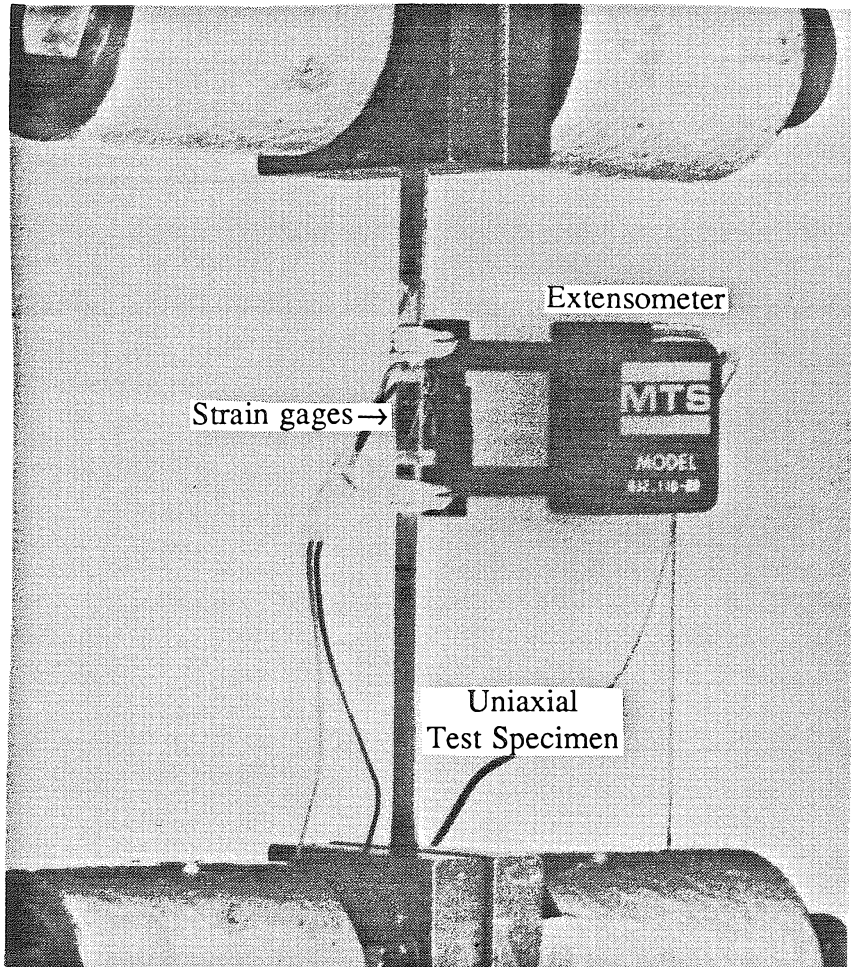
Figure 2.5.   Stress-Strain Measuring Setup with Strain Gages and Extensometer.
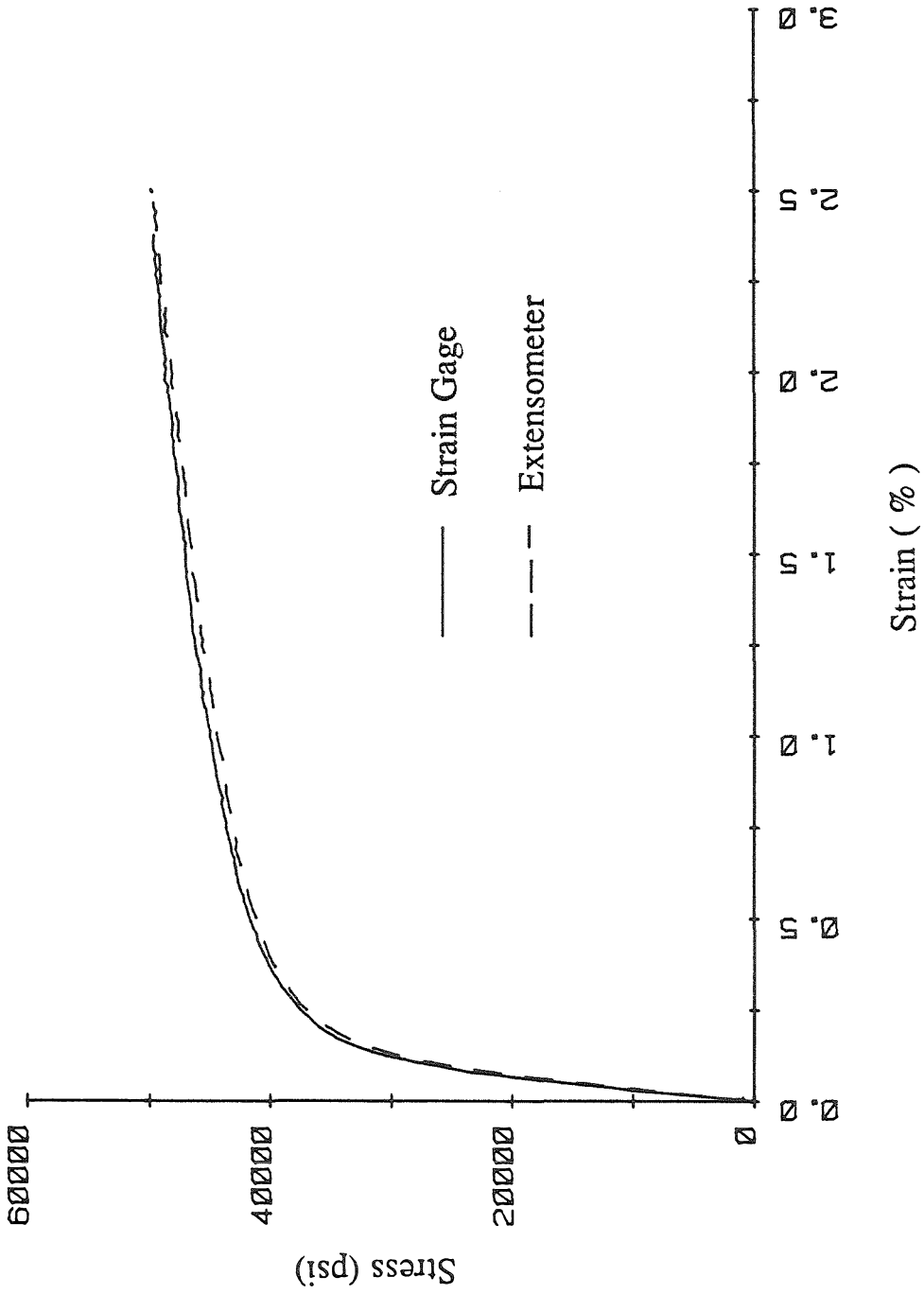
Figure 2.6.   Comparison of Stress-Strain Curves from Strain Gages and Extensometer
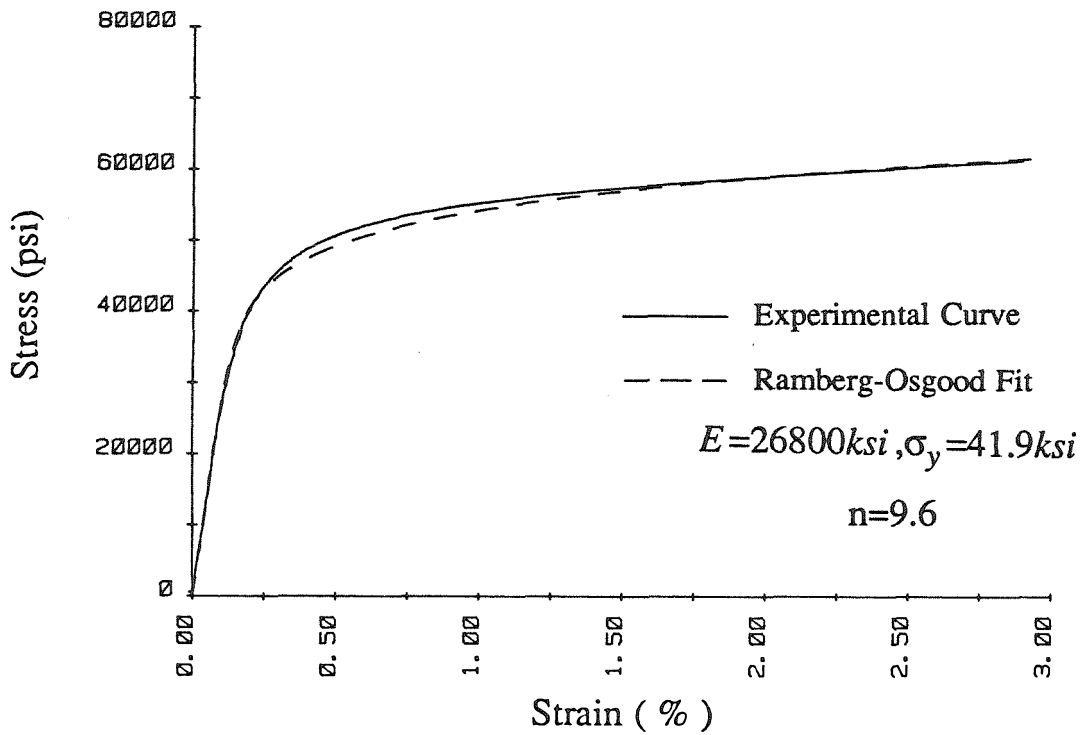
Figure 2.7a.   Experimental Stress-Strain Curve and Ramberg-Osgood Fit for 304 Stainless Steel.
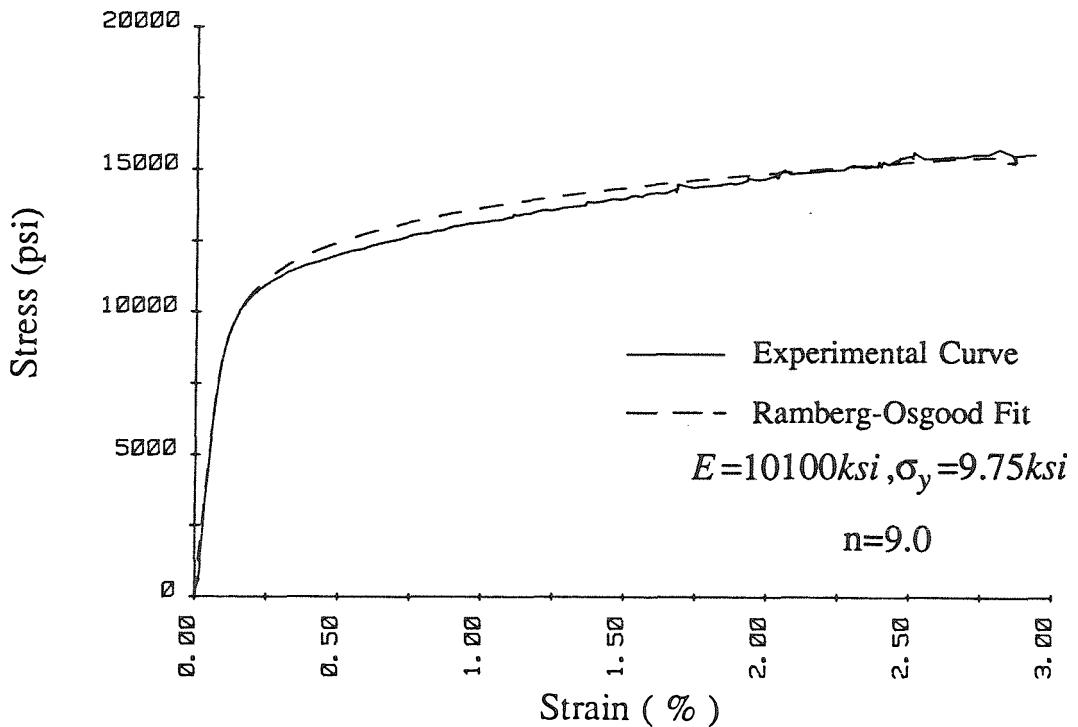
Figure 2.7b.   Experimental Stress-Strain Curve and Ramberg-Osgood Fit for Aluminum 6061-O.
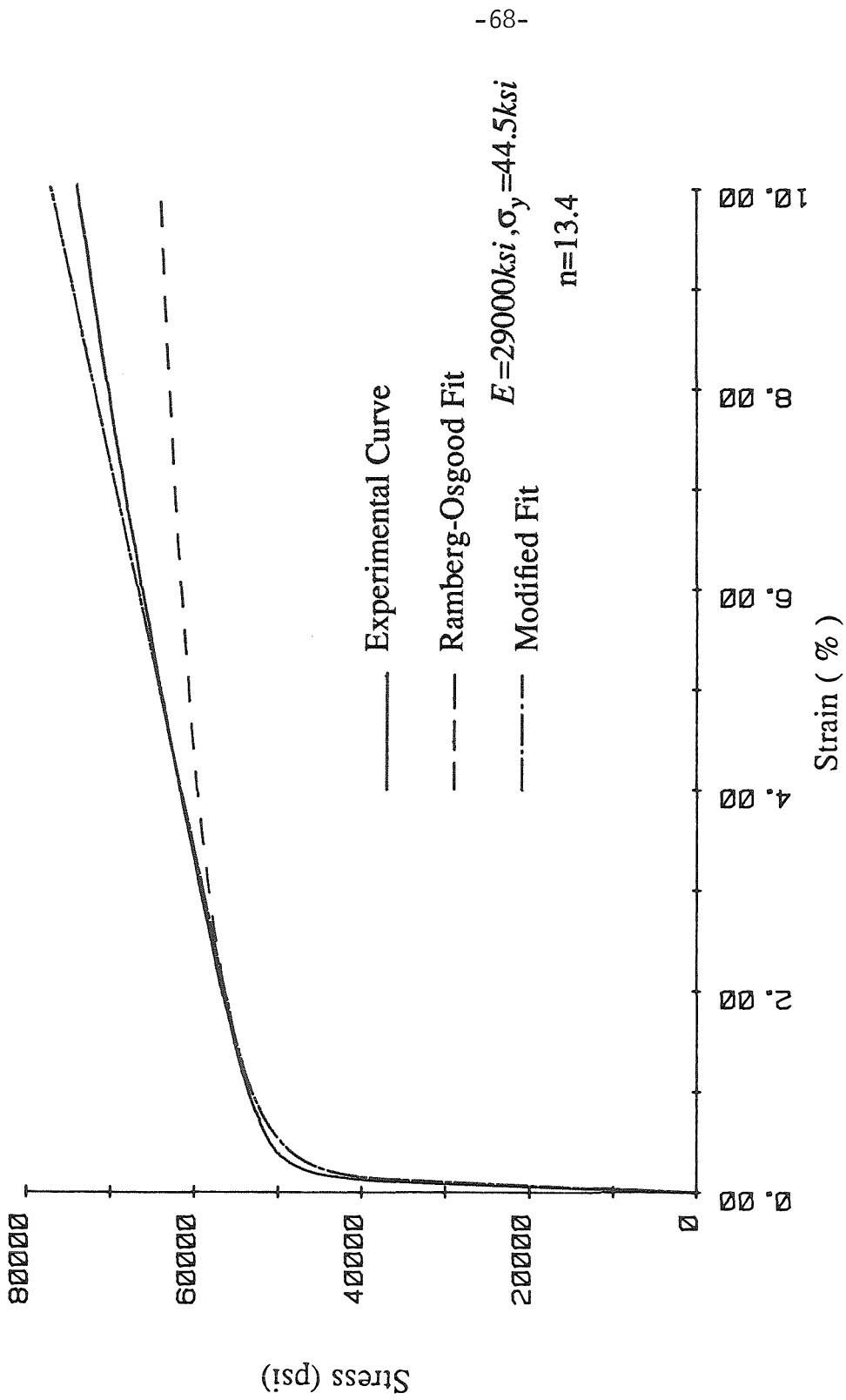
Figure 2.8. Experimental and Fitted Stress-Strain Curves for 304 Steel.
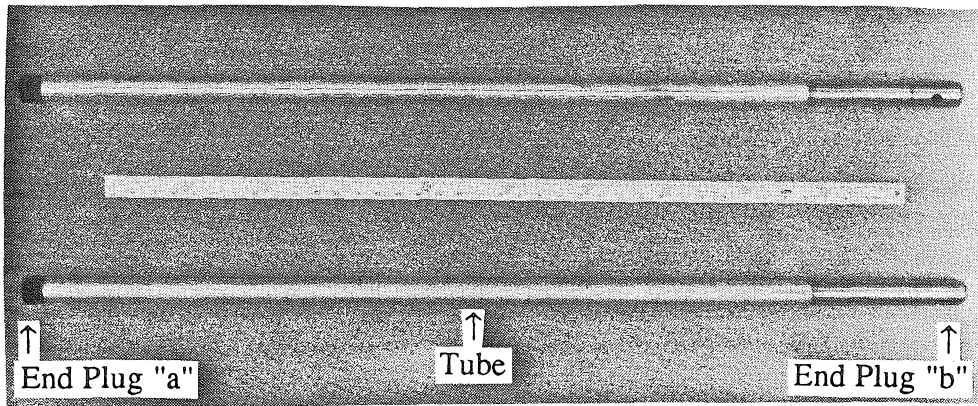
Figure 2.9. Test Specimens Shown with a Meter Scale
(Aluminum 6061-O, D_o/t = 12.2).
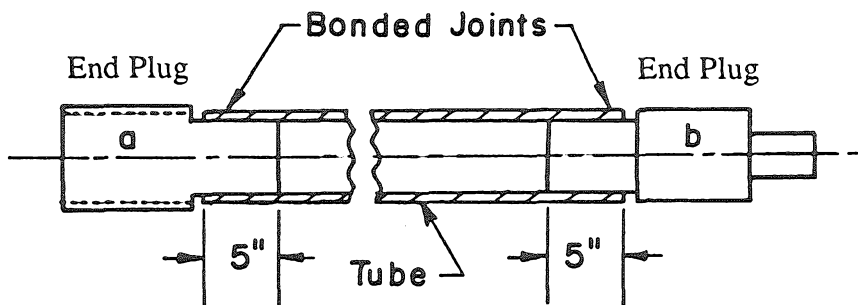
Figure 2.10. Schematic of Test Specimen
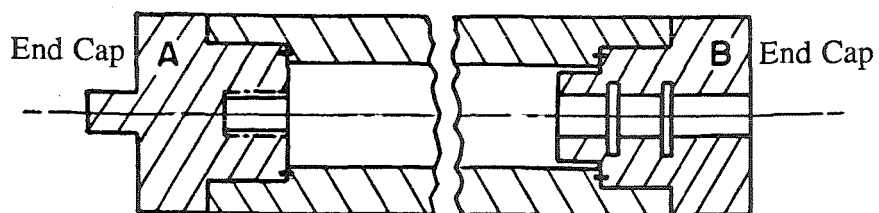
Figure 2.11.   Schematic of Pressure Chamber
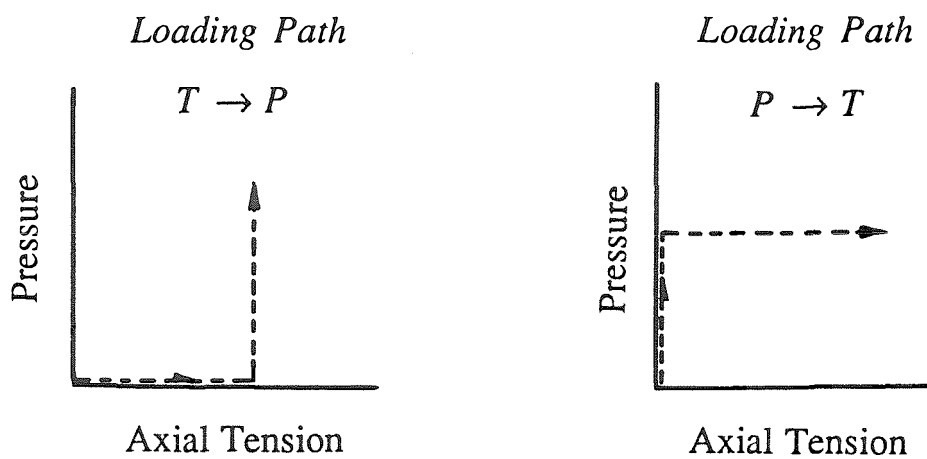
Figure 2.12.   Loading Paths Followed in the Collapse Experiments
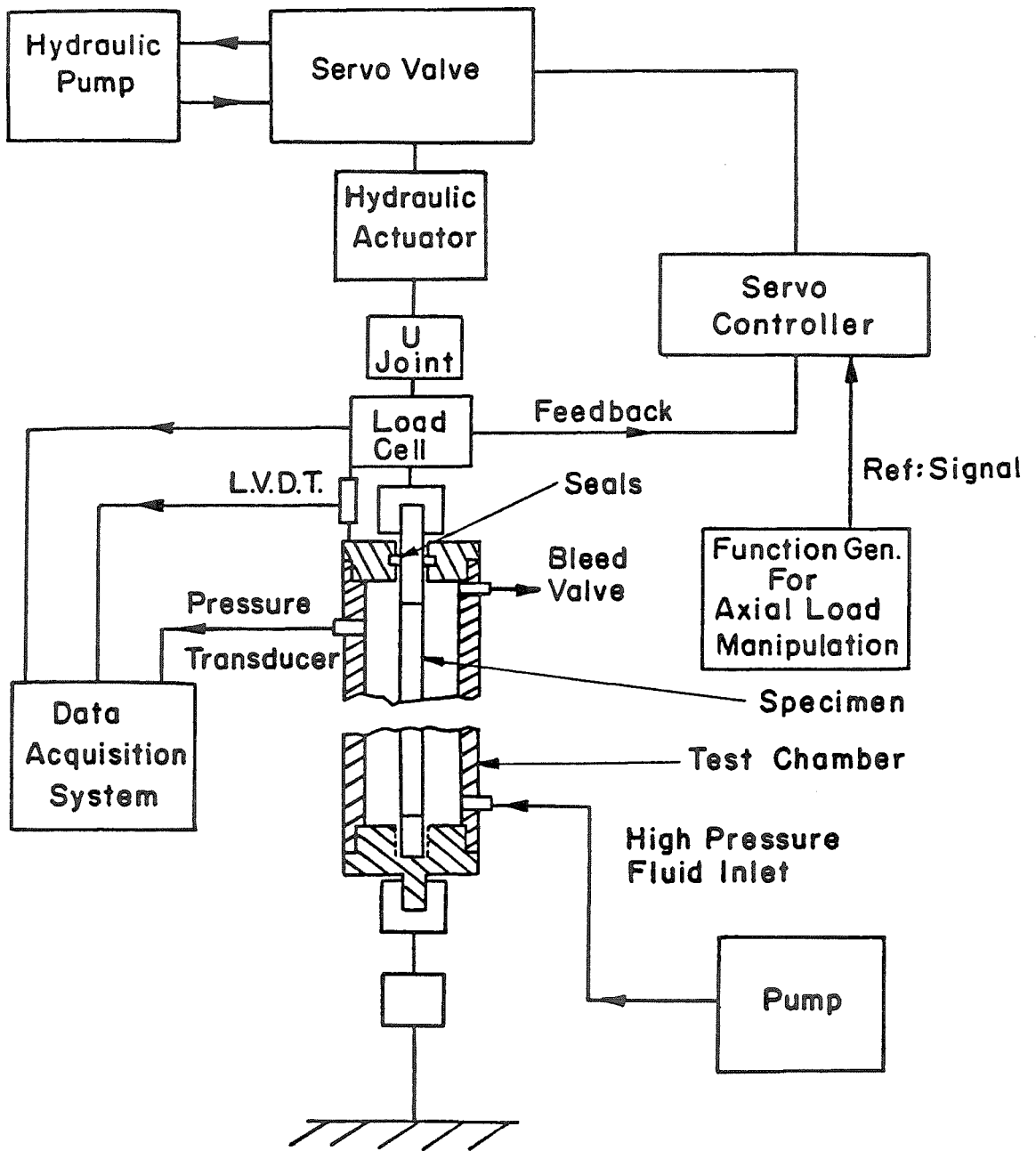
Figure 2.13.   Schematic of the Tension and Pressure Test Setup
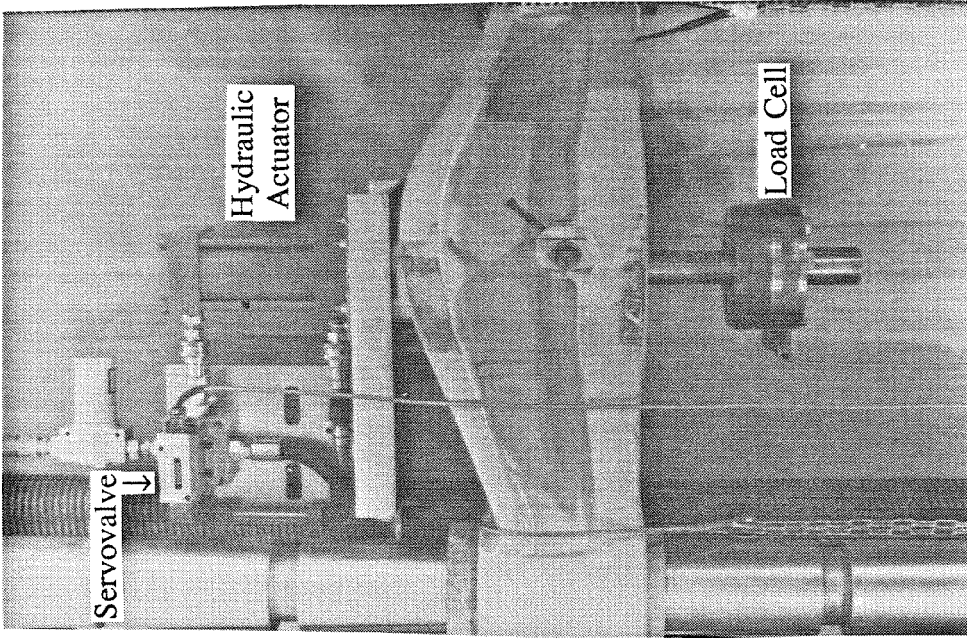
Figure 2.15. Servo-Controlled Hydraulic Cylinder System
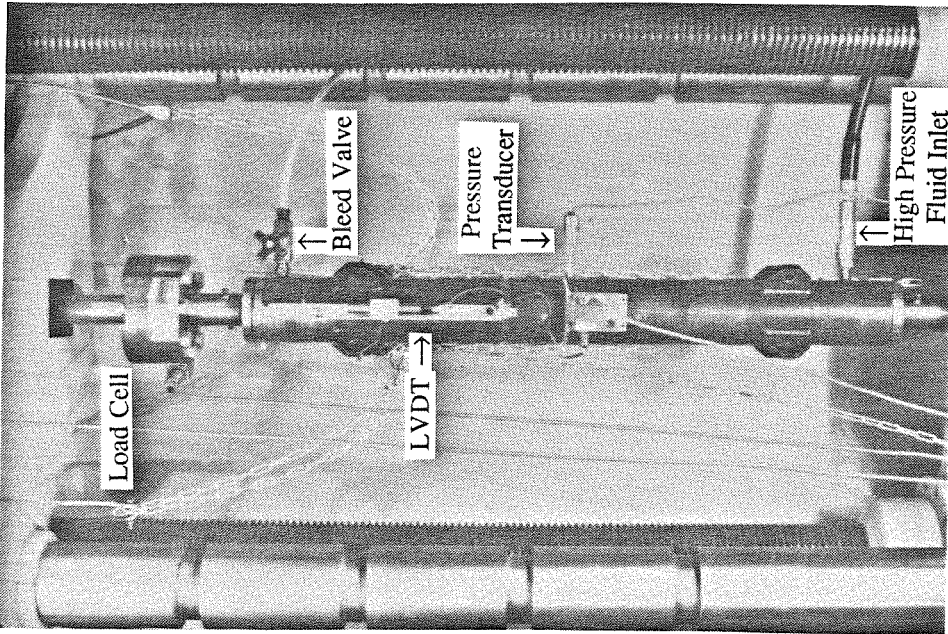
Figure 2.14. Combined Tension and Pressure Setup
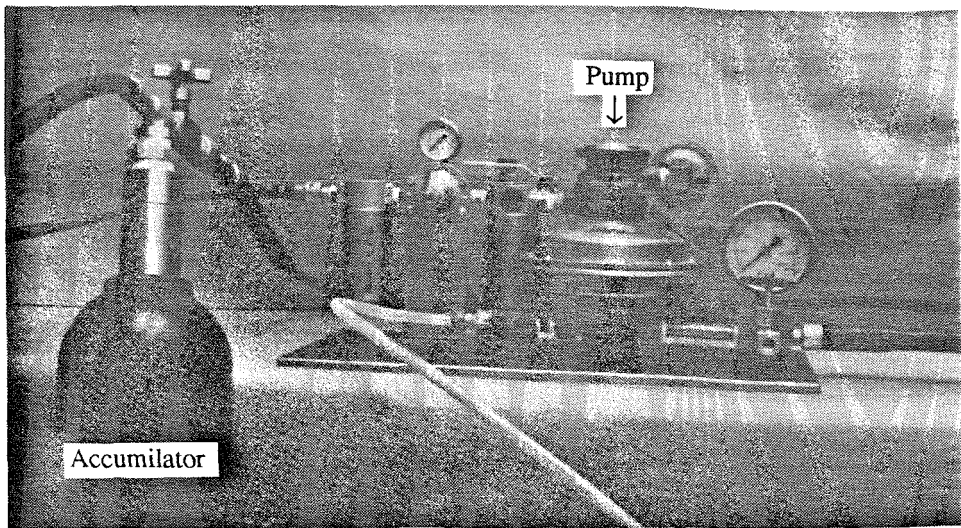
Figure 2.16. Accumulator and Pump Setup Used in Tests
Involving Loading Path P → T
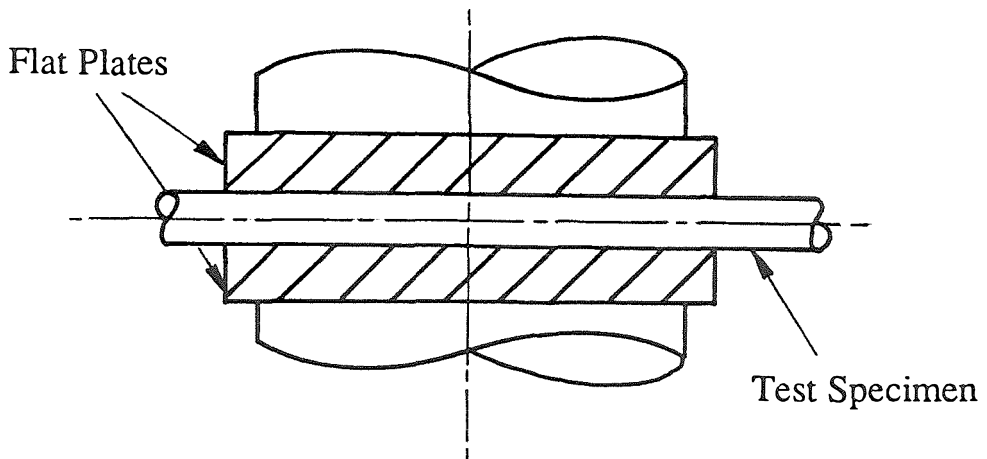
Figure 2.17. Schematic of the Hydraulic Press with Flat Plates, Used to Induce
Initial Ovality on Test Specimen
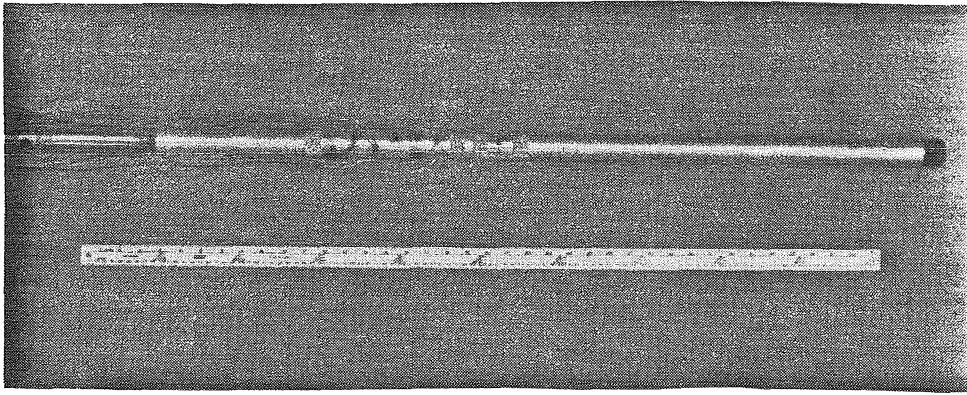
Figure 2.18. Test Specimen (D_o/t = 12.2, Aluminum 6061-O) with Strain Gages Attached, shown with a Meter Scale.
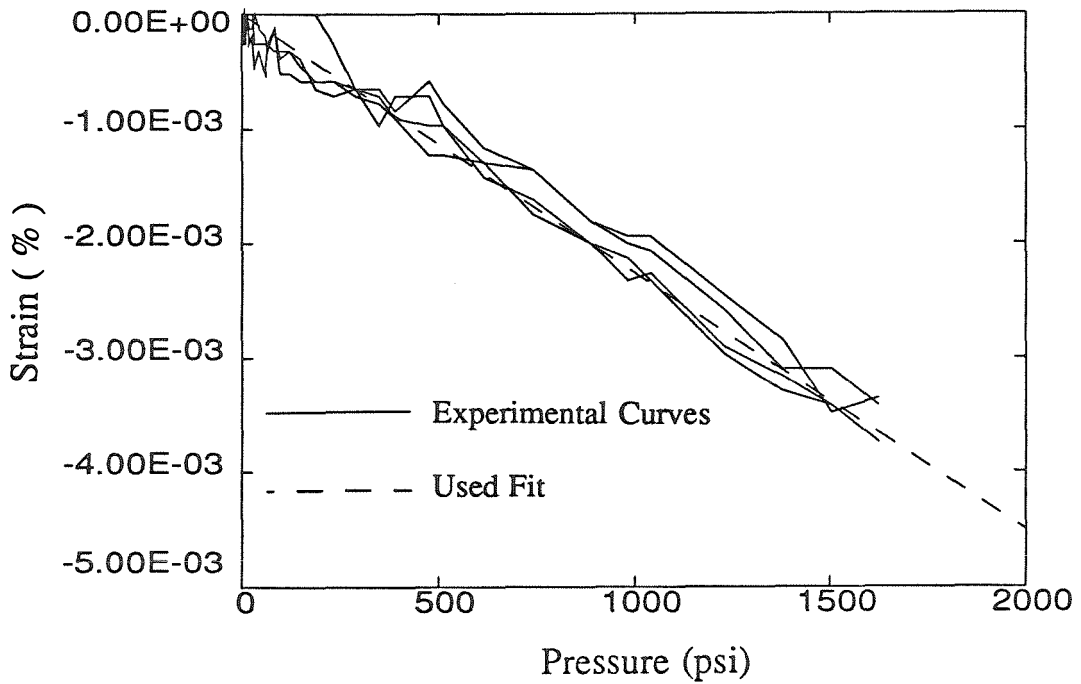
Figure 2.19. Lateral Pressure Sensitivity of the Film Type Strain Gages Used.
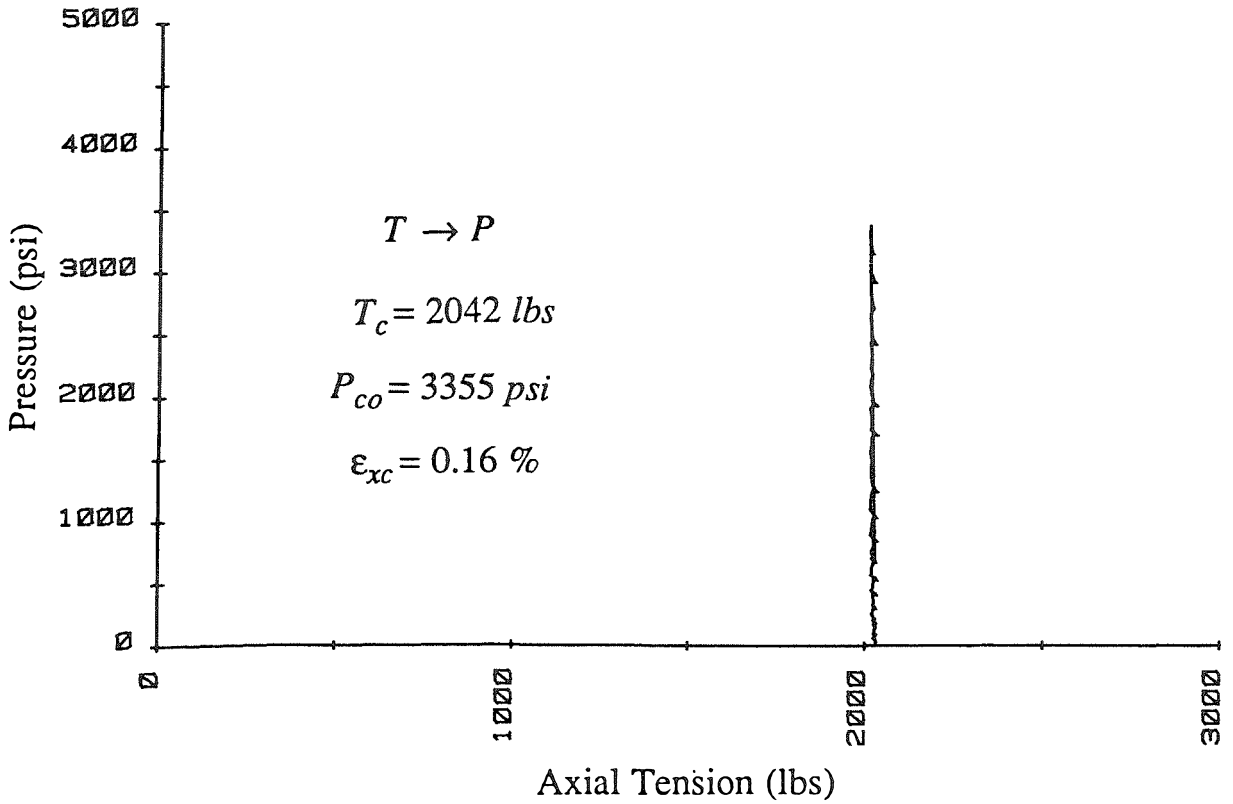
Figure 2.20a.   Measured Axial Tension-Pressure Response Until Collapse
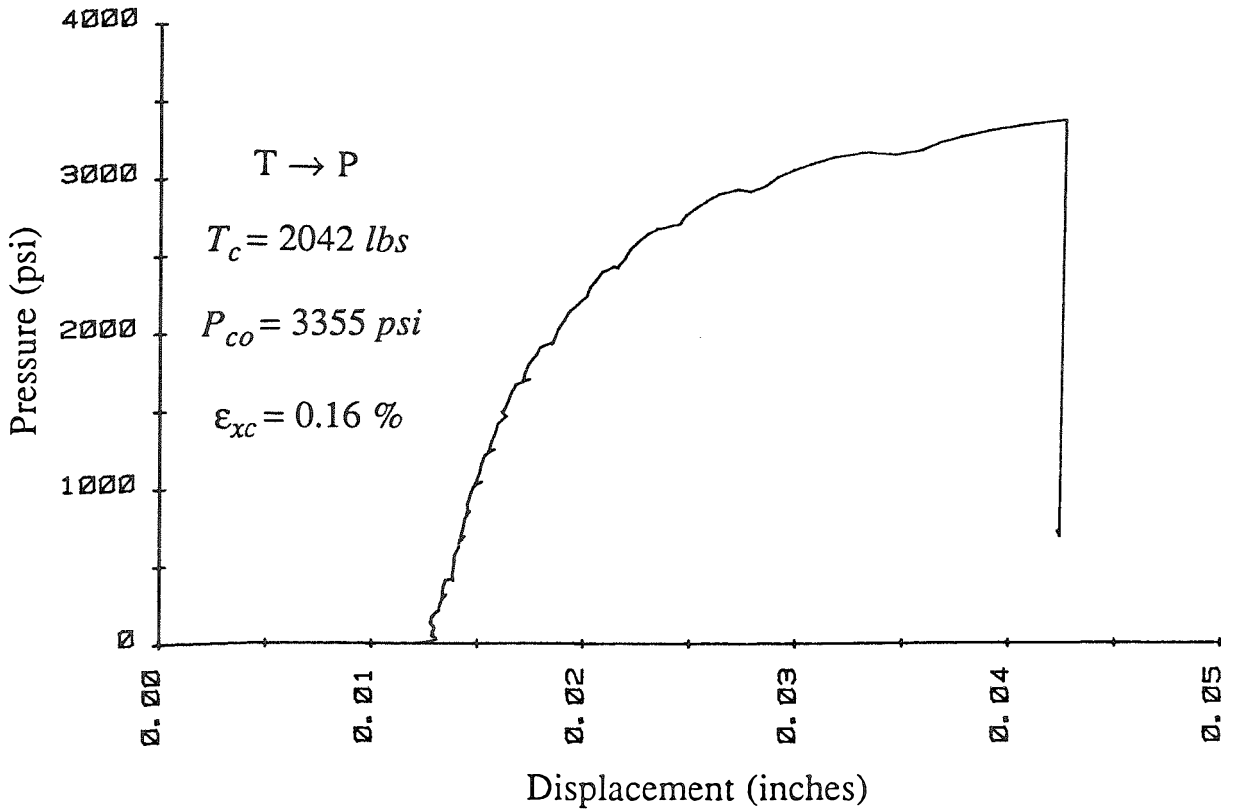
Figure 2.20b.   Measured Axial Elongation-Pressure Response Until Collapse

Figure 2.22. Close-up of the Local Collapse Pattern for Specimens of Different D_o/t Under Loading Path T → P (From left to right D_o/t =38.3,24.5,18.2,12.2 of 304 steel).

Figure 2.21. Collapsed Test Specimens of Different D_o/t (From left to right D_o/t =38.3,24.5,18.2,12.2 of 304 steel) Under Loading Path T → P
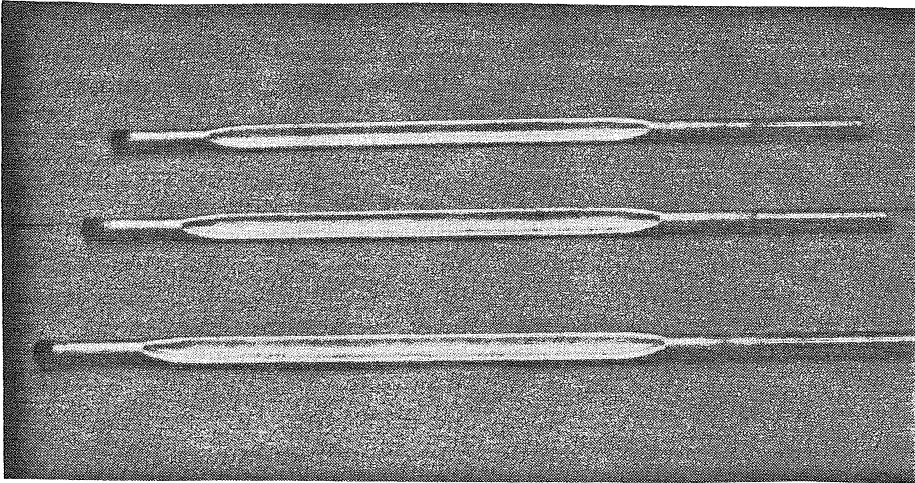
Figure 2.23. Collapsed Test Specimens Under Loading Path P → T
(304 steel, D_o/t =27.2)
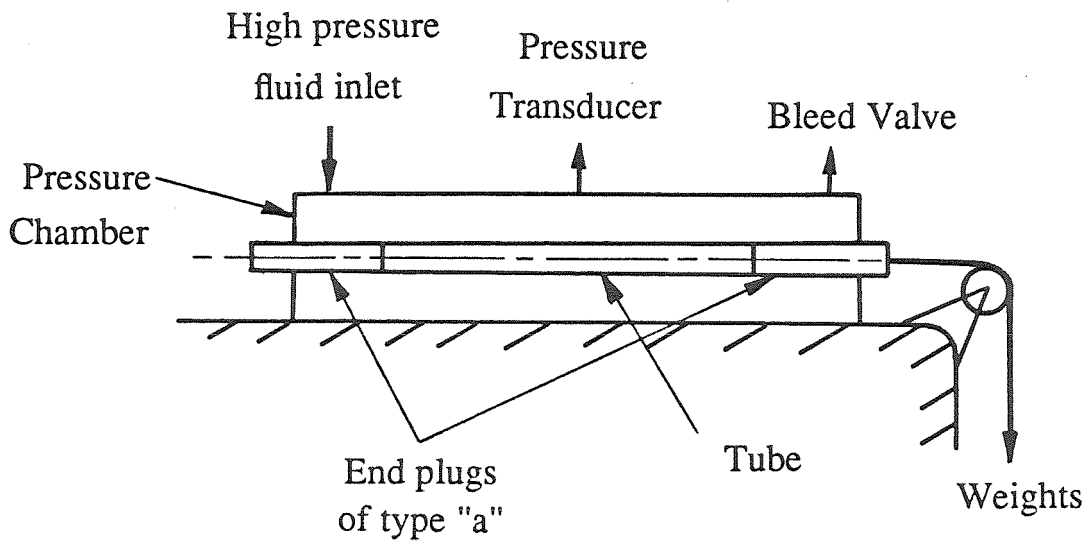
Figure 2.24. Schematic of the Setup Used to Measure the Frictional
Resistance at the Seals, at Different Pressures.
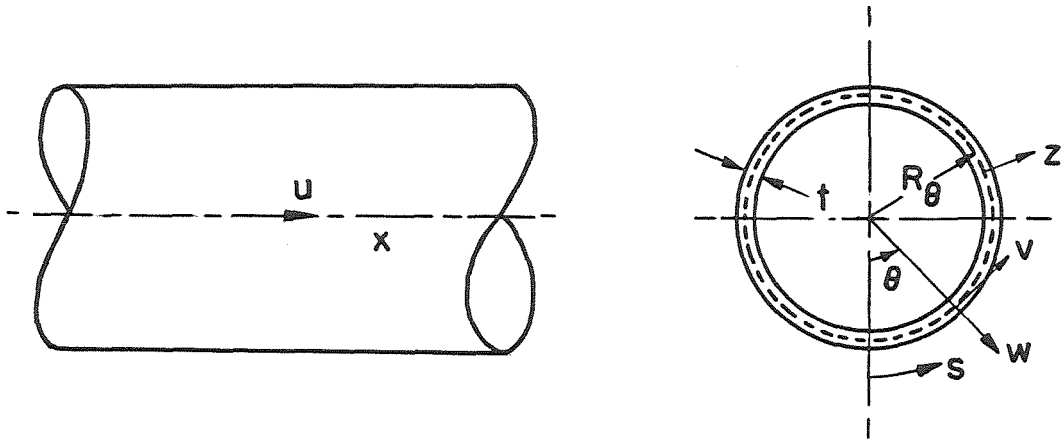
a) Problem Variables

$$\frac{R_\theta}{R_o} = \left(1 - \frac{W_o}{R_o} \cos 2\theta\right)$$
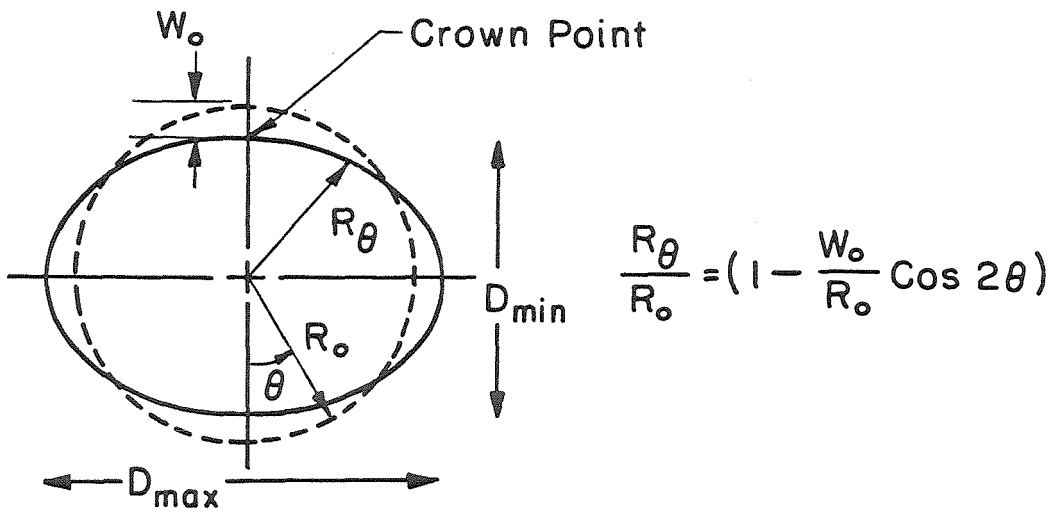
b) Initial Geometry

Figure 3.1. Idealized Initial Geometry of Tube Cross Section and Problem Variables.
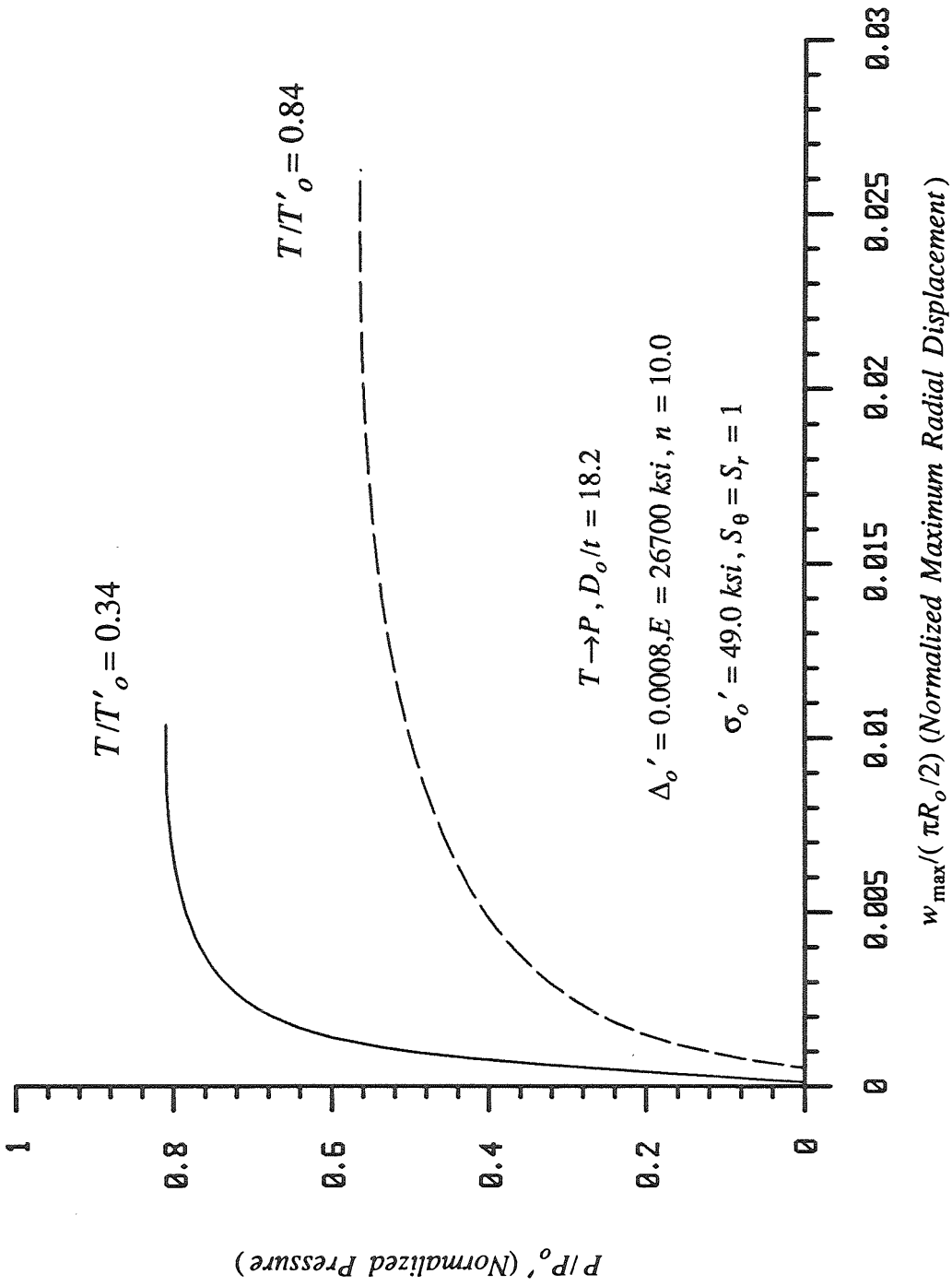
Figure 3.2a.   Predicted Pressure-Deflection Responses at Different Prescribed Axial Tensions.

$P/P'_o = 0.37$

$P/P'_o = 0.50$

$P \rightarrow T, D_o/t = 18.2$

$\Delta_o' = 0.0008, E = 26700 \ ksi, n = 10.0$

$\sigma_o' = 49.0 \ ksi, S_\theta = S_r = 1$

$w_{max}/(\pi R_o/2)$ (*Normalized Maximum Radial Displacement*)

T/T_o' (*Normalized Axial Tension*)
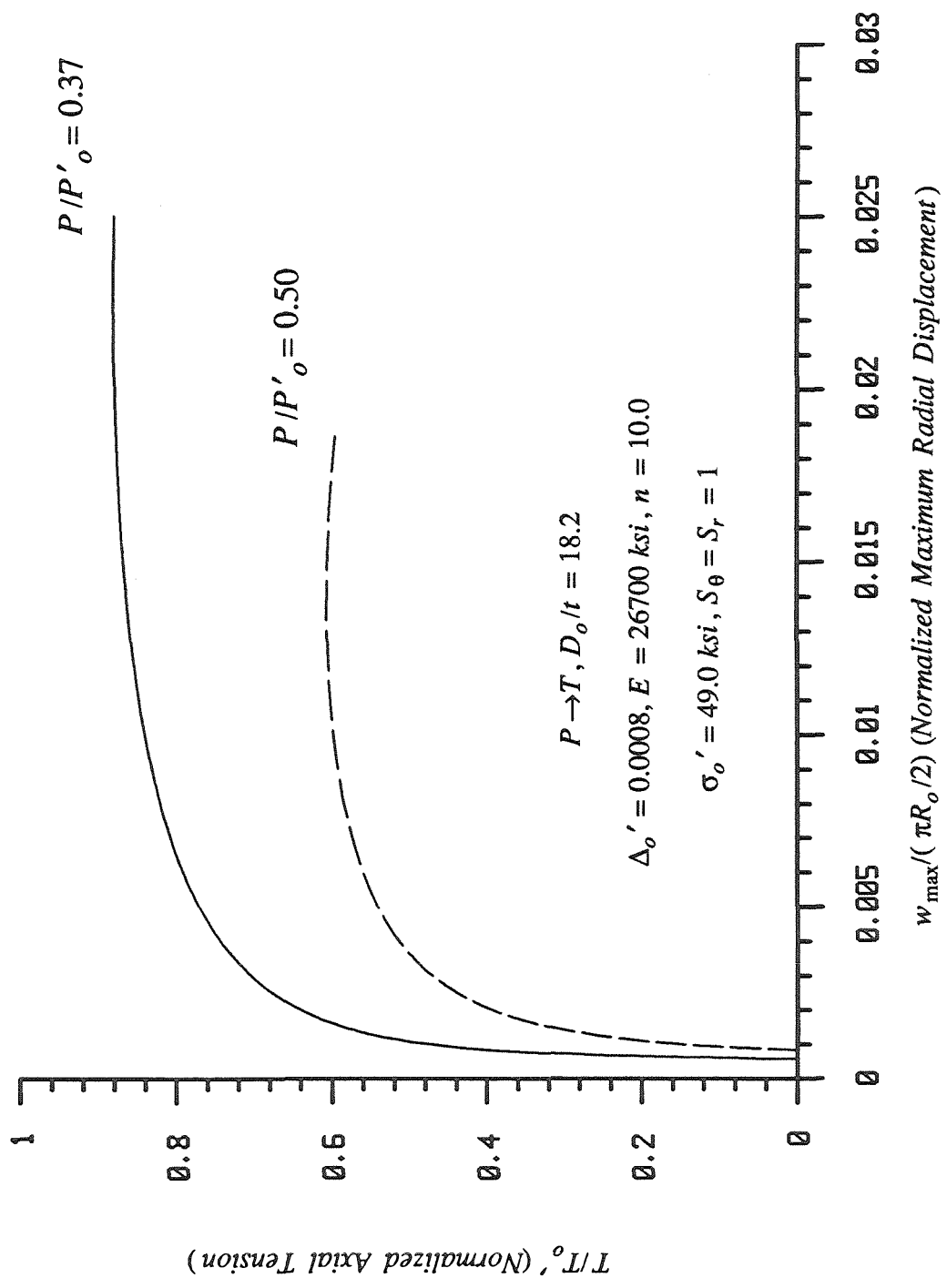
Figure 3.2b. Predicted Tension-Deflection Responses at Different Prescribed Pressures.
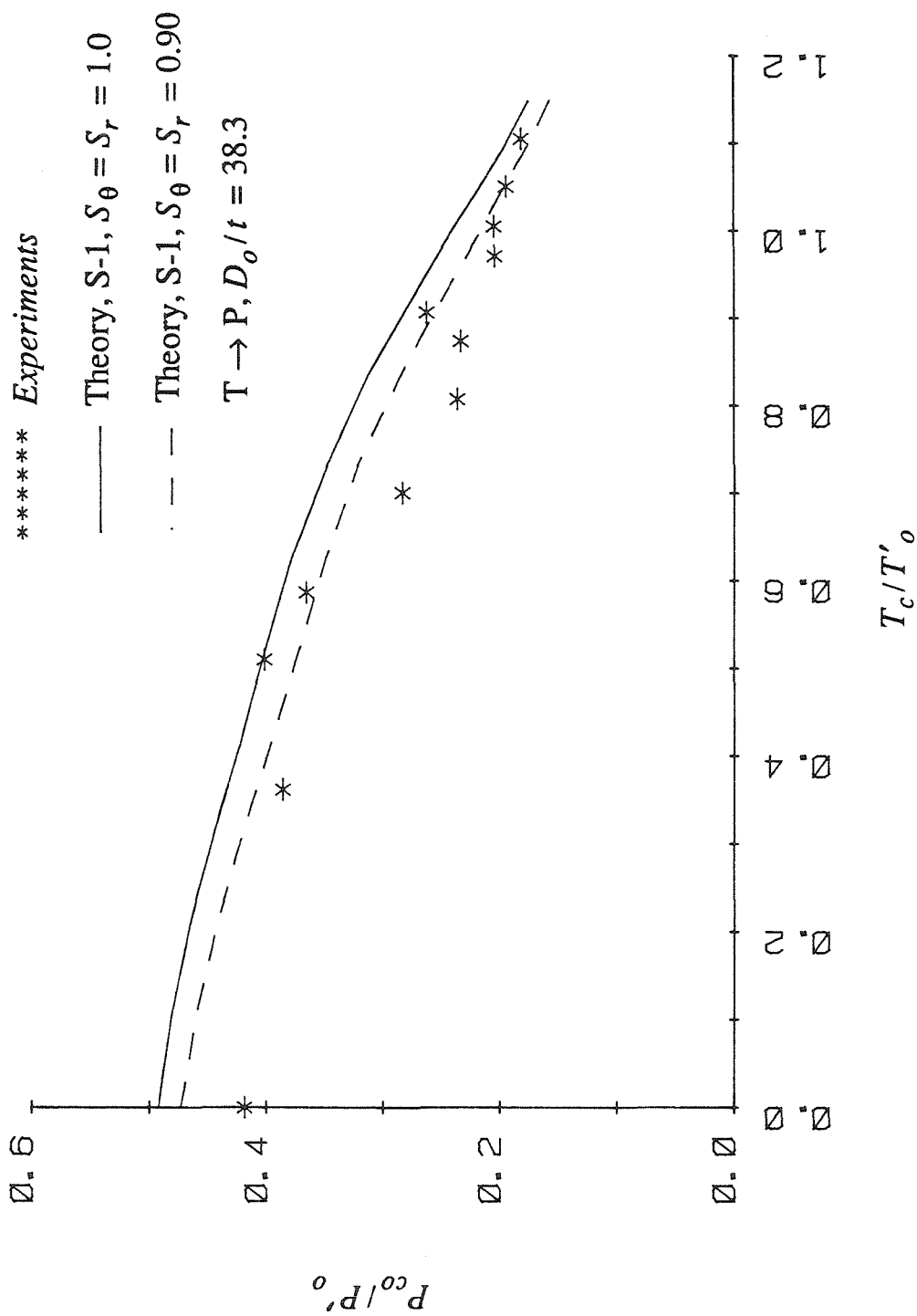
Figure 4.1a. Experimental and Predicted Tension-Pressure Collapse Envelope (T→P) for $D_o/t = 38.3$
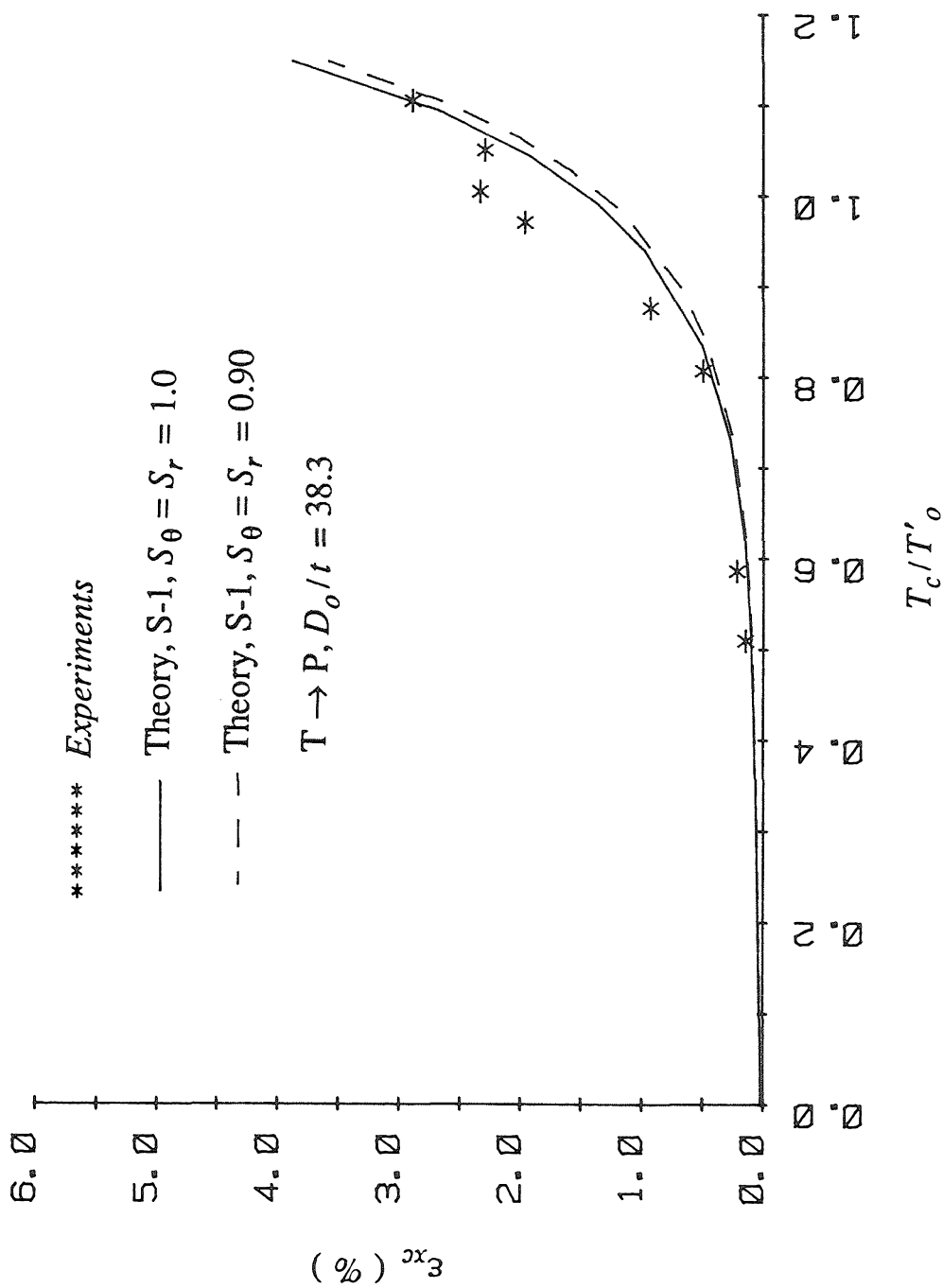
Figure 4.1b. Experimental and Predicted Axial Strain-Tension Collapse Envelope (T→P) for $D_o/t = 38.3$
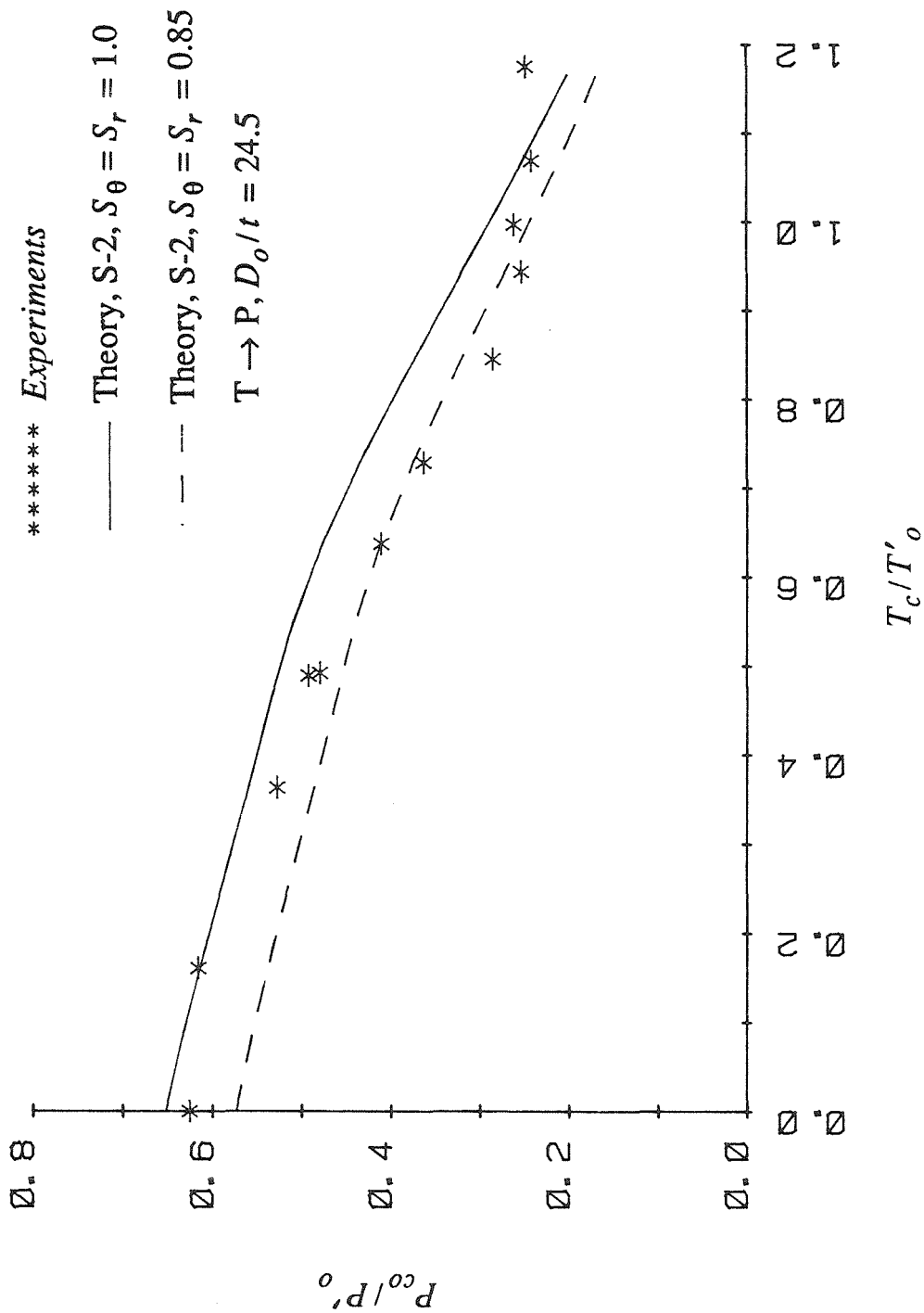
Figure 4.2a. Experimental and Predicted Tension-Pressure Collapse Envelope (T→P) for $D_o/t = 24.5$
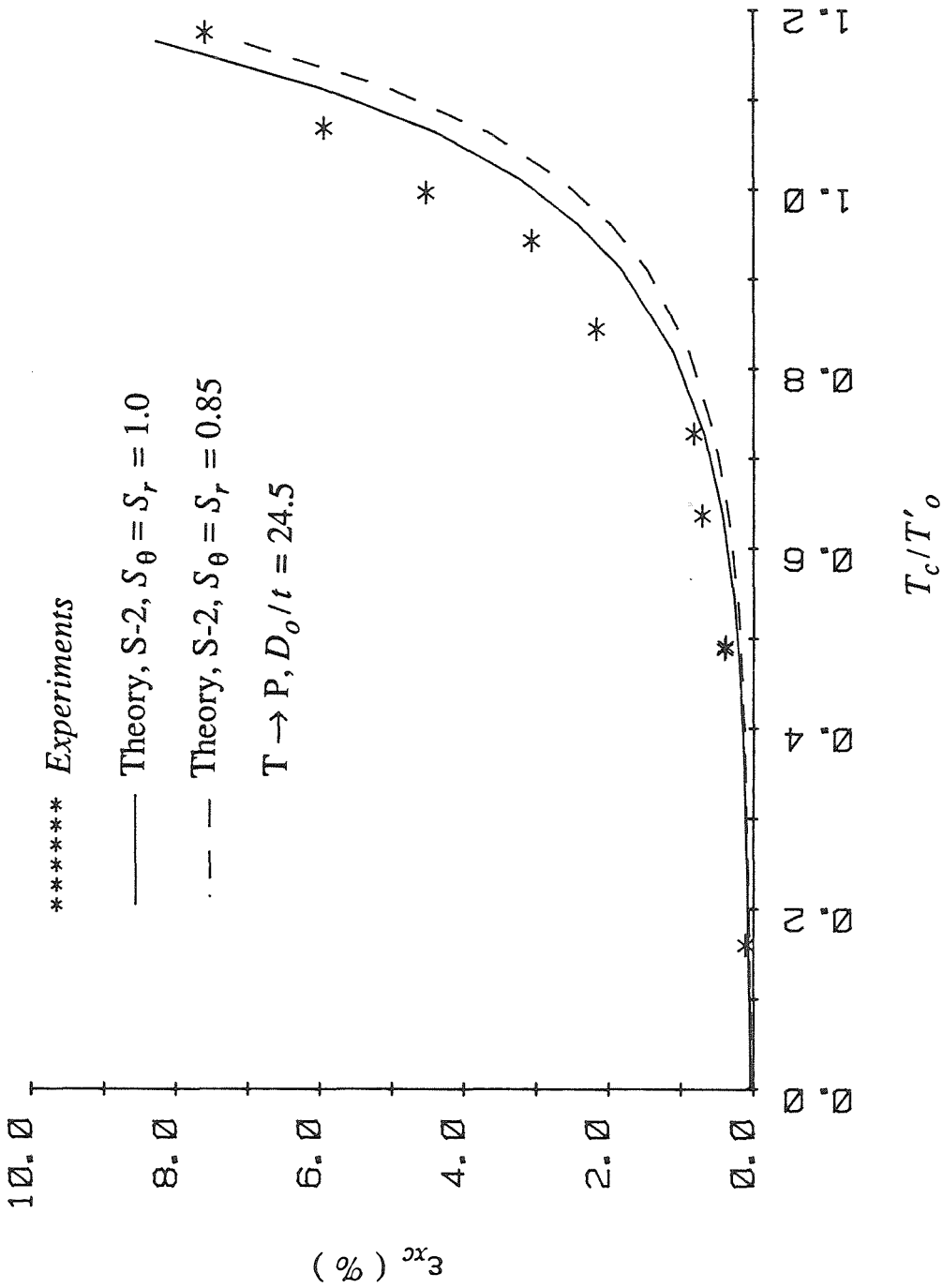
Figure 4.2b. Experimental and Predicted Axial Strain-Tension Collapse Envelope (T→P) for $D_o/t = 24.5$
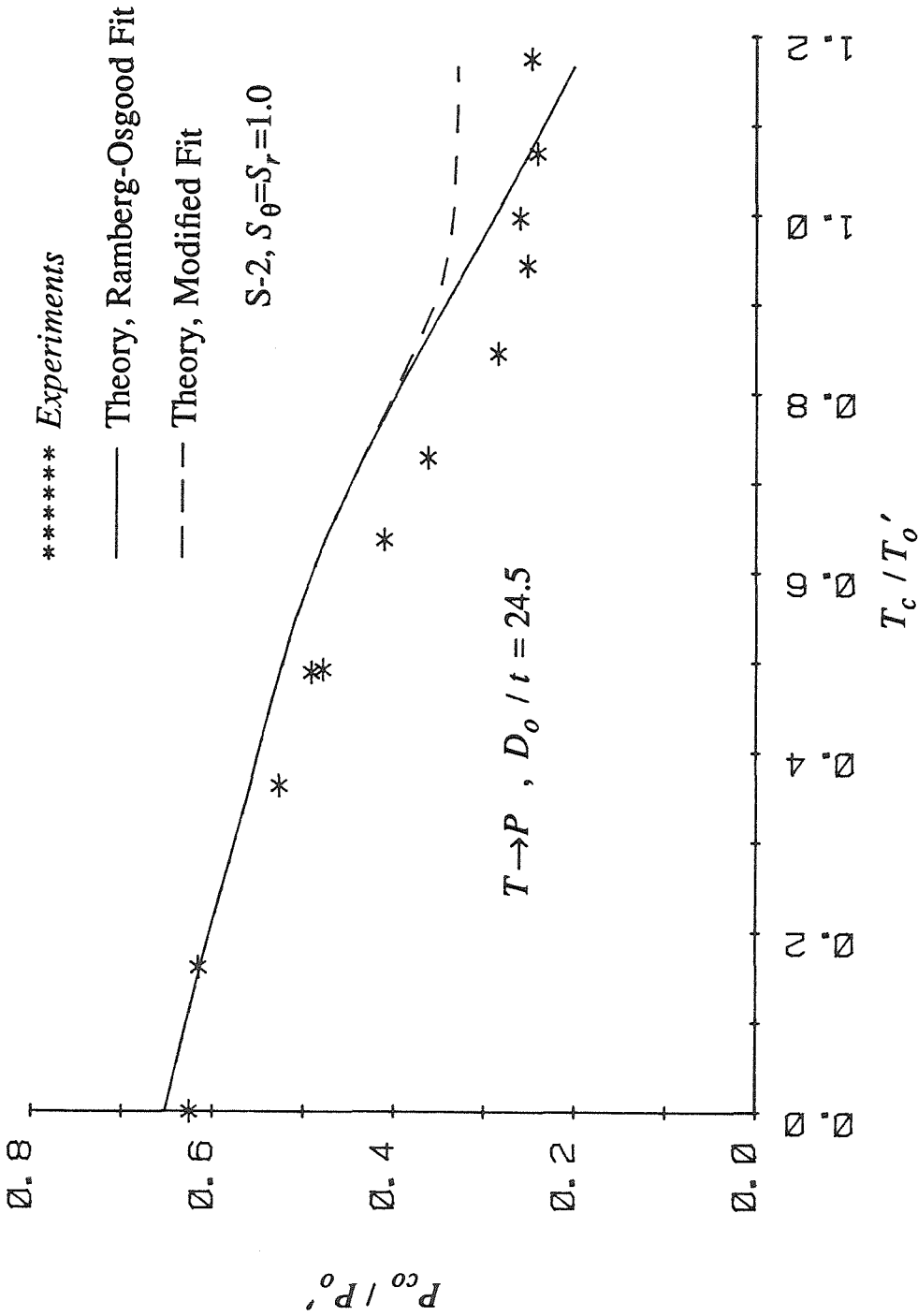
Figure 4.2c. Experimental Tension-Pressure Collapse Envelope and Predictions Based on Ramberg-Osgood Fit and Modified Fit Representations for the Stress-Strain Behavior (T→P, D_o/t=24.5, 304 steel).
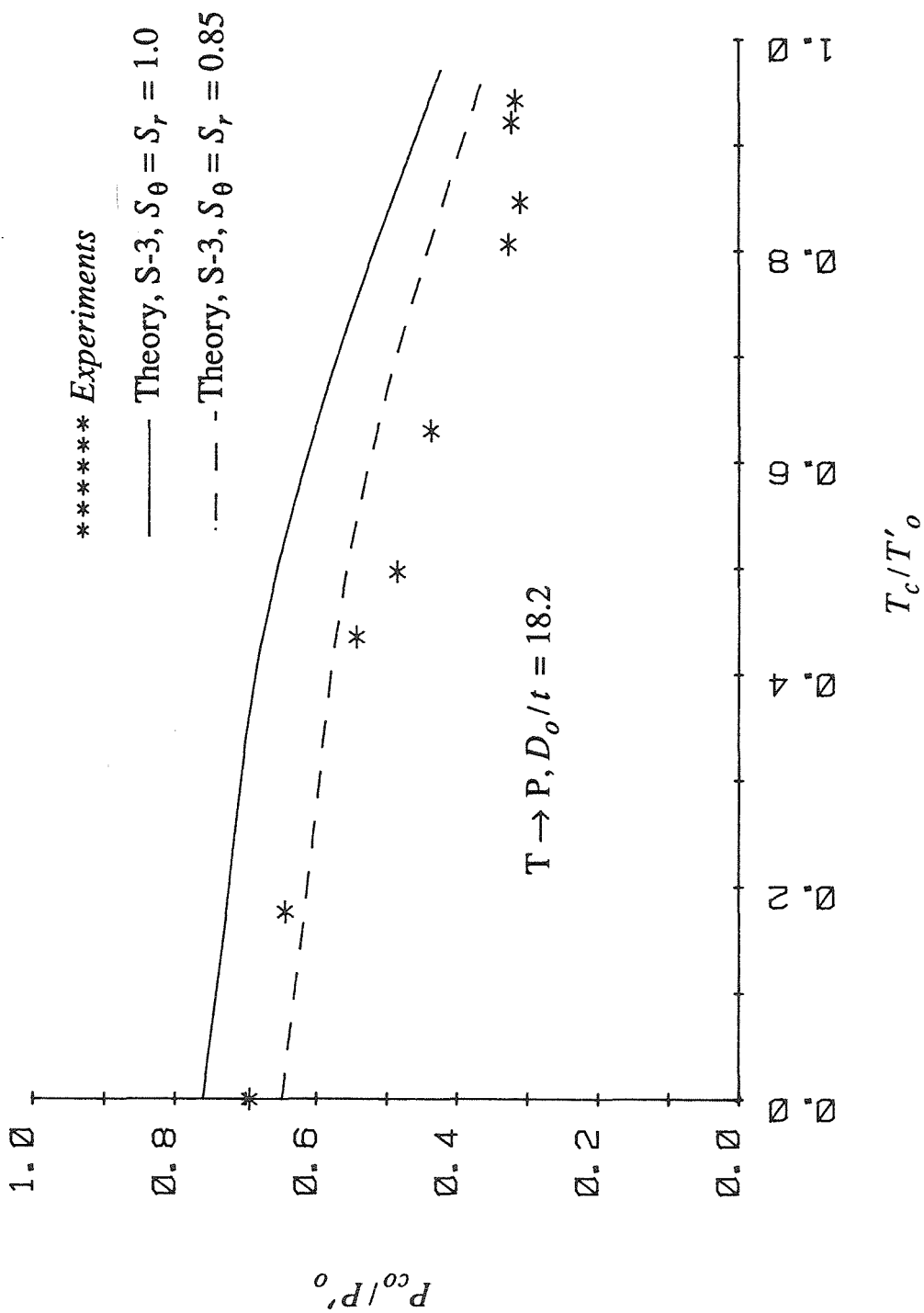
Figure 4.3a. Experimental and Predicted Tension-Pressure Collapse Envelope (T→P) for $D_o/t = 18.2$
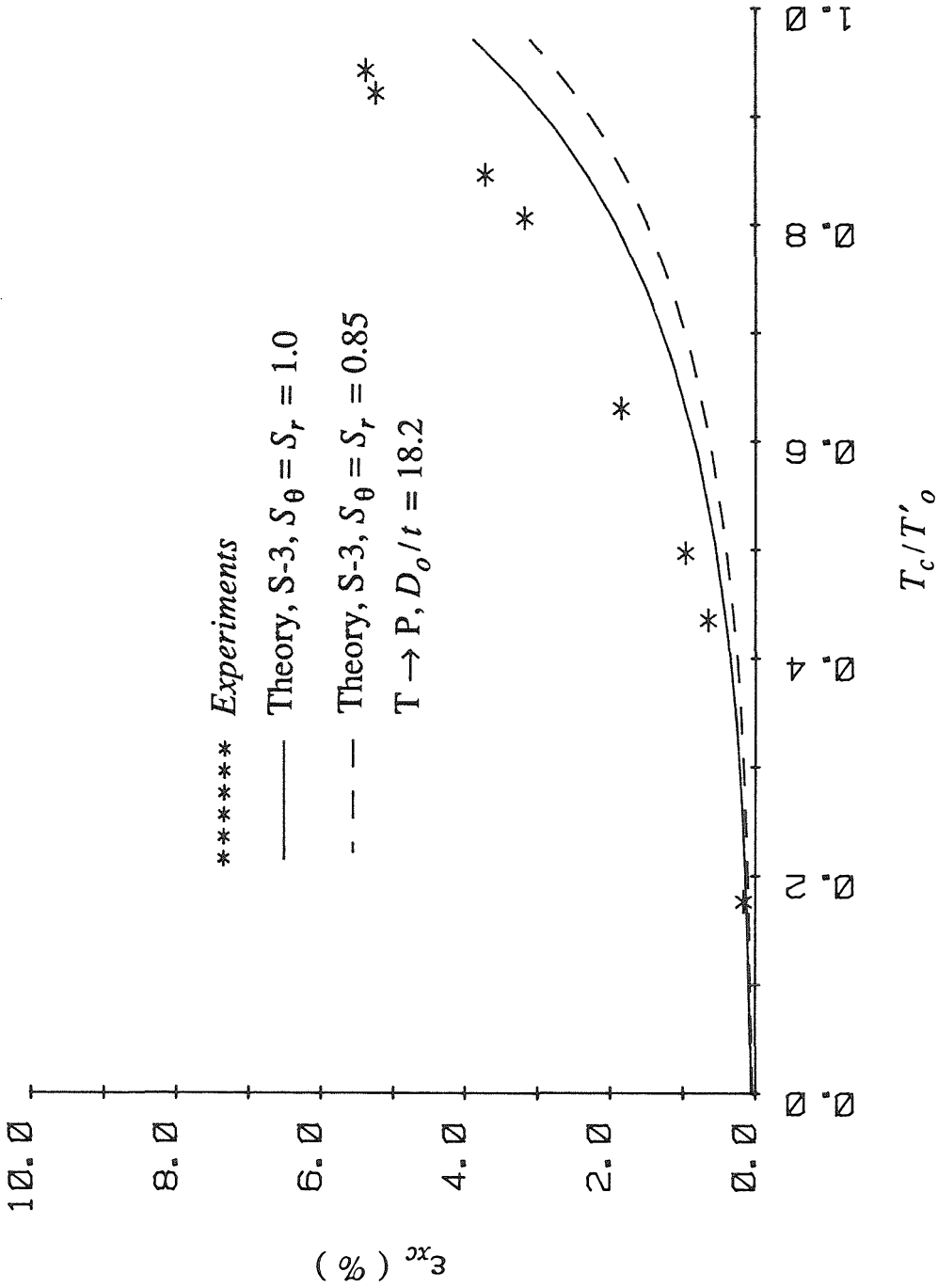
Figure 4.3b.   Experimental and Predicted Axial Strain-Tension Collapse Envelope (T→P) for
$D_o/t = 18.2$
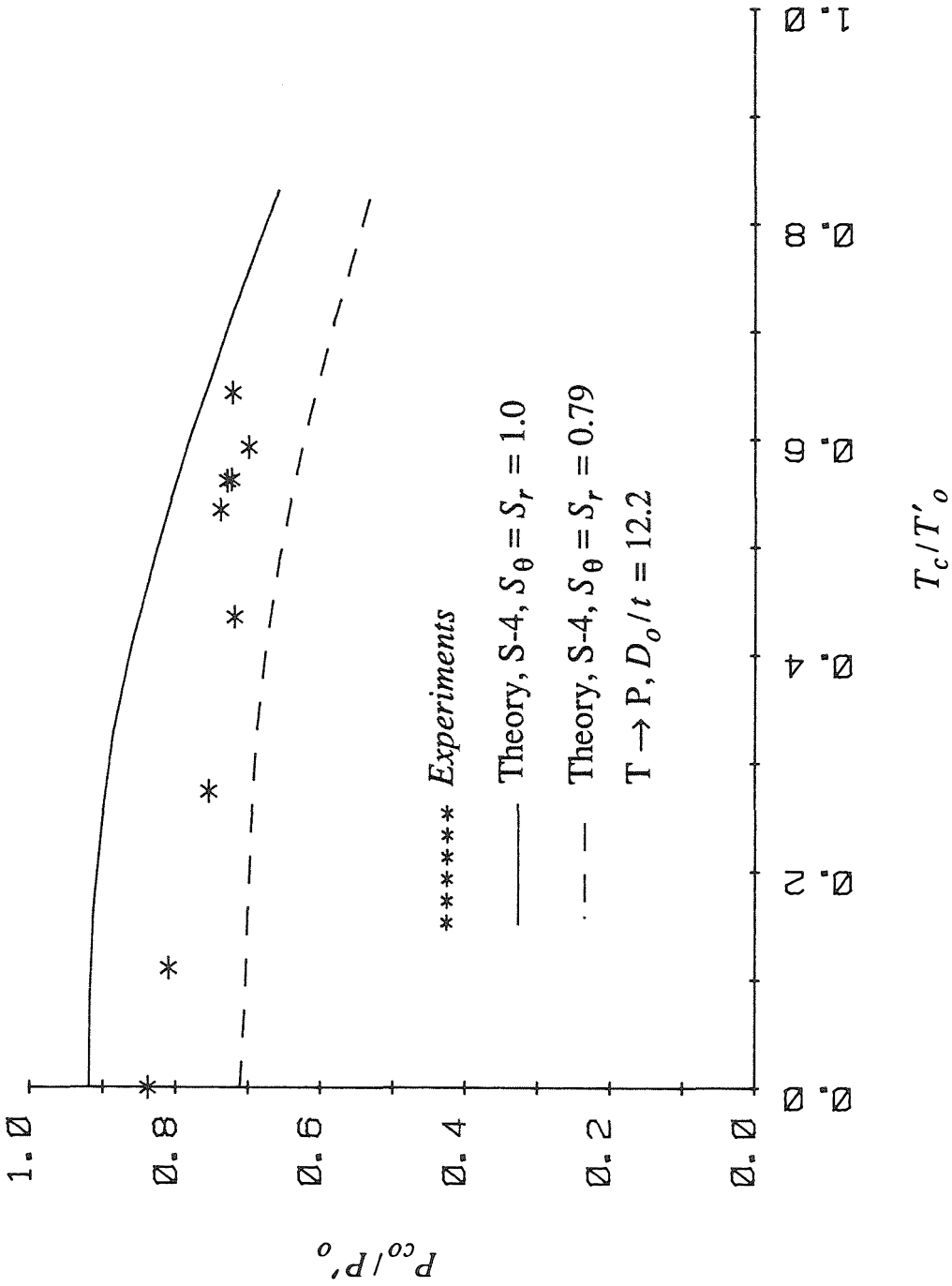
Figure 4.4a.   Experimental and Predicted Tension-Pressure Collapse Envelope (T→P) for $D_o/t = 12.2$
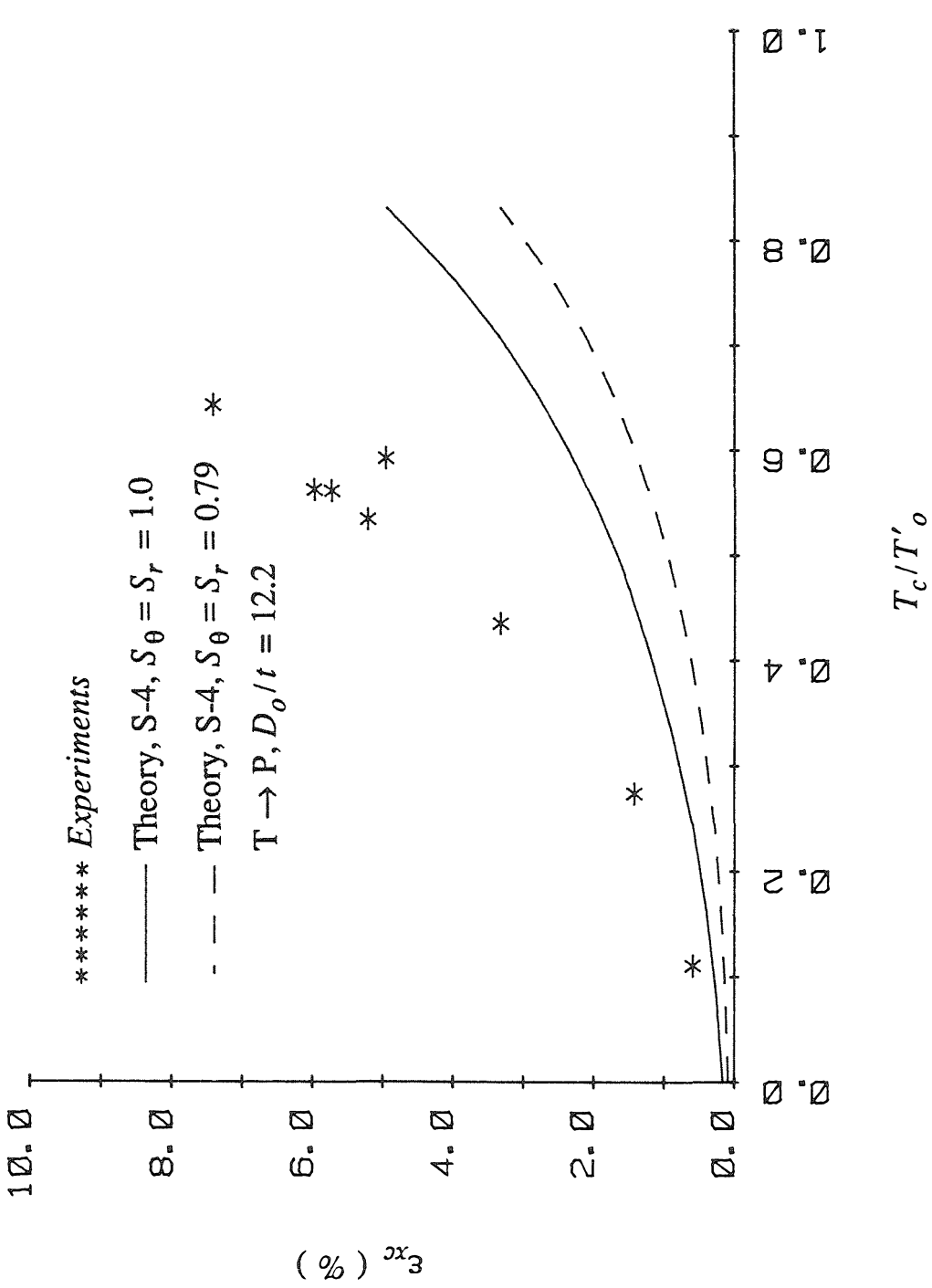
Figure 4.4b Experimental and Predicted Axial Strain-Tension Collapse Envelope (T→P) for $D_o/t = 12.2$
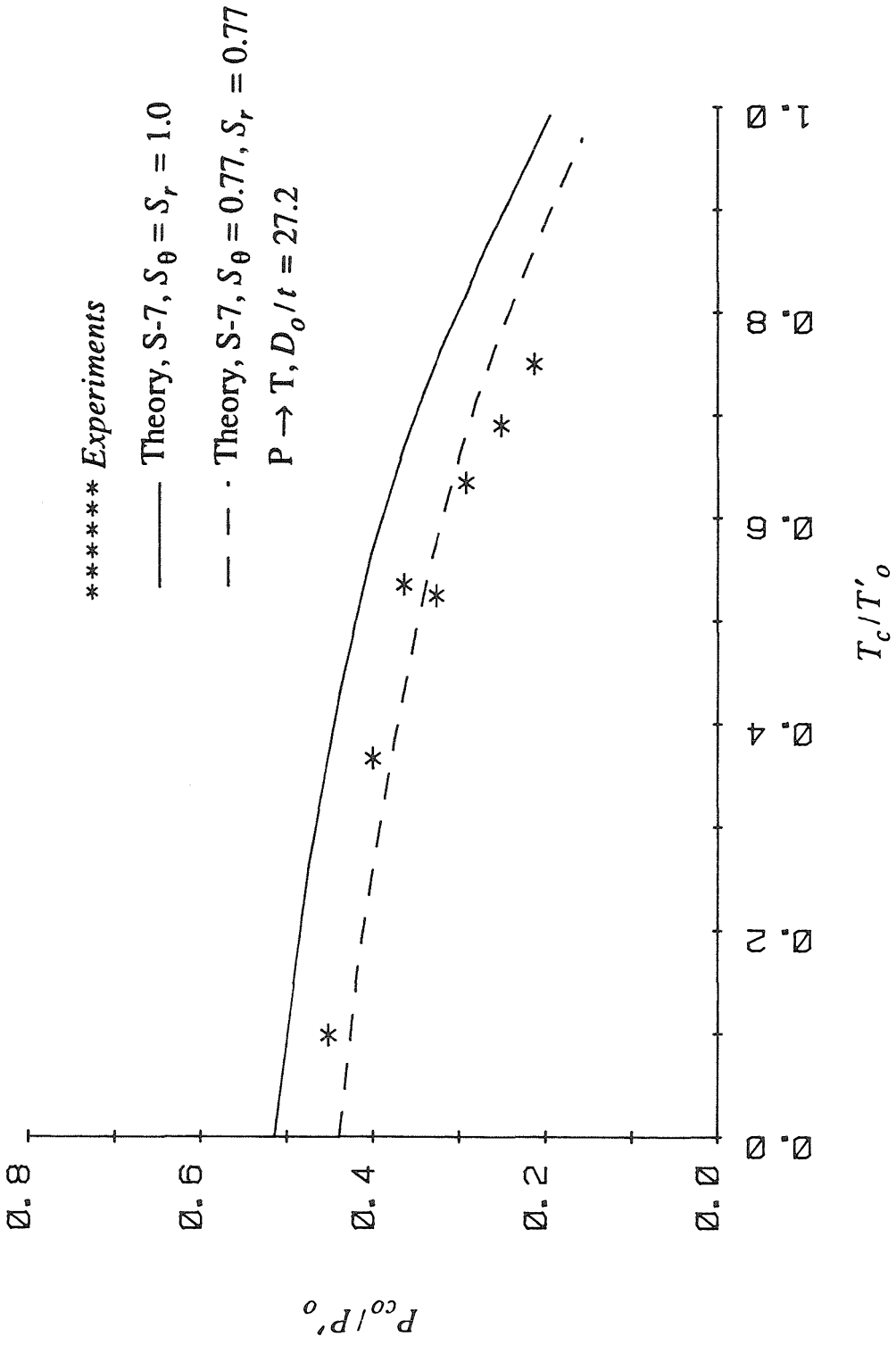
Figure 4.5a. Experimental and Predicted Tension-Pressure Collapes Envelope (P→T) for $D_o/t=27.2$.
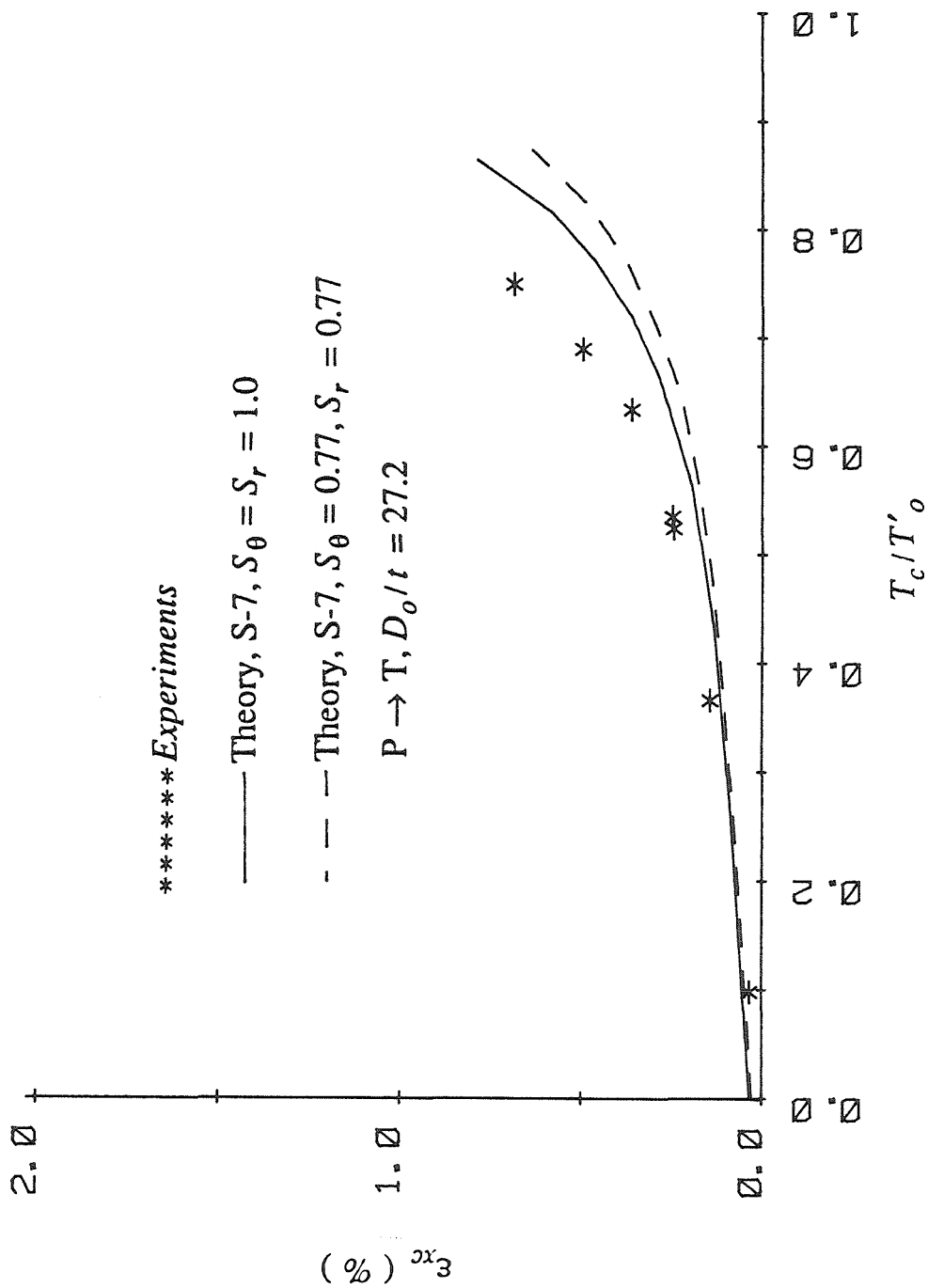
Figure 4.5b. Experimental and Predicted Axial Strain Tension Collapse Envelope (P→T) for $D_o/t=27.2$
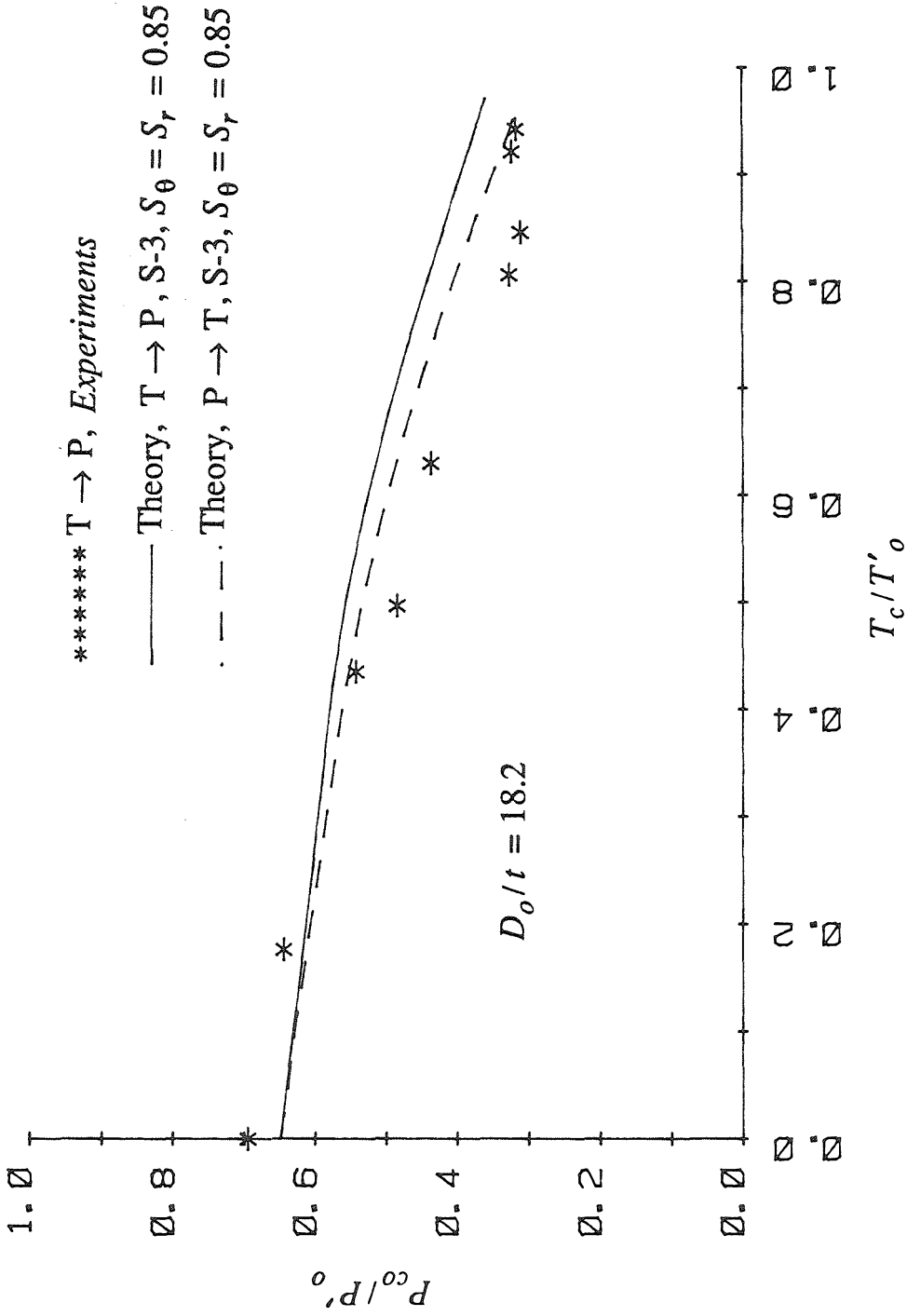
Figure 4.6.   Effect of Loading Path on Tension-Pressure Collapse Envelope ($D_o/t = 18.2$)
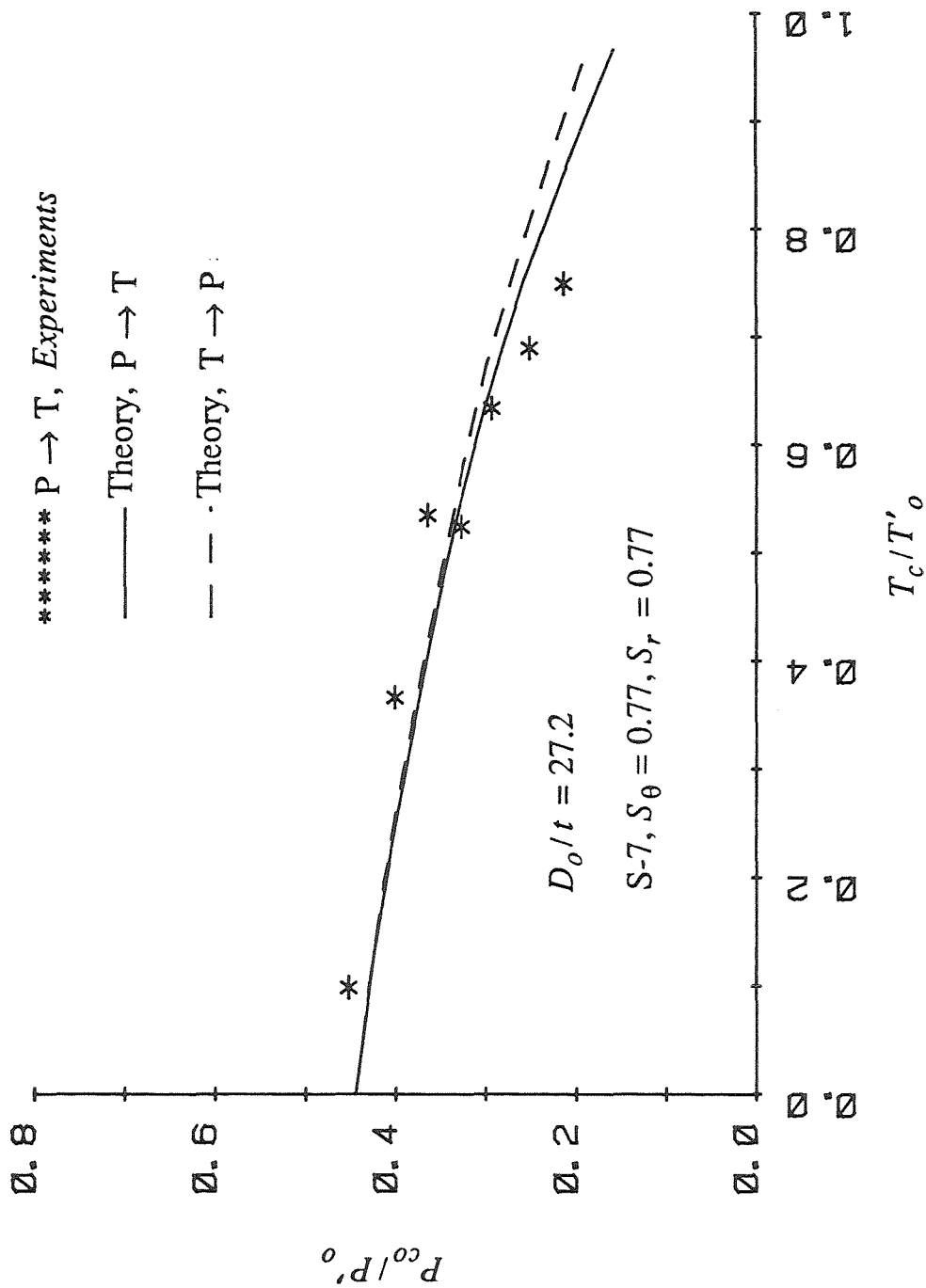
Figure 4.7.   Effect of Loading Path on Tension-Pressure Collapse Envelope ($D_o/t = 27.2$)
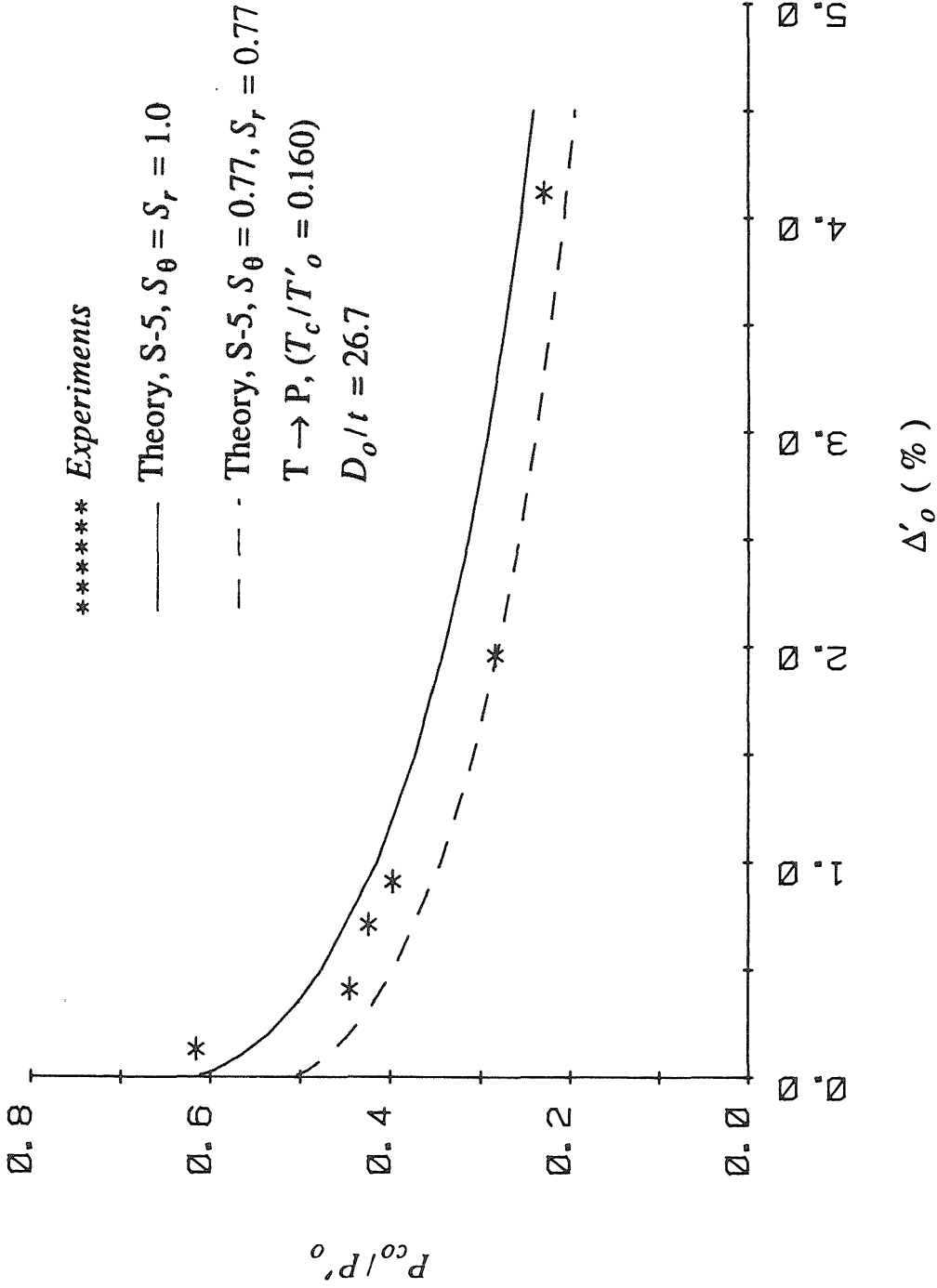
Figure 4.8a. Experimental and Predicted Collapse Strength of Initially Ovalized Tubes $(D_o/t = 26.7, T \rightarrow P, T_c/T'_o = 0.160)$
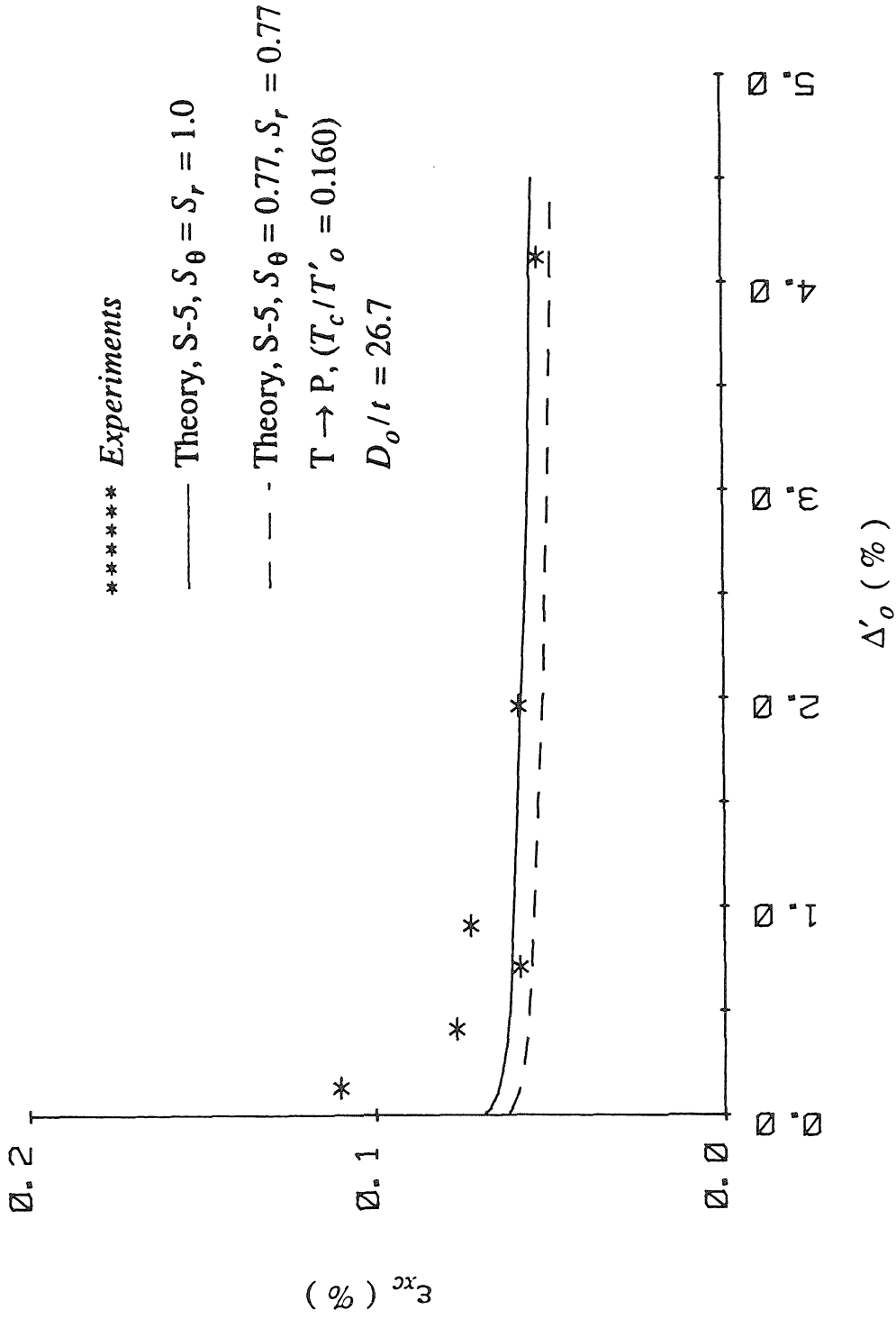
Figure 4.8b. Experimental and Predicted Axial Strain Response at Collapse of Initially Ovalized Tubes ($D_o/t = 26.7$, $T \rightarrow P$, $T_c/T'_o = 0.160$)

-96-
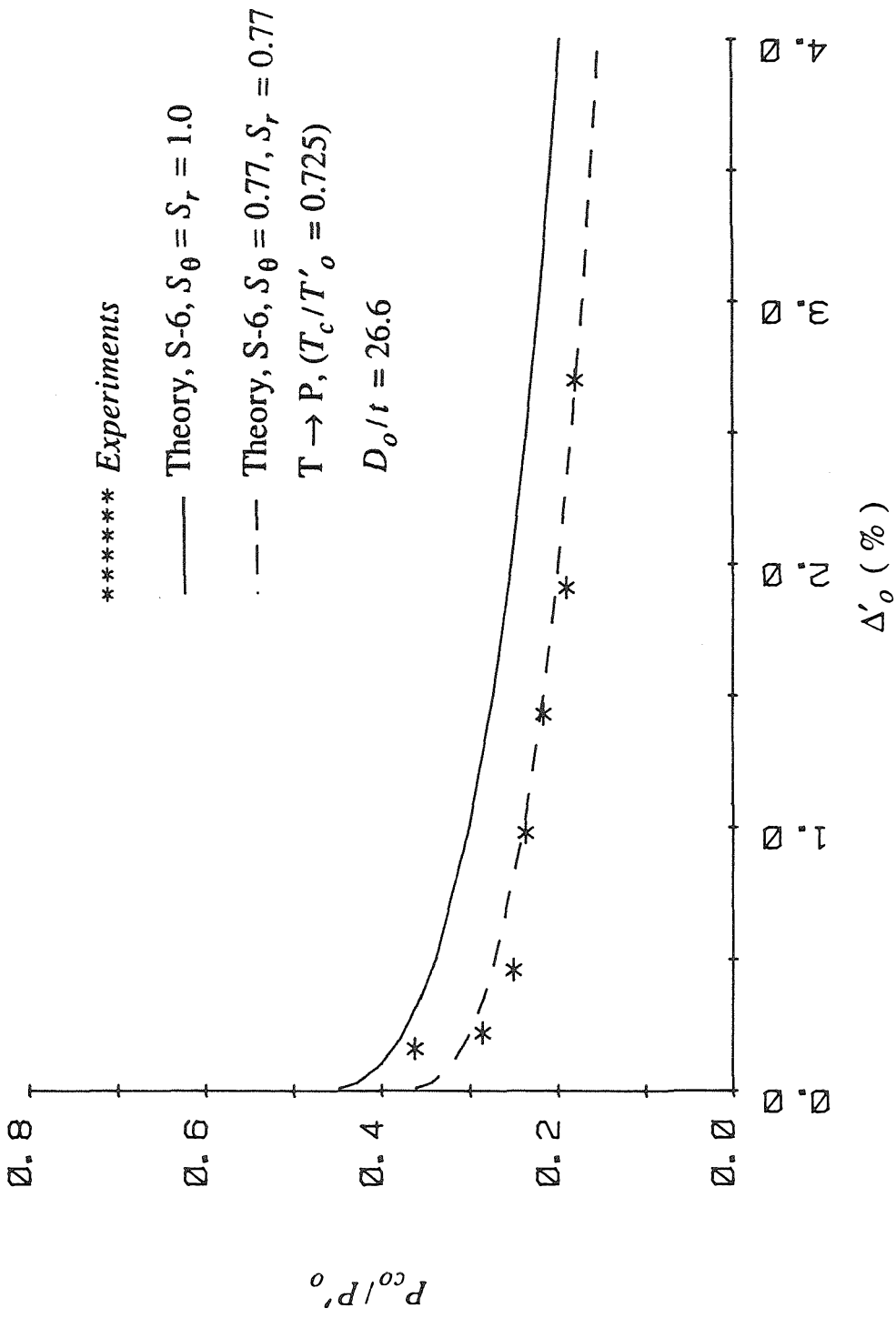
Figure 4.9a. Experimental and Predicted Collapse Strength of Initially Ovalized Tubes
$(D_o/t = 26.6, \; T \rightarrow P, \; T_c/T'_o = 0.725)$
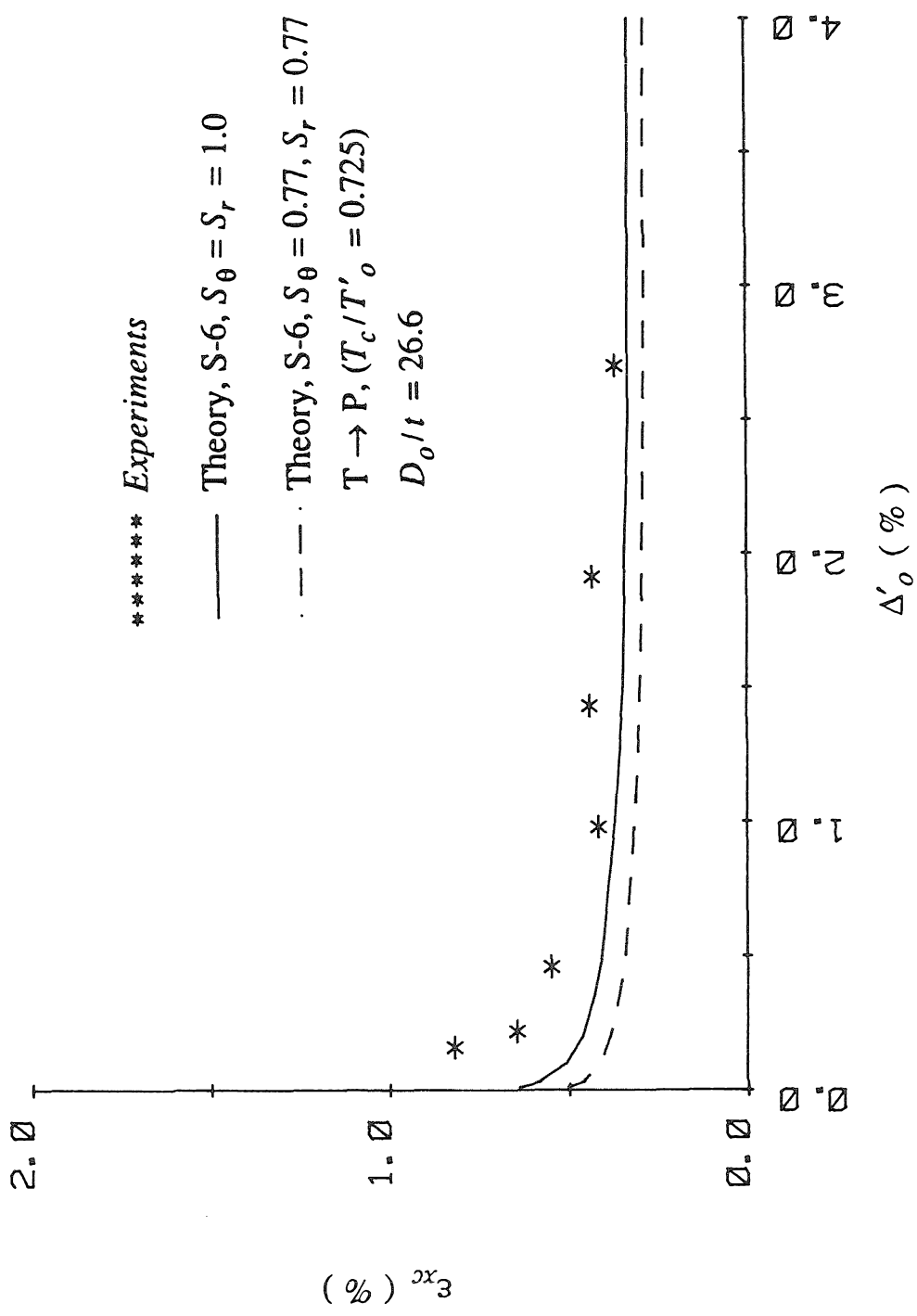
Figure 4.9b. Experimental and Predicted Axial Strain Response at Collapse of Initially Ovalized Tubes ($D_o/t = 26.6$, $T \to P$, $T_c/T'_o = 0.725$)
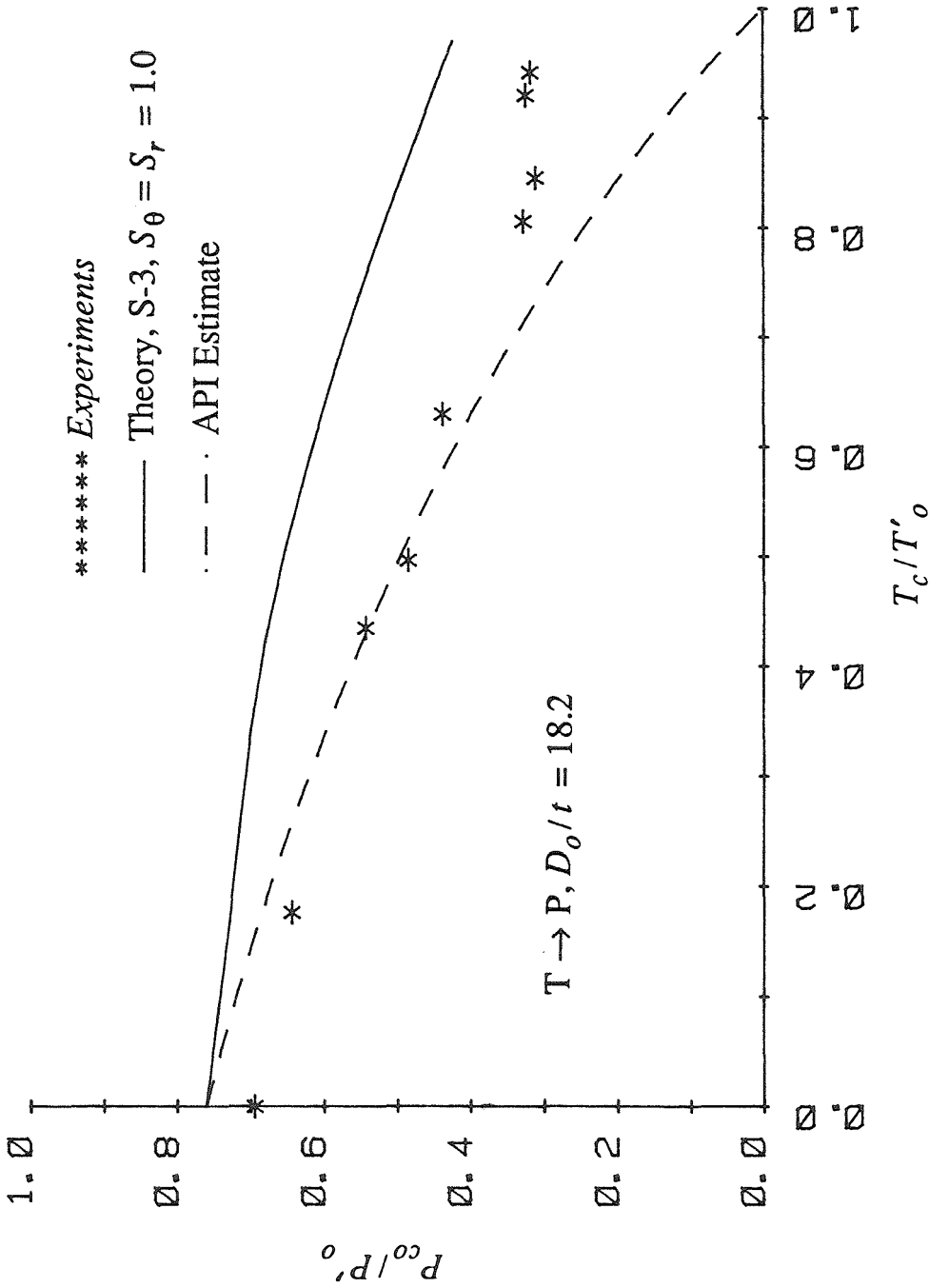
Figure 4.10. Comparison Between Current Theoretical and Experimental Results and API Estimate ($T \to P$, $D_o/t = 18.2$)
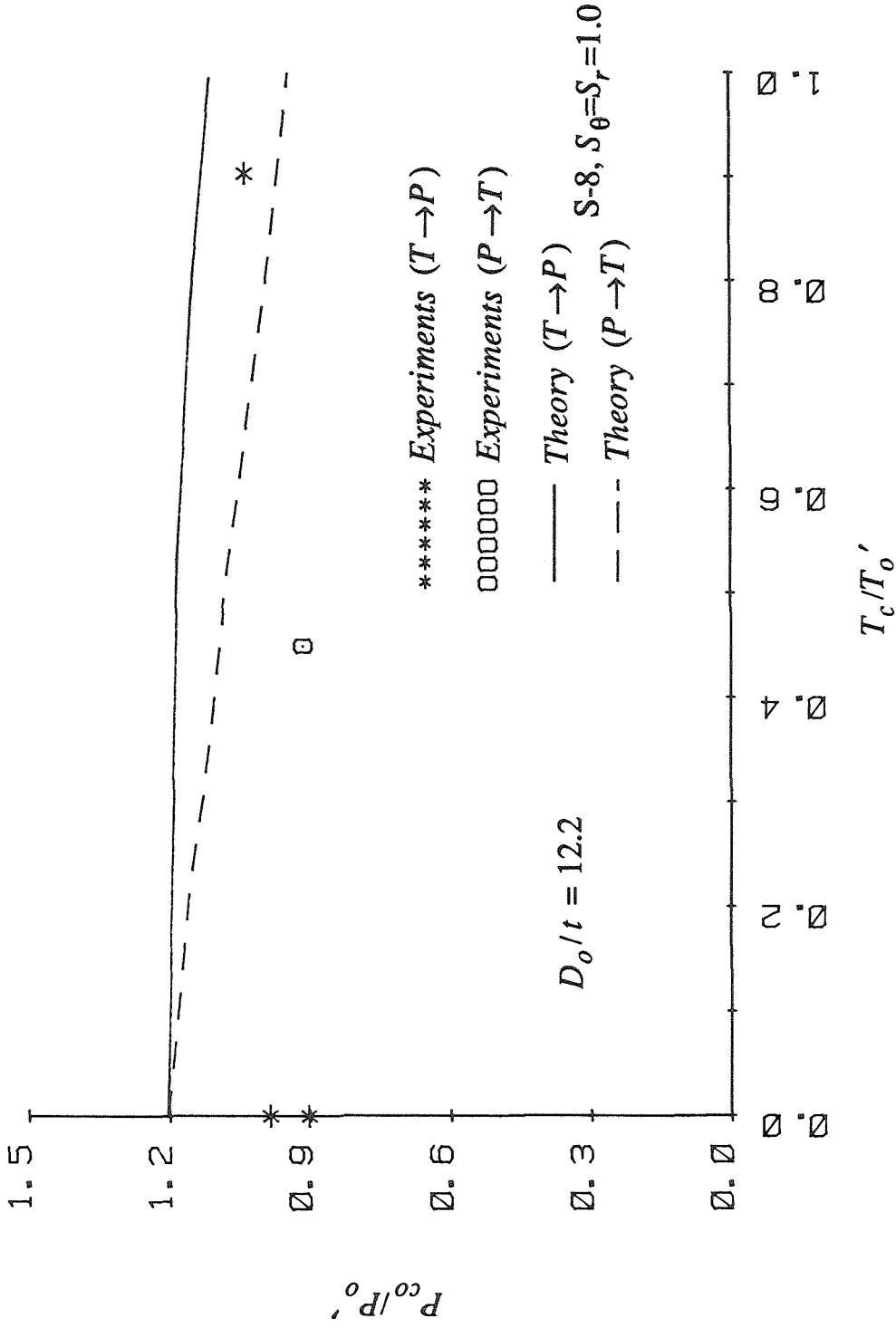
Figure 4.11a. Experimental and Predicted Tension-Pressure Collapse Envelopes for D_o/t=12.2 (6061-O Aluminum, T→P and P→T).
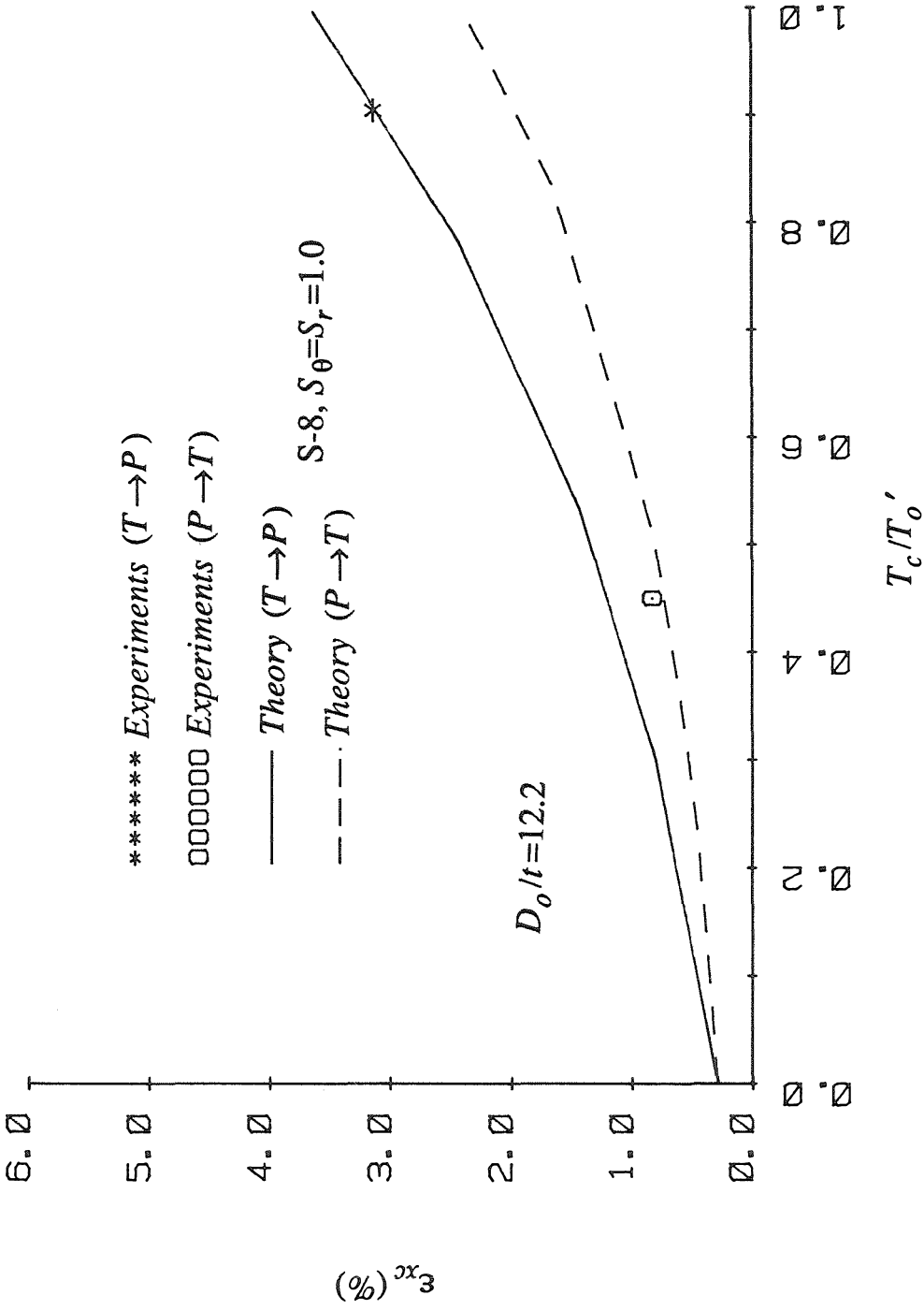
Figure 4.11b. Experimental and Predicted Axial Strian-Tension Collapse Envelope for $D_o/t=12.2$ (6061-O Aluminum, T→P and P→T).
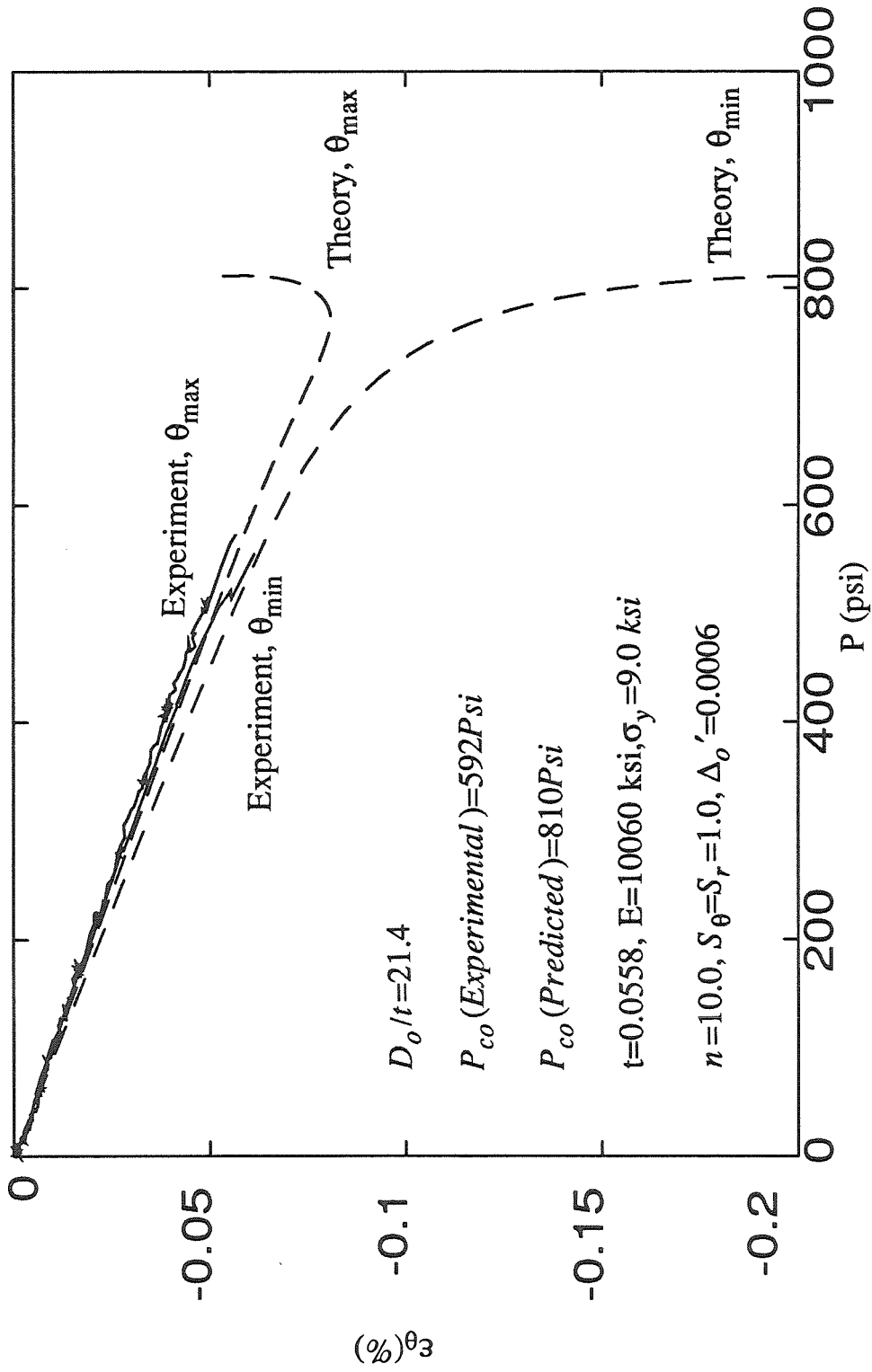
Figure 4.12a. Experimental and Predicted Pressure-Hoop Strain Response at Axial Location "L" and Circumferential Positions θ_{max} and θ_{min} (6061-O Aluminum, D_o/t=21.4, T=0).
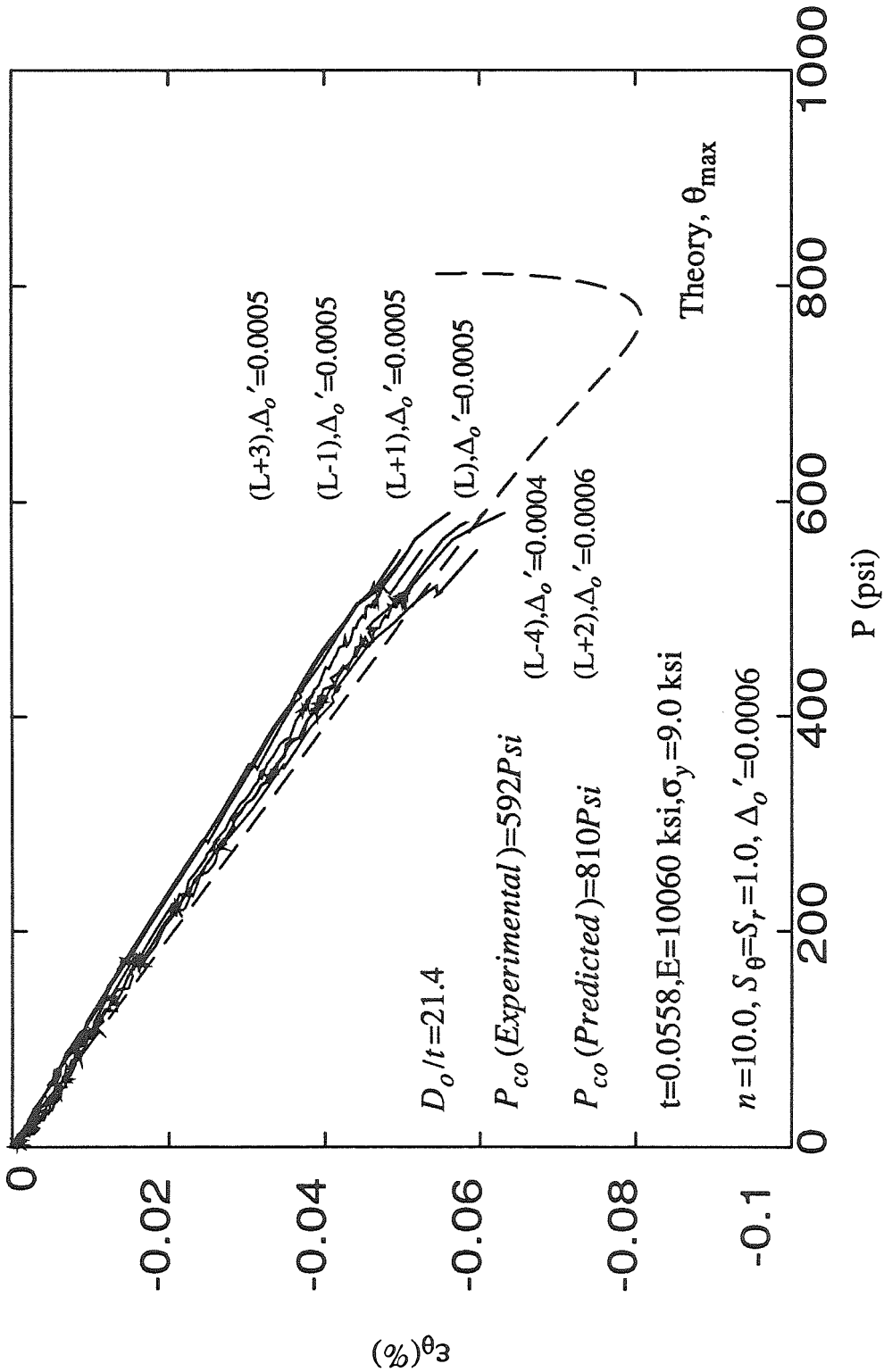
Figure 4.12b. Experimental Pressure-Hoop Strain Response at the Circumferential Position θ_{max} for Different Axial Locations Compared with the Prediction (6061-O Aluminum, D_o/t=21.4, T=0).
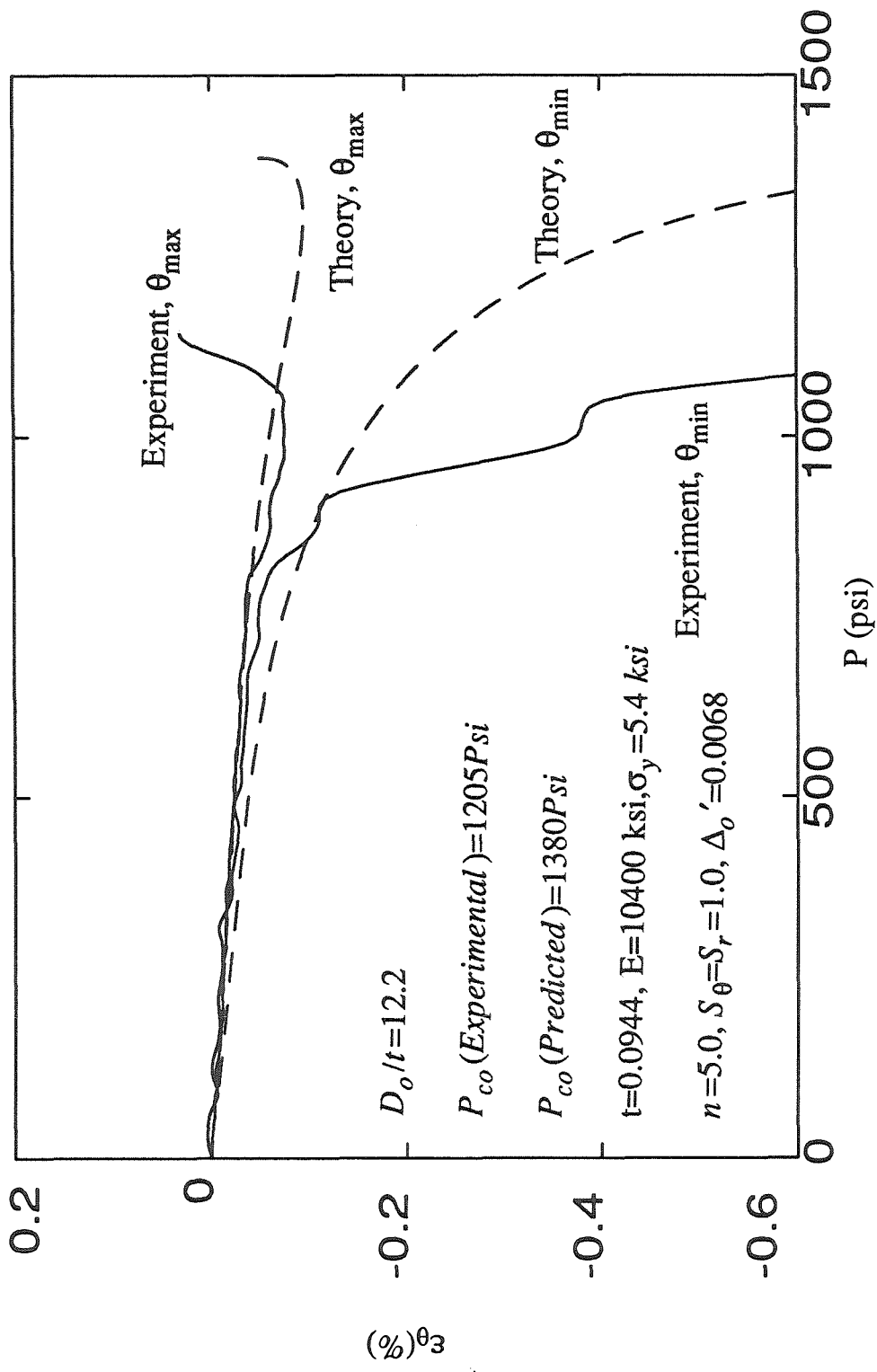
Figure 4.13a. Experimental and Predicted Pressure-Hoop Strain Response at Axial Location "L" and Circumferential Positions θ_{max} and θ_{min} (6061-O Aluminum, D_o/t=12.2, T=0).
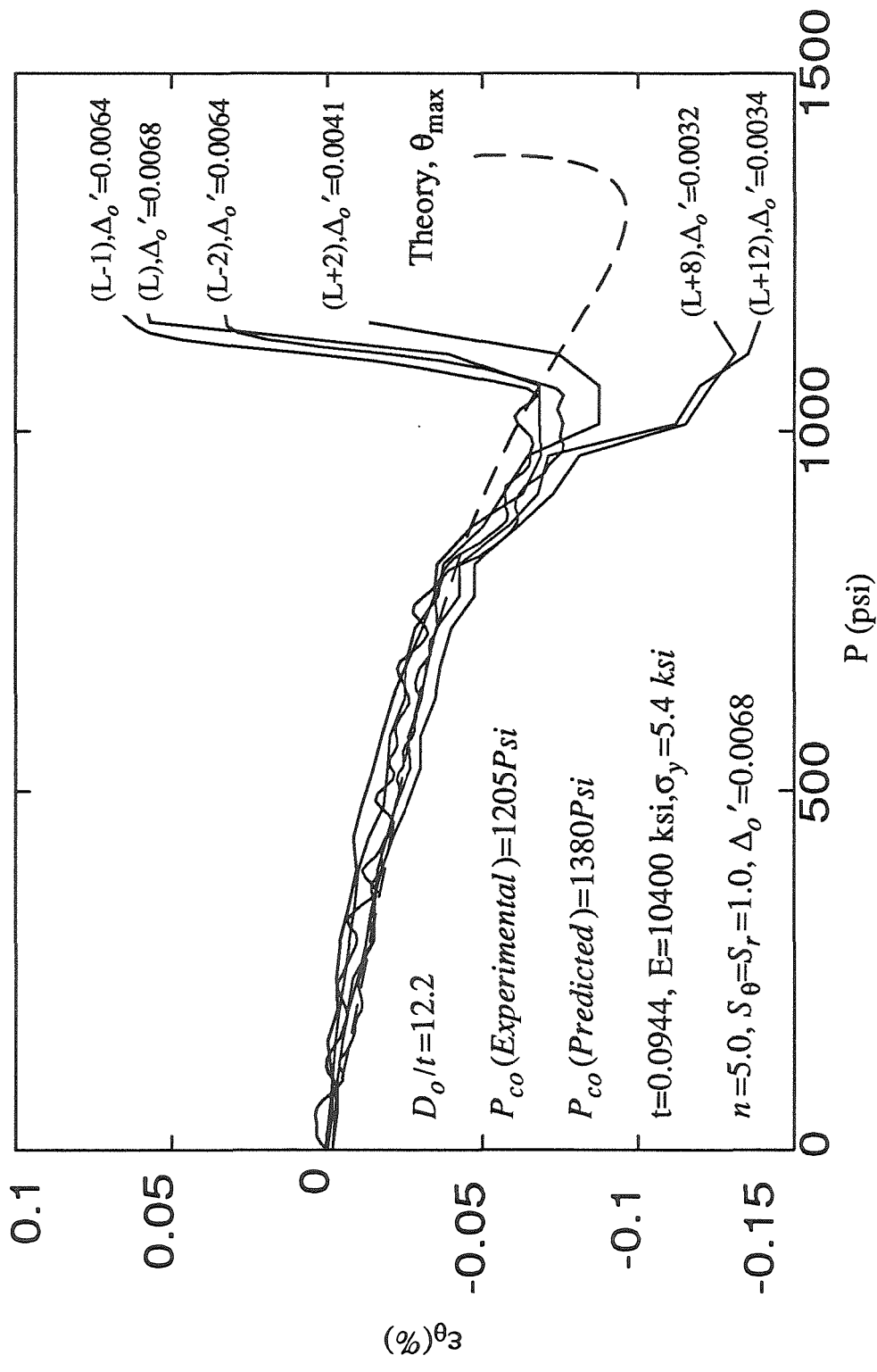
Figure 4.13b. Experimental Pressure-Hoop Strain Response at the Circumferential Position θ_{max} for Different Axial Locations Compared with the Prediction (6061-O Aluminum, $D_o/t=12.2$, T=0).
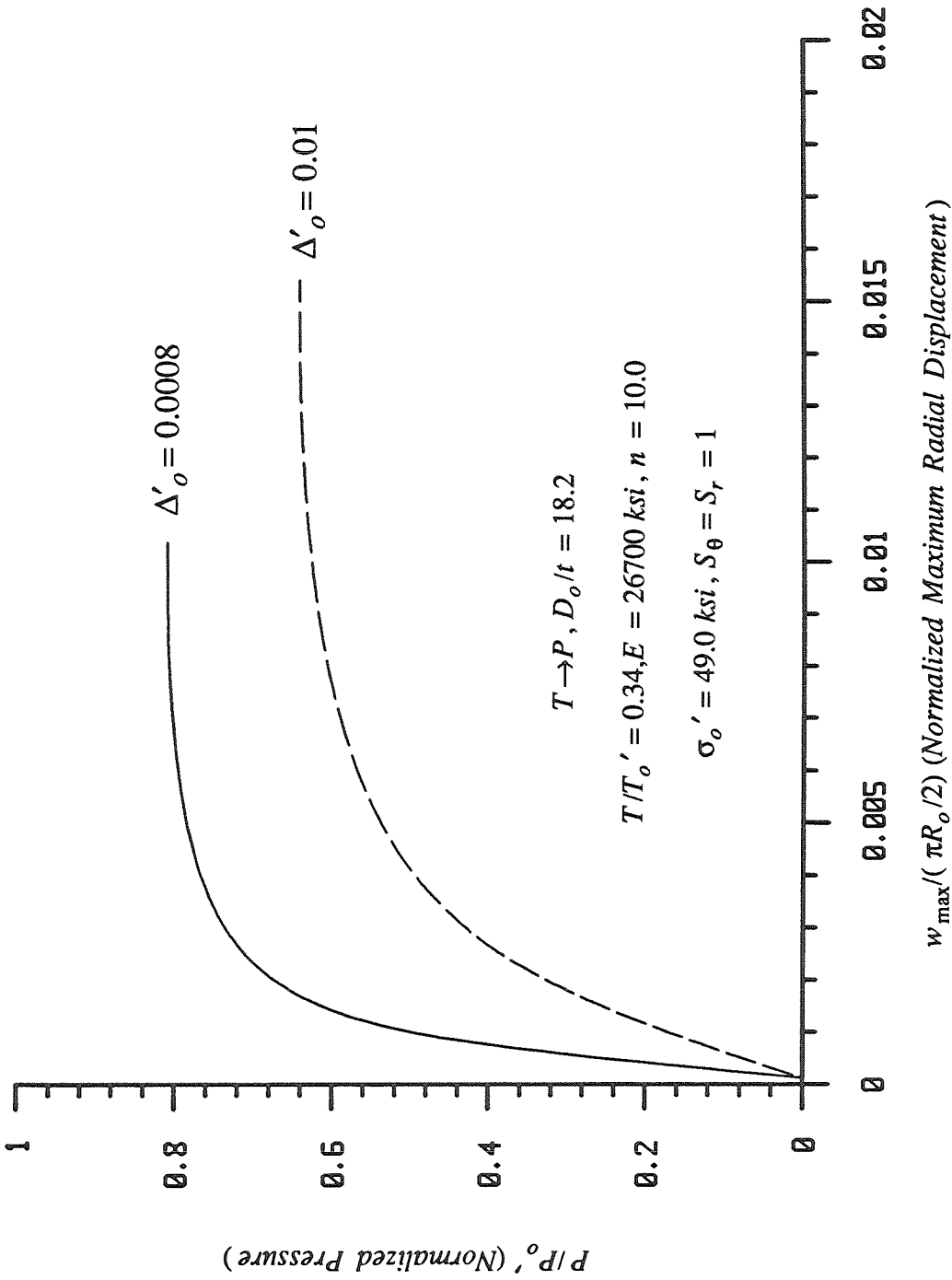
Figure 5.1a. Predicted Pressure-Deflection Responses at Different Values of Initial Ovality ($T \rightarrow P$, $T/T_o' = 0.34$).
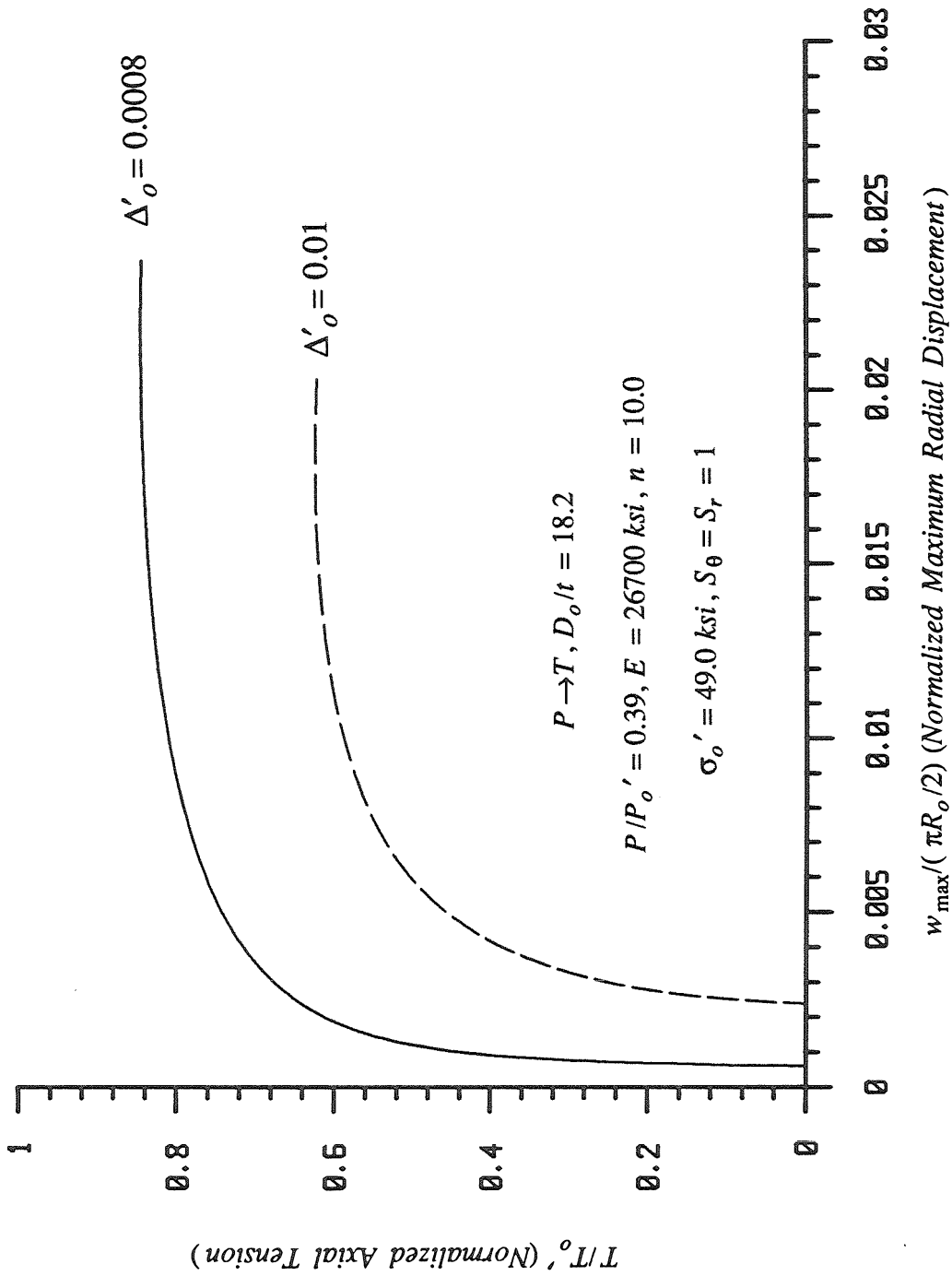
Figure 5.1b. Predicted Tension-Deflection Responses at Different Values of Initial Ovality ($P \to T$, $P/P_o' = 0.39$)
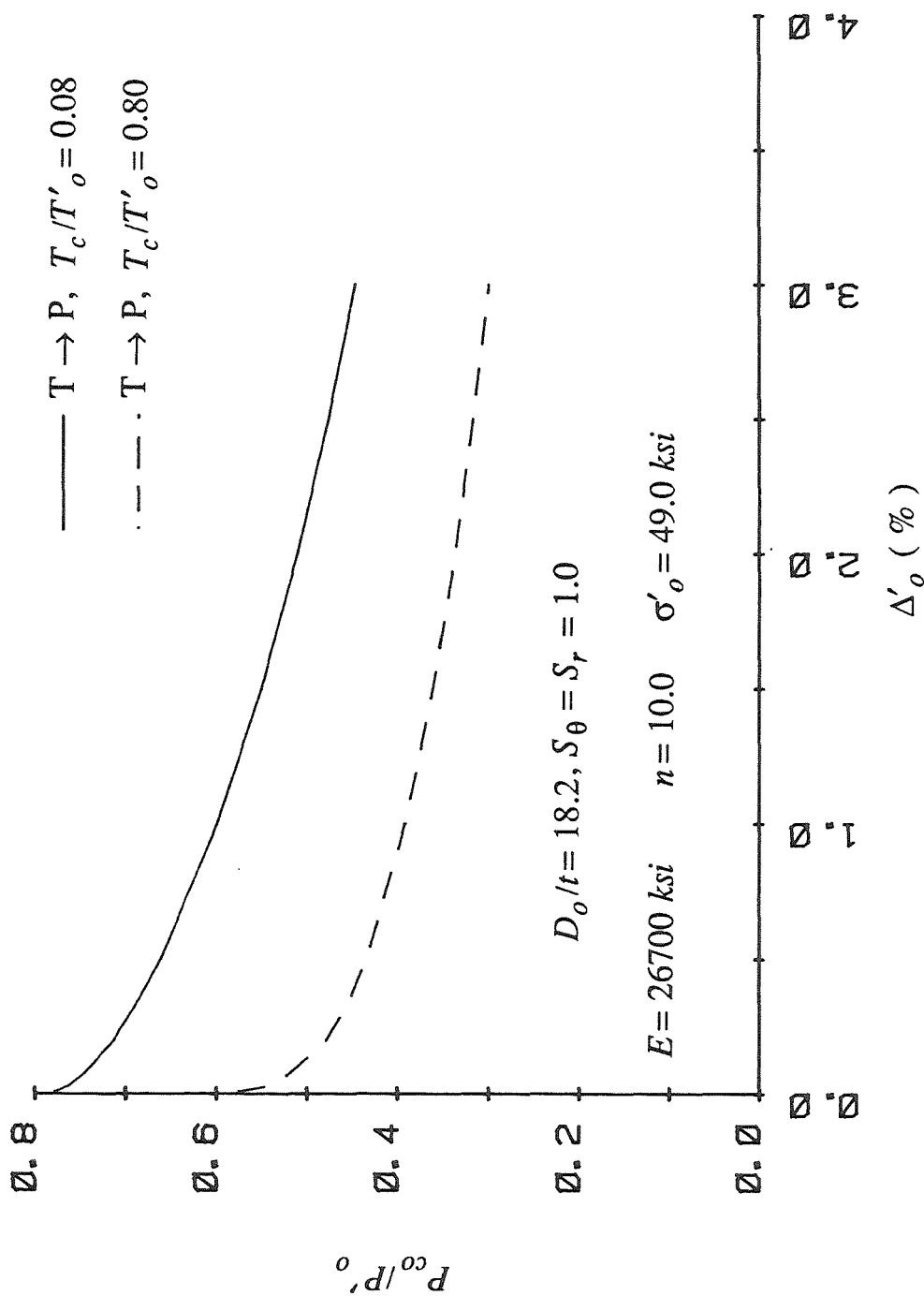
Figure 5.2. Predicted Collapse Strength for Different Values of Initial Ovality, Under Biaxial Loading ($T \rightarrow P$, $D_o/t = 18.2$)
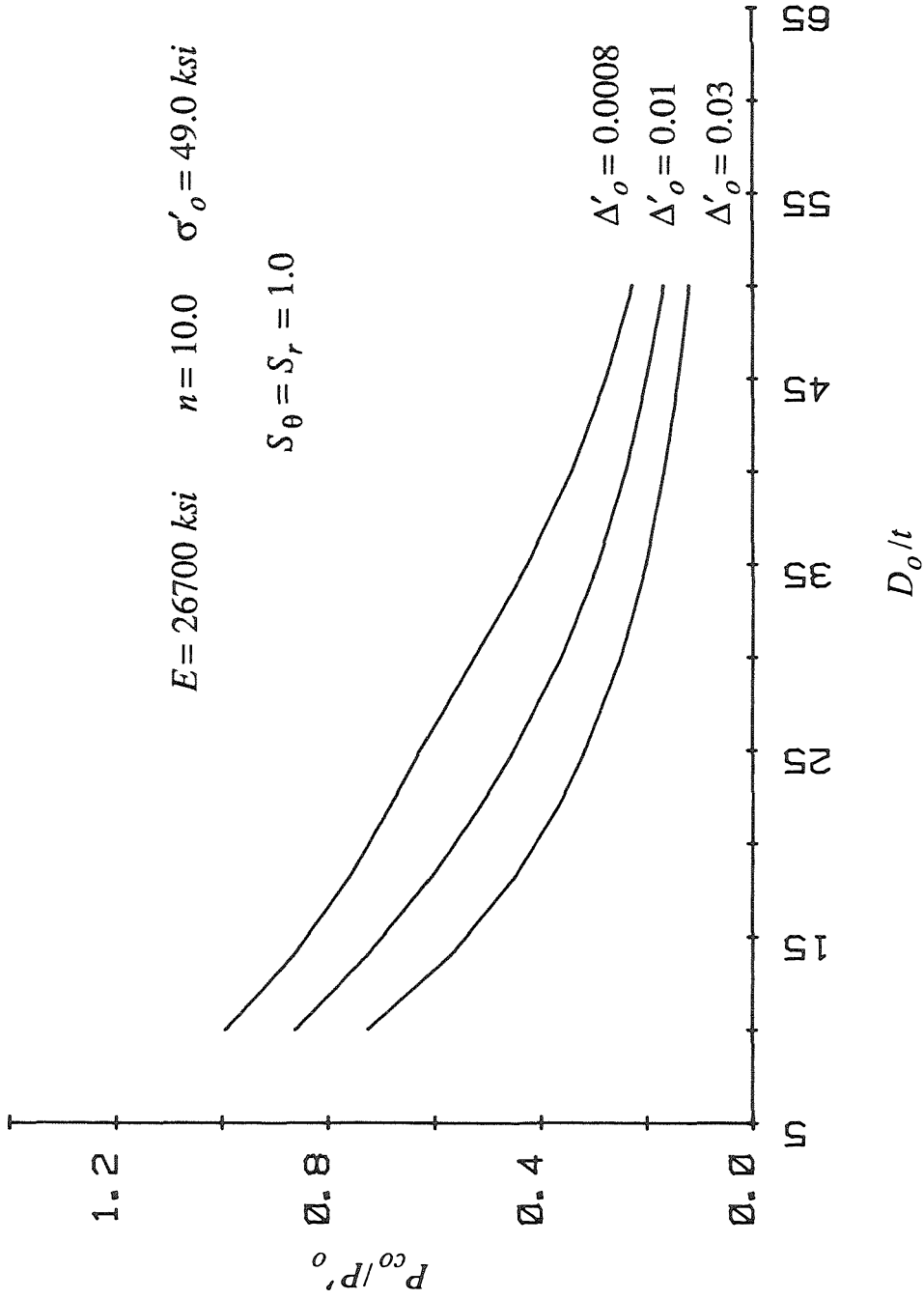
Figure 5.3.   Predicted Collapse Pressure for Different Values of Initial Ovality (T=0)
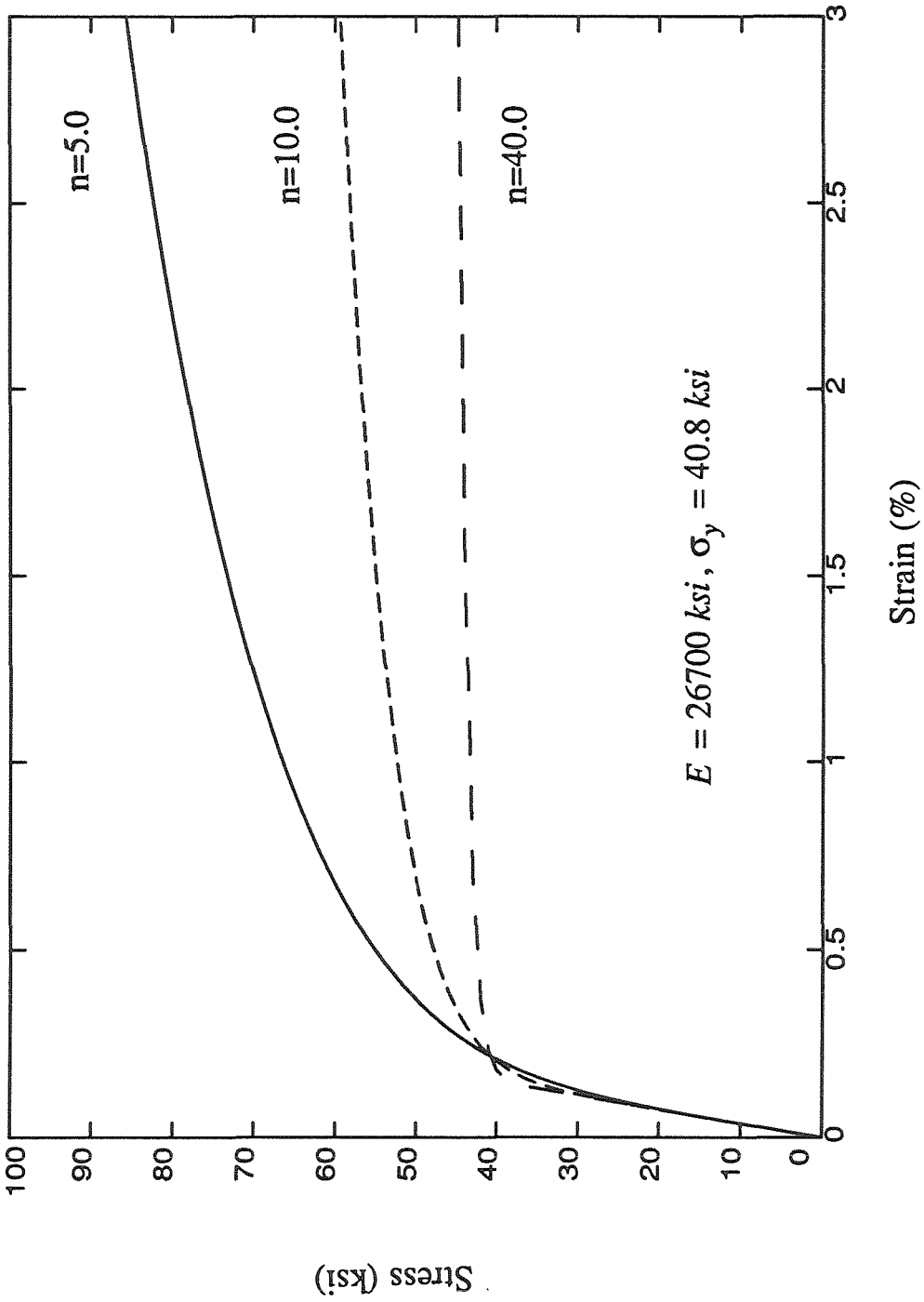
Figure 5.4.   Stress-Strain Curves Represented by the Ramberg-Osgood Fit
for Three Different Values of the Hardening Parameter.

$S_\theta = S_r = 1.0$

$E = 26700\ ksi,\ \Delta_o{'} = 0.0008,\ \sigma_y = 40.8\ ksi$
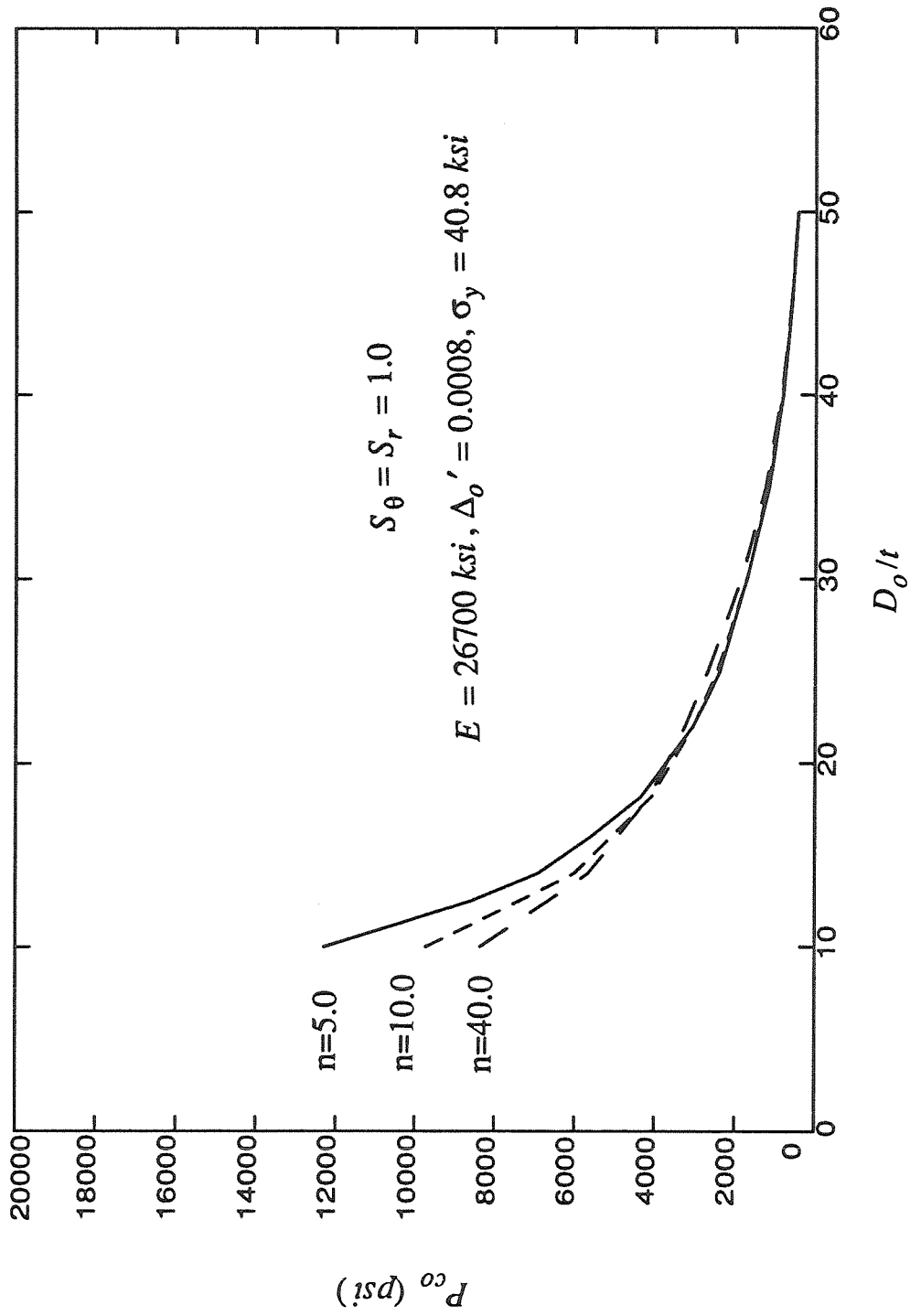
Figure 5.5. Predicted Collapse Pressure (T=0) for Three Different Values of the Material Hardening Parameter n.
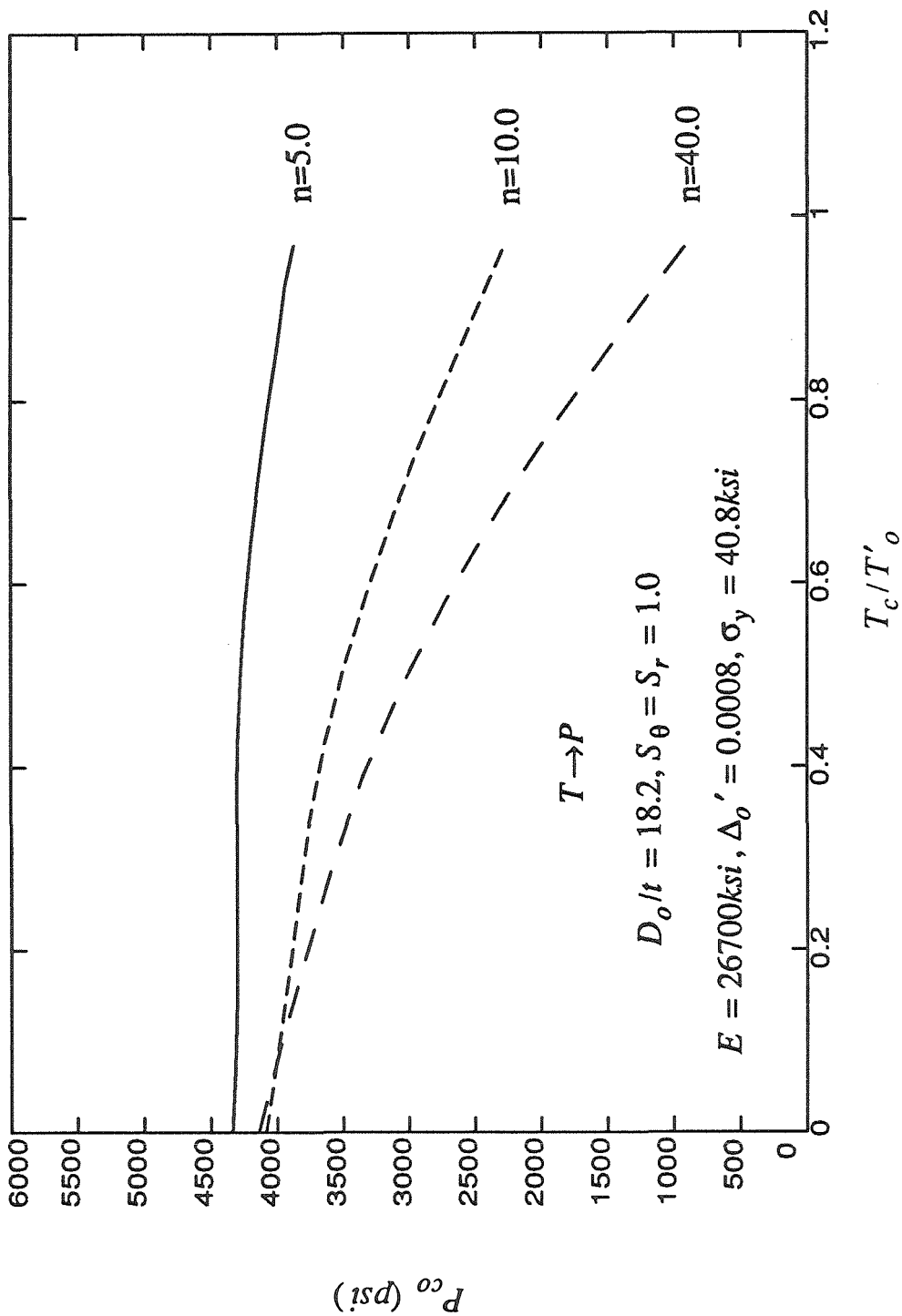
Figure 5.6.   Parametric Study on the Effect of Material Hardening Parameter on Predicted Tension-Pressure Collapse Envelopes ($T \rightarrow P$, $D_o/t = 18.2$)
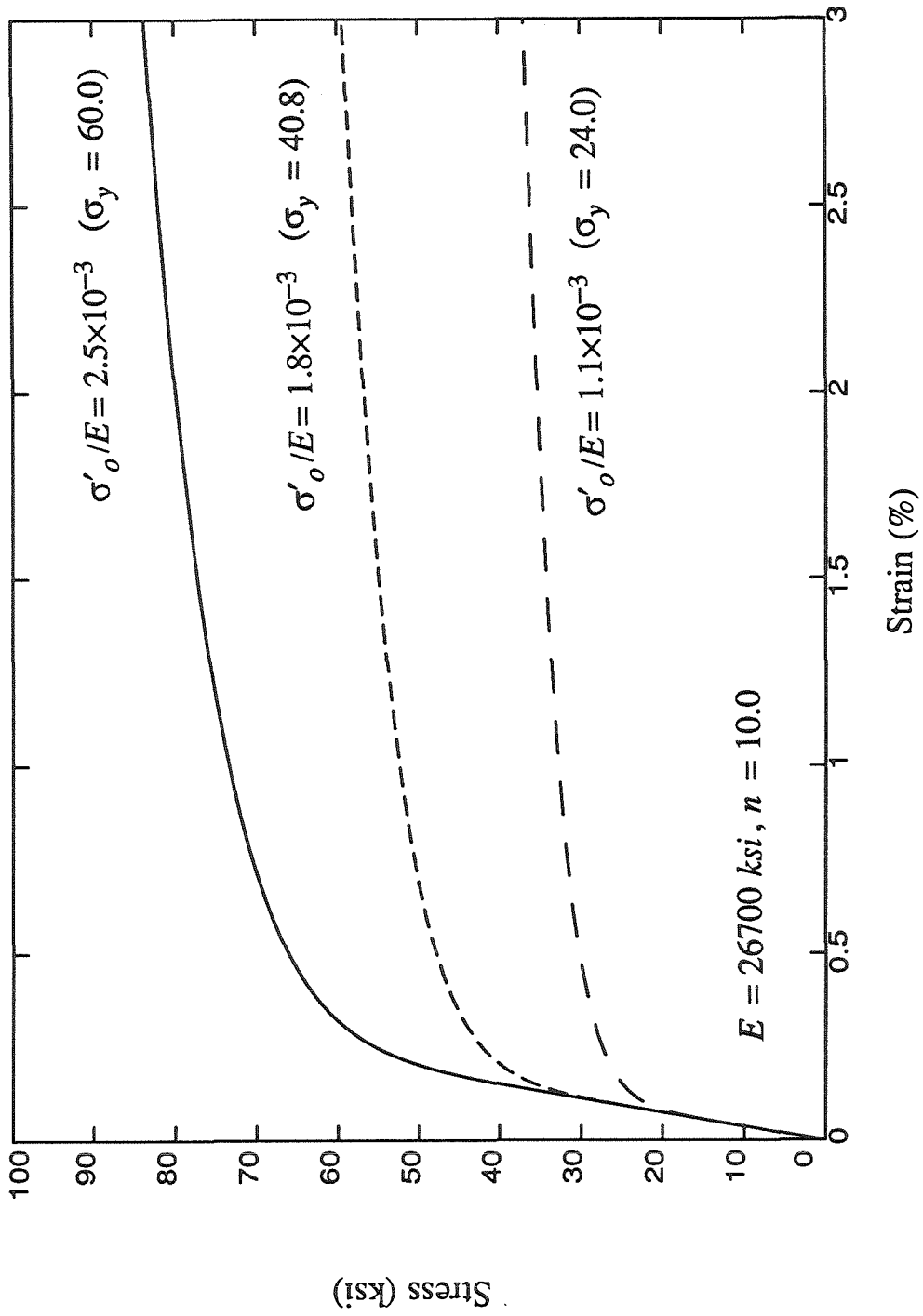
Figure 5.7.   Stress-Strain Curves Represented by the Ramberg-Osgood Fit for Three Different Values of the Yield Stress.
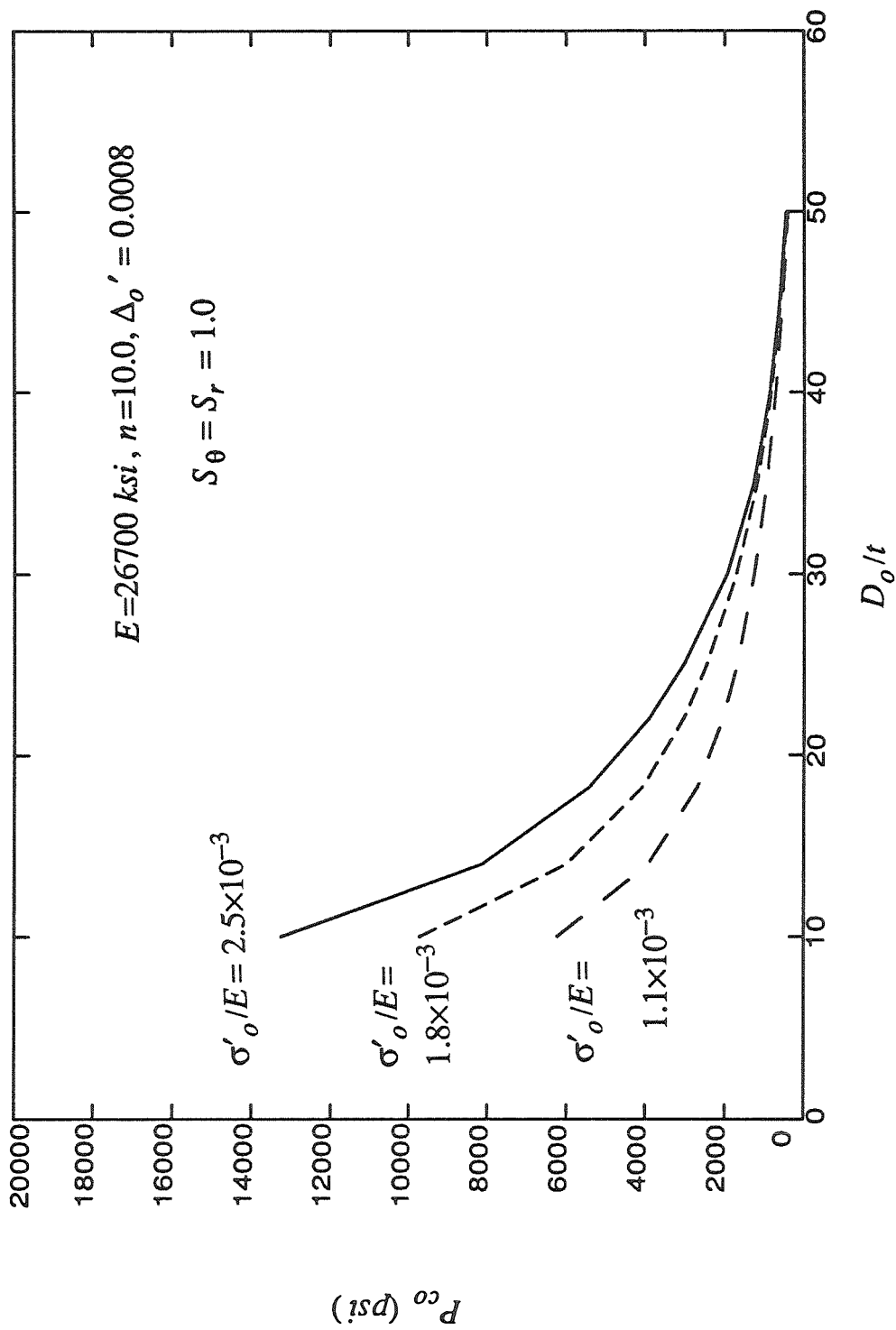
Figure 5.8.   Predicted Collapse Pressure (T=0) for Three Different Values
of the Yield Stress σ'_o.
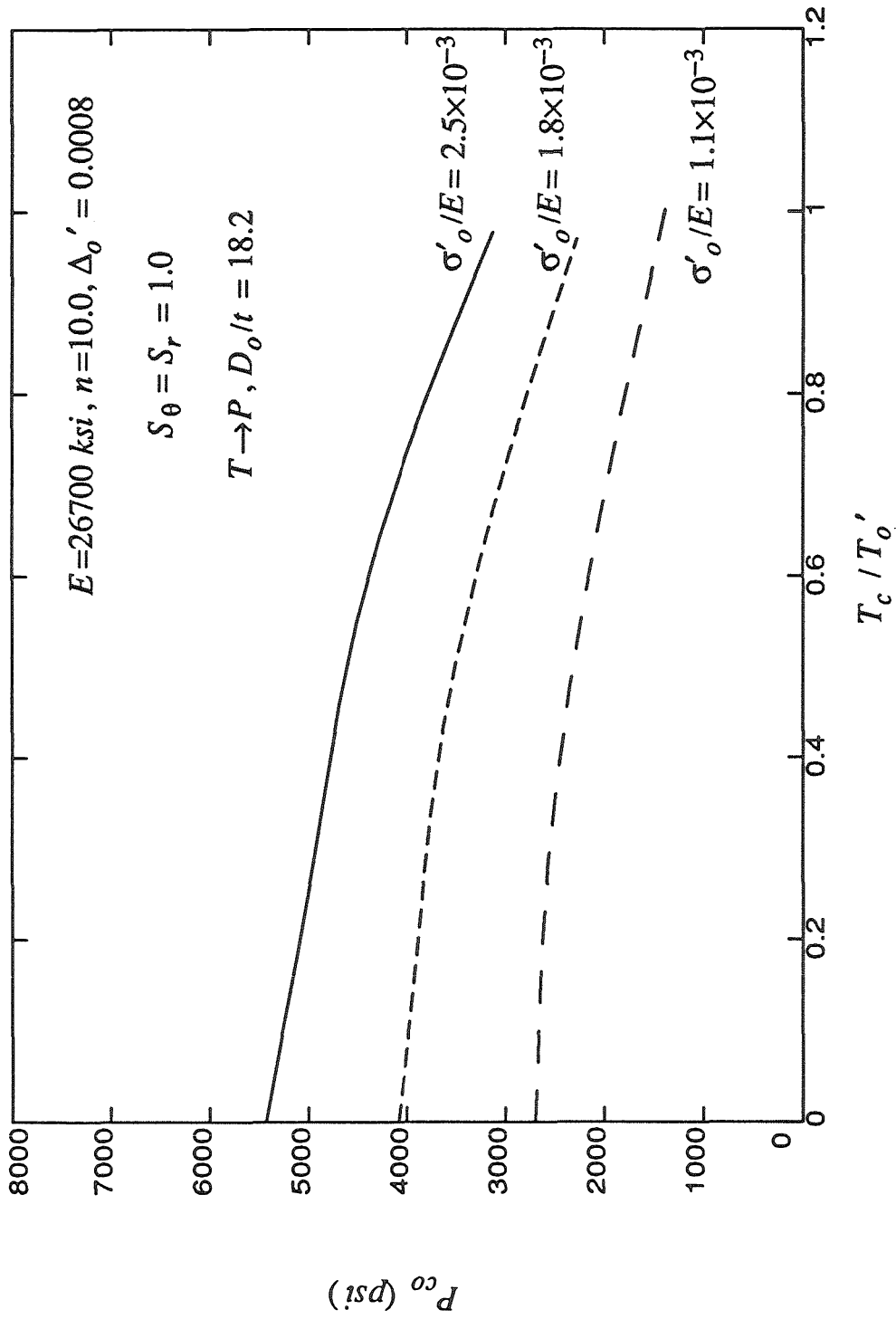
Figure 5.9.   Parametric Study on the Effect of Yield Stress on Predicted
Tension-Pressure Collapse Envelopes (T → P, D_o/t = 18.2)
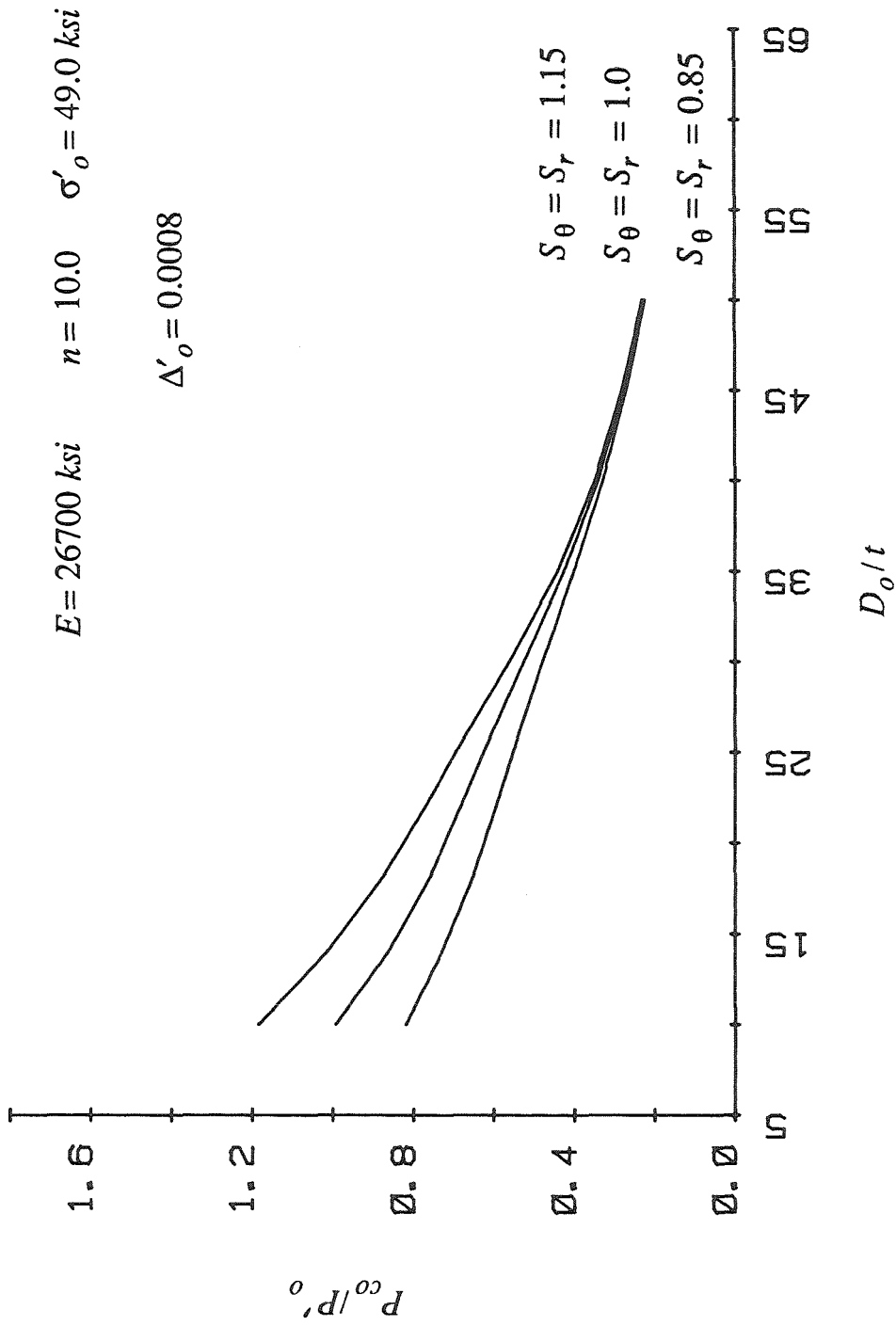
Figure 5.10. Effect of Material Anisotropy on the Predicted Collapse Pressure (T=0)
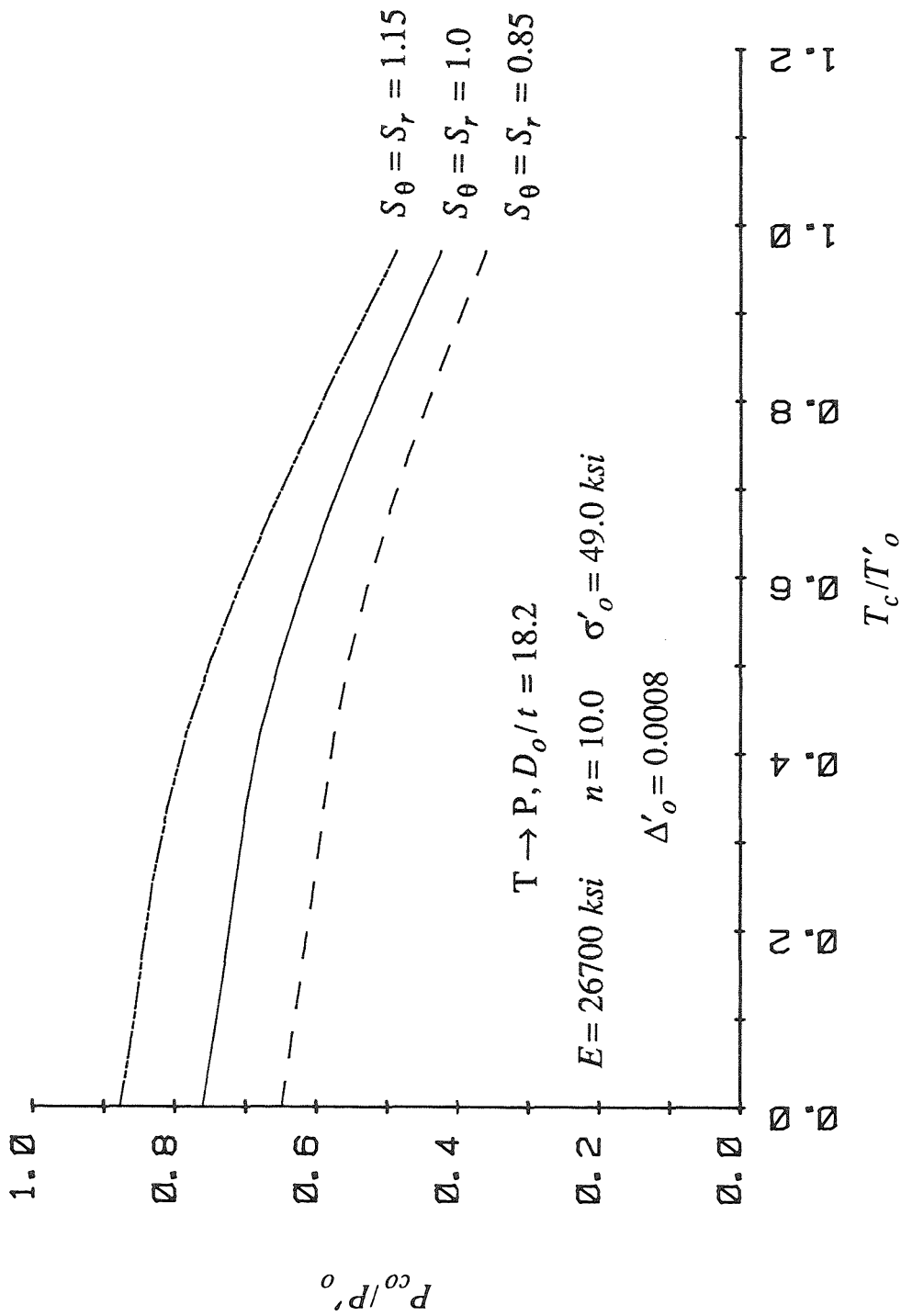
Figure 5.11. Effect of Material Anisotropy on the Predicted Tension-Pressure Collapse Envelope ($T \rightarrow P, D_o/t = 18.2$)
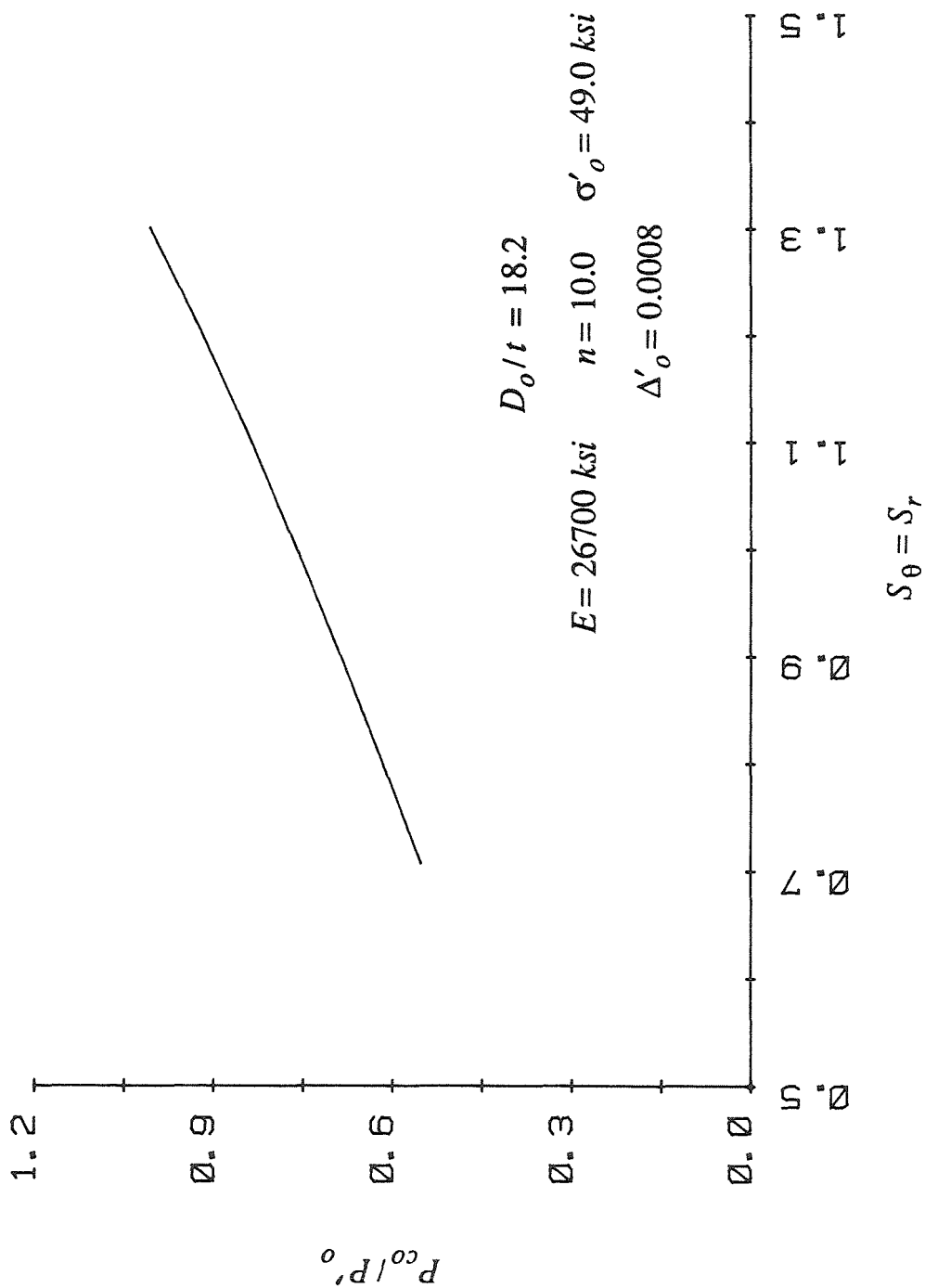
Figure 5.12.   Parametric Study on the Effect of Material Anisotropy on Predicted Collapse Pressure ($T=0$, $D_o/t = 18.2$)
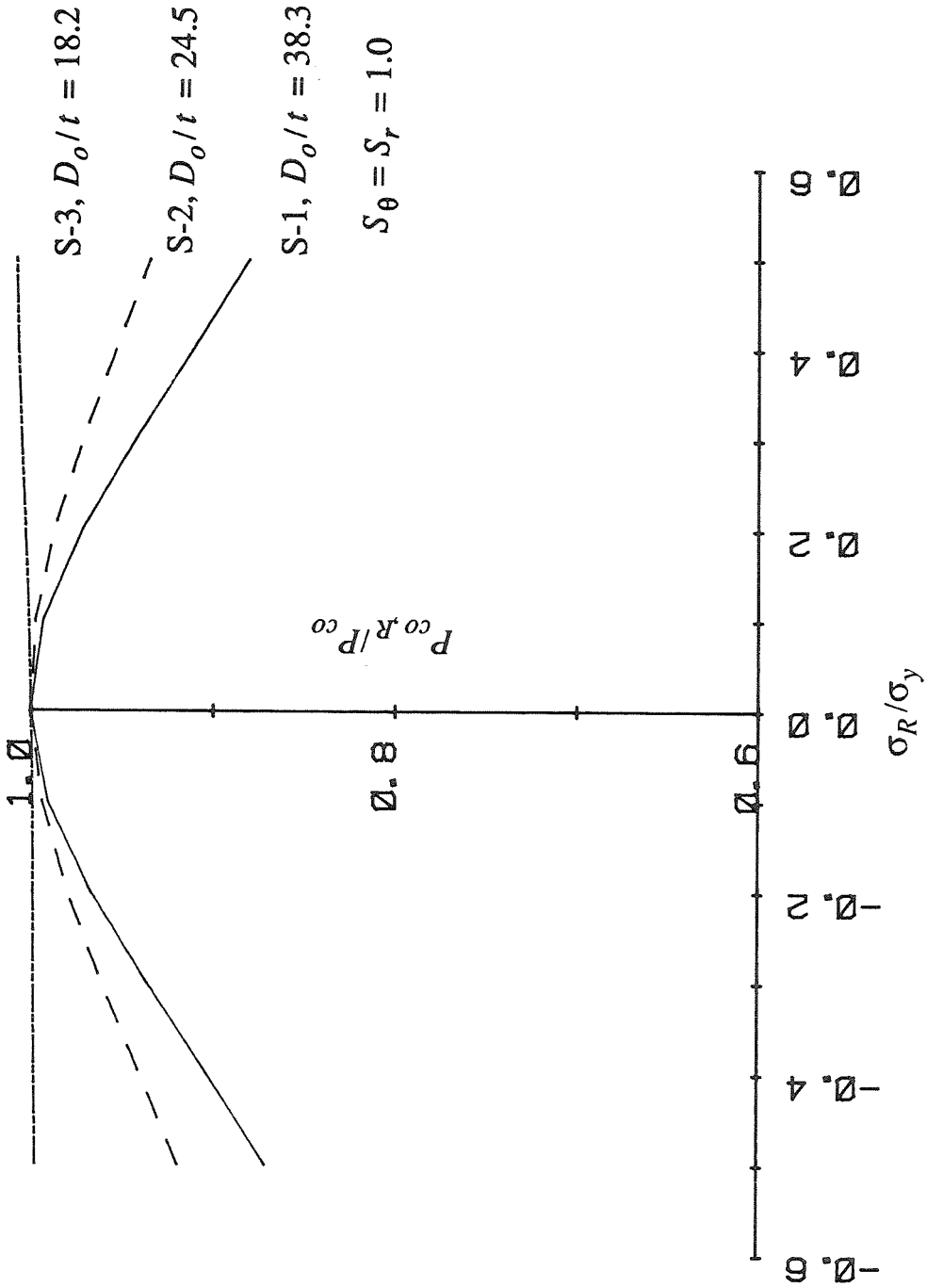
Figure 5.13.   Effect of Residual Stress on Predicted Collapse Pressure (T=0)
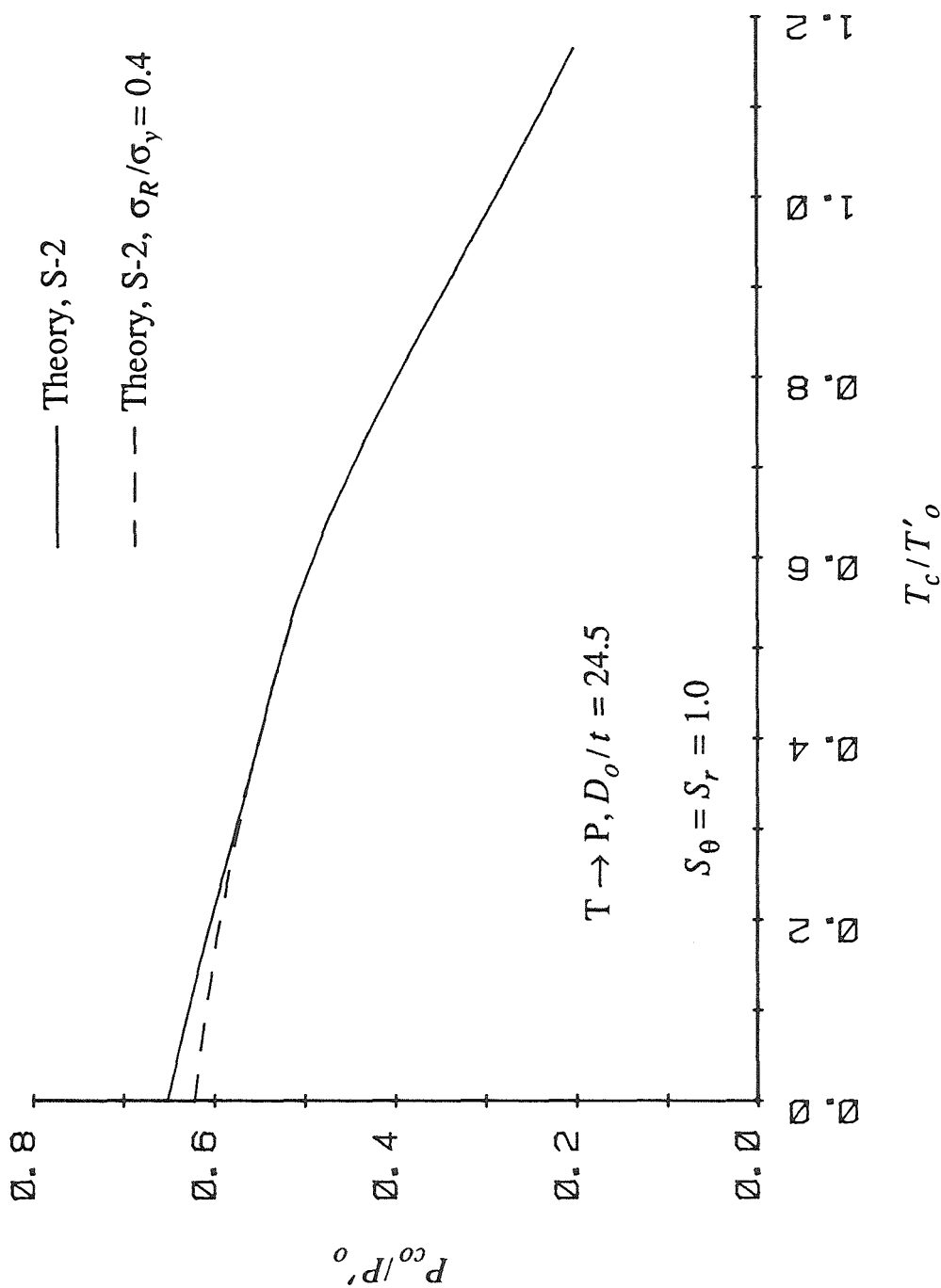
Figure 5.14.   Effect of Residual Stress on Predicted Tension-Pressure Collapse Envelope
($T \rightarrow P$, $D_o/t = 24.5$)
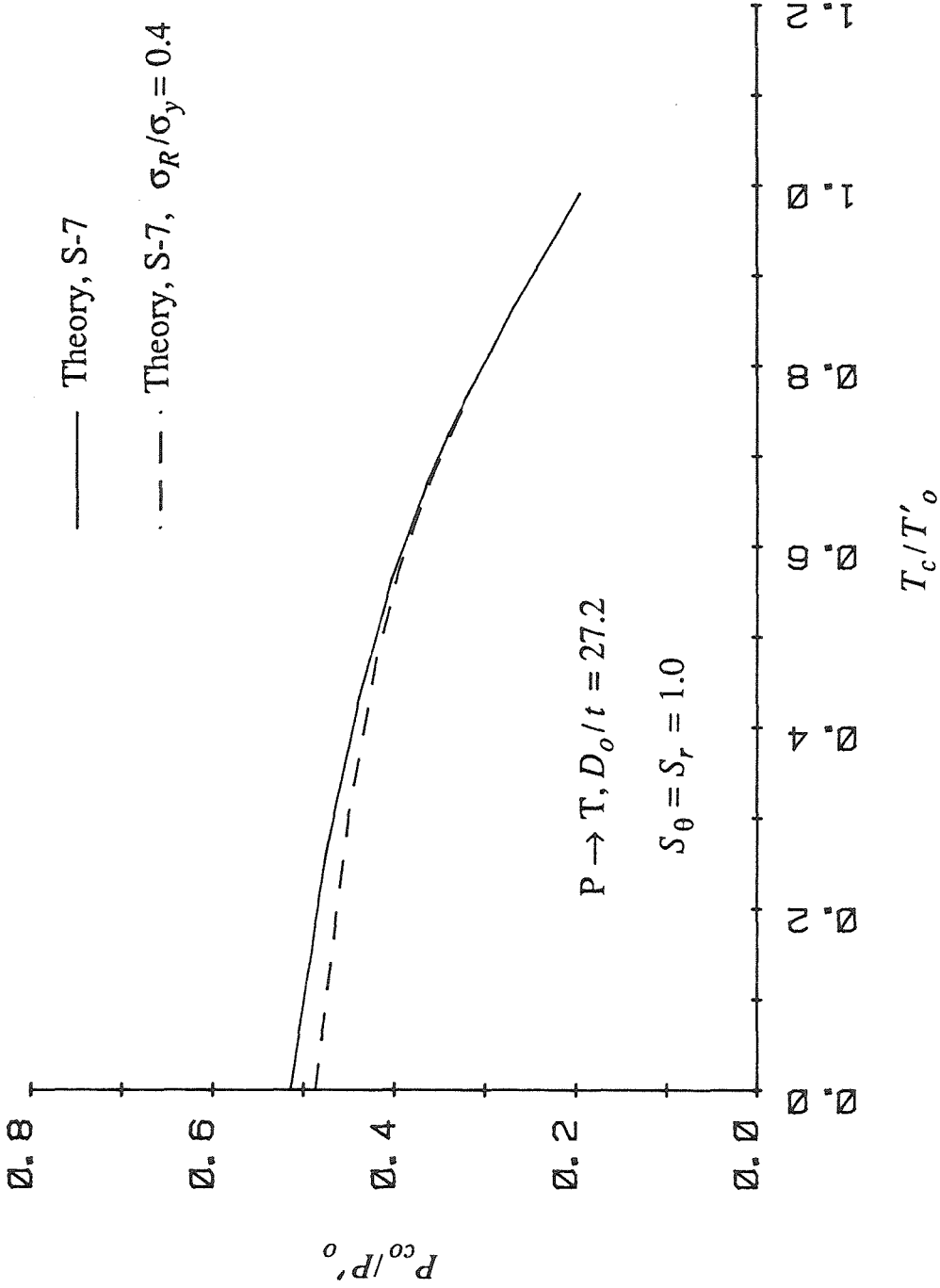
Figure 5.15. Effect of Residual Stress on Predicted Tension-Pressure Collapse Envelope ($P \rightarrow T$, $D_o/t = 27.2$)
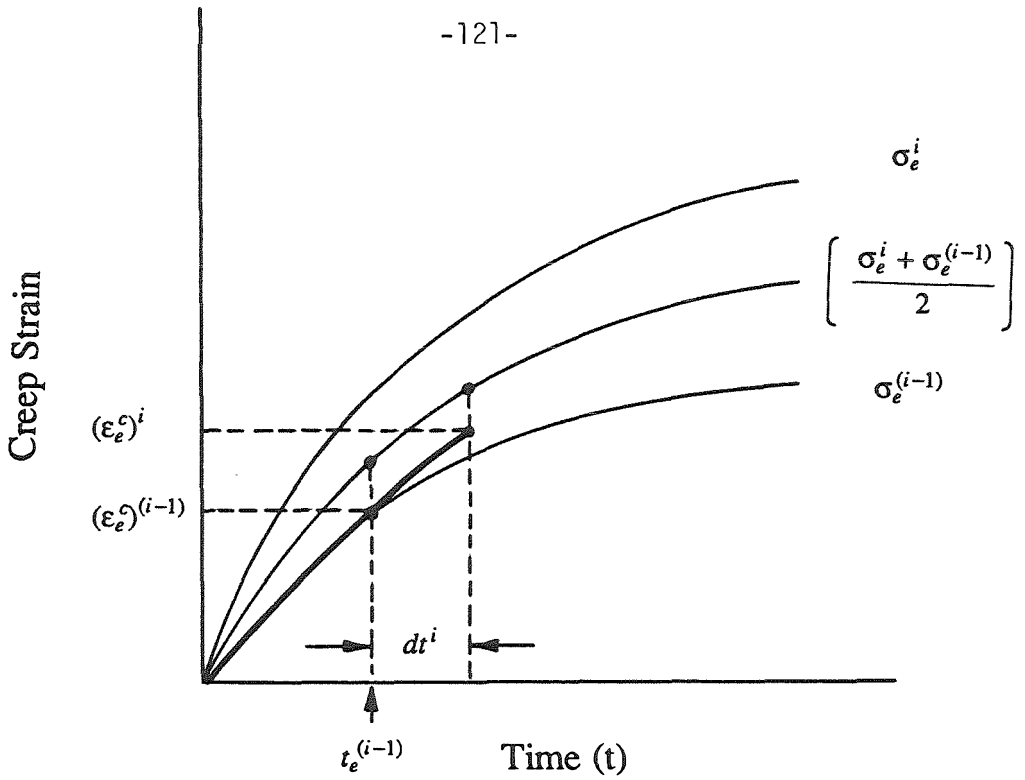
Figure 6.1. Hardening Model Used to Obtain the Creep Strain Increments
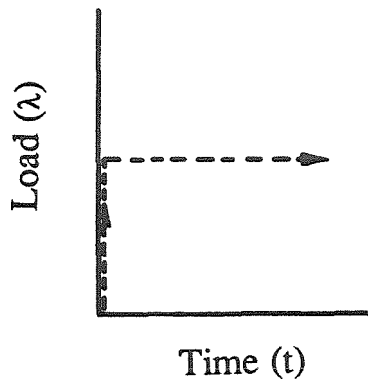
Figure 6.2. Load-Time History Followed in the Numerical Examples.
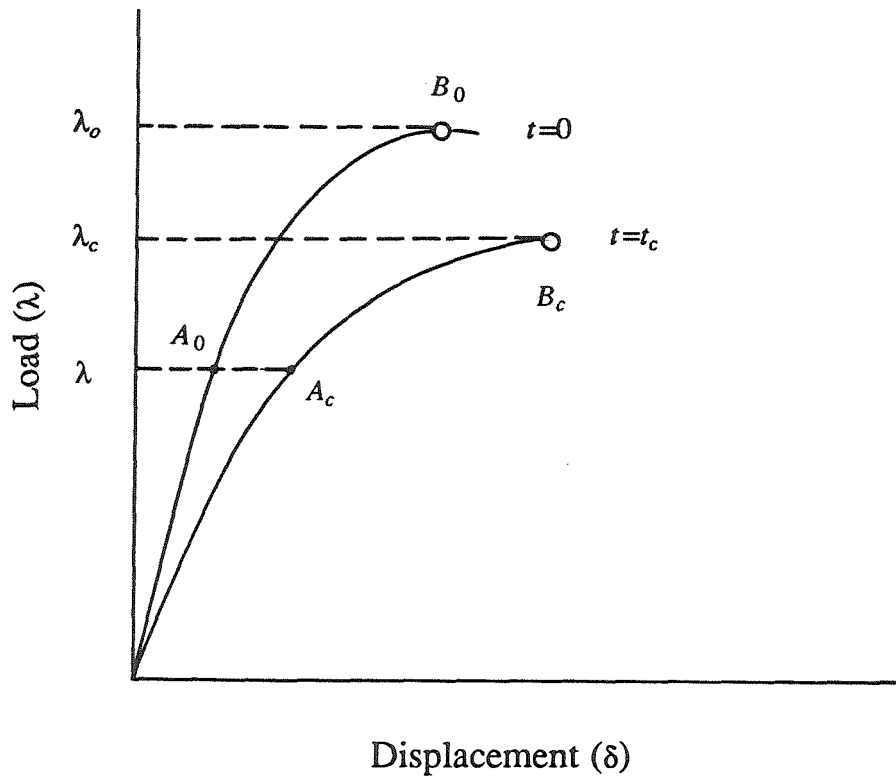
Figure 6.3. Load-Displacement Behavior of the Tube Cross Section
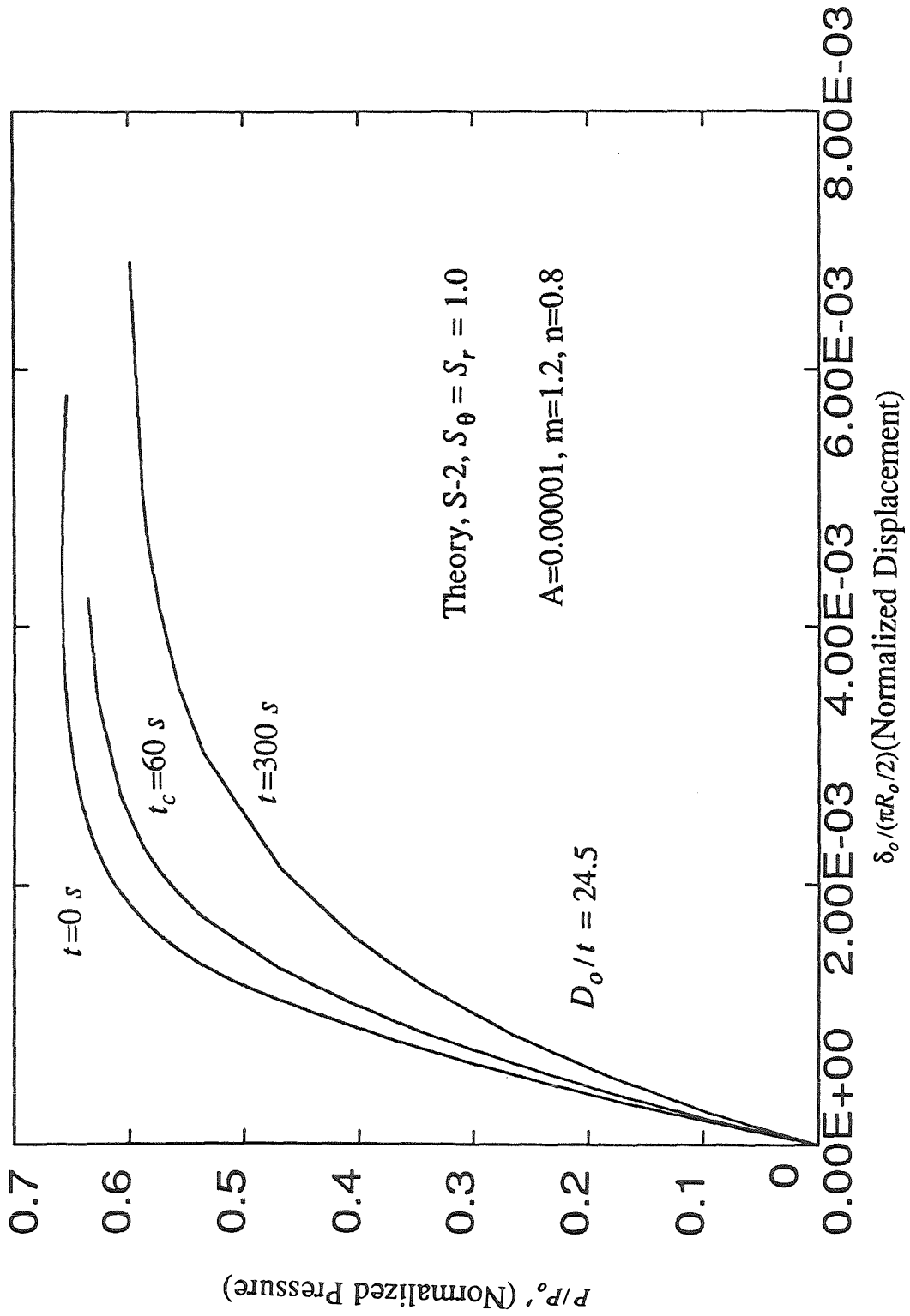
Figure 6.4. Predicted Pressure-Deflection Response Corresponding to Different Time Periods
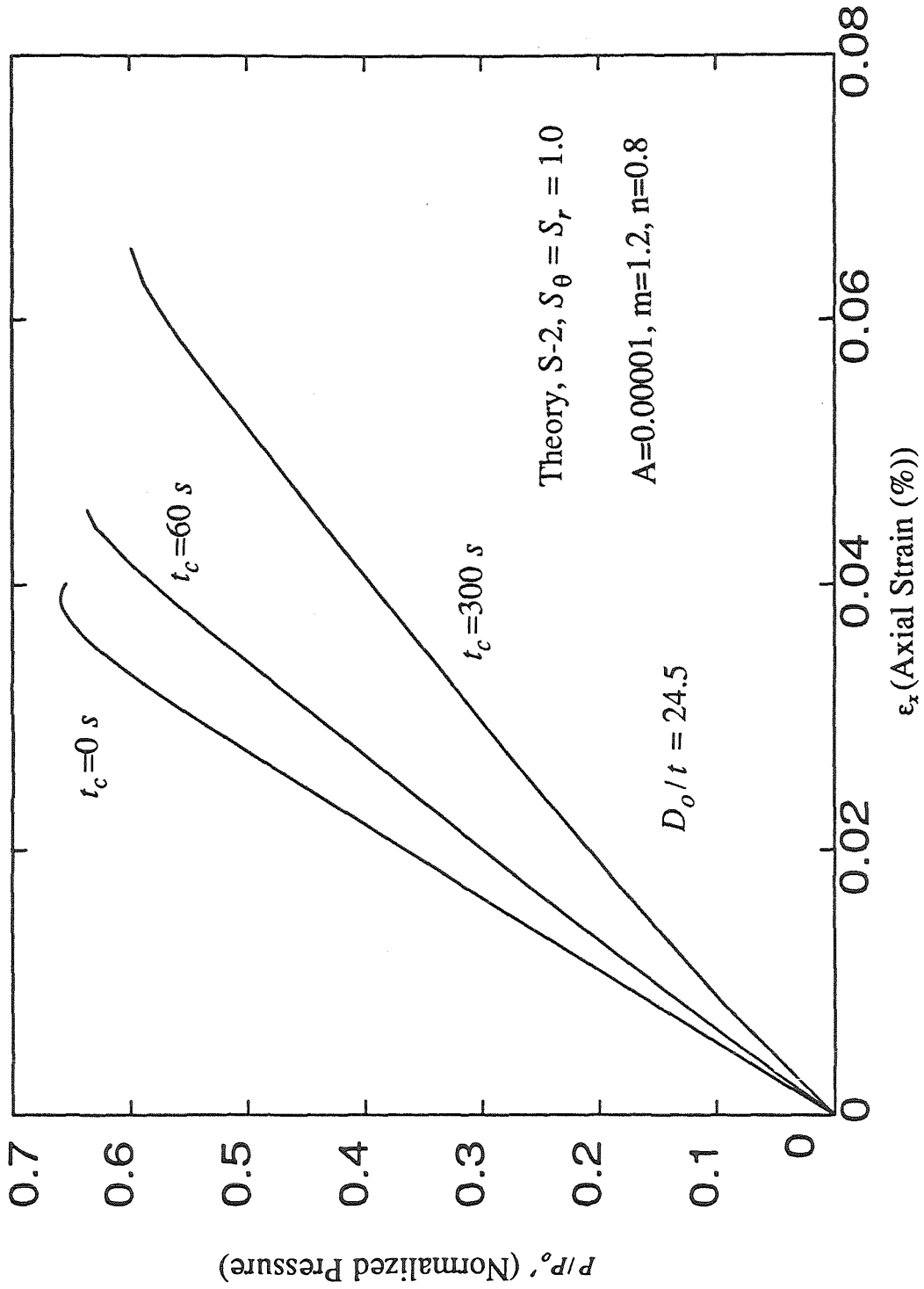
Figure 6.5.   Predicted Pressure-Axial Strain Response Corresponding to Different Time Periods
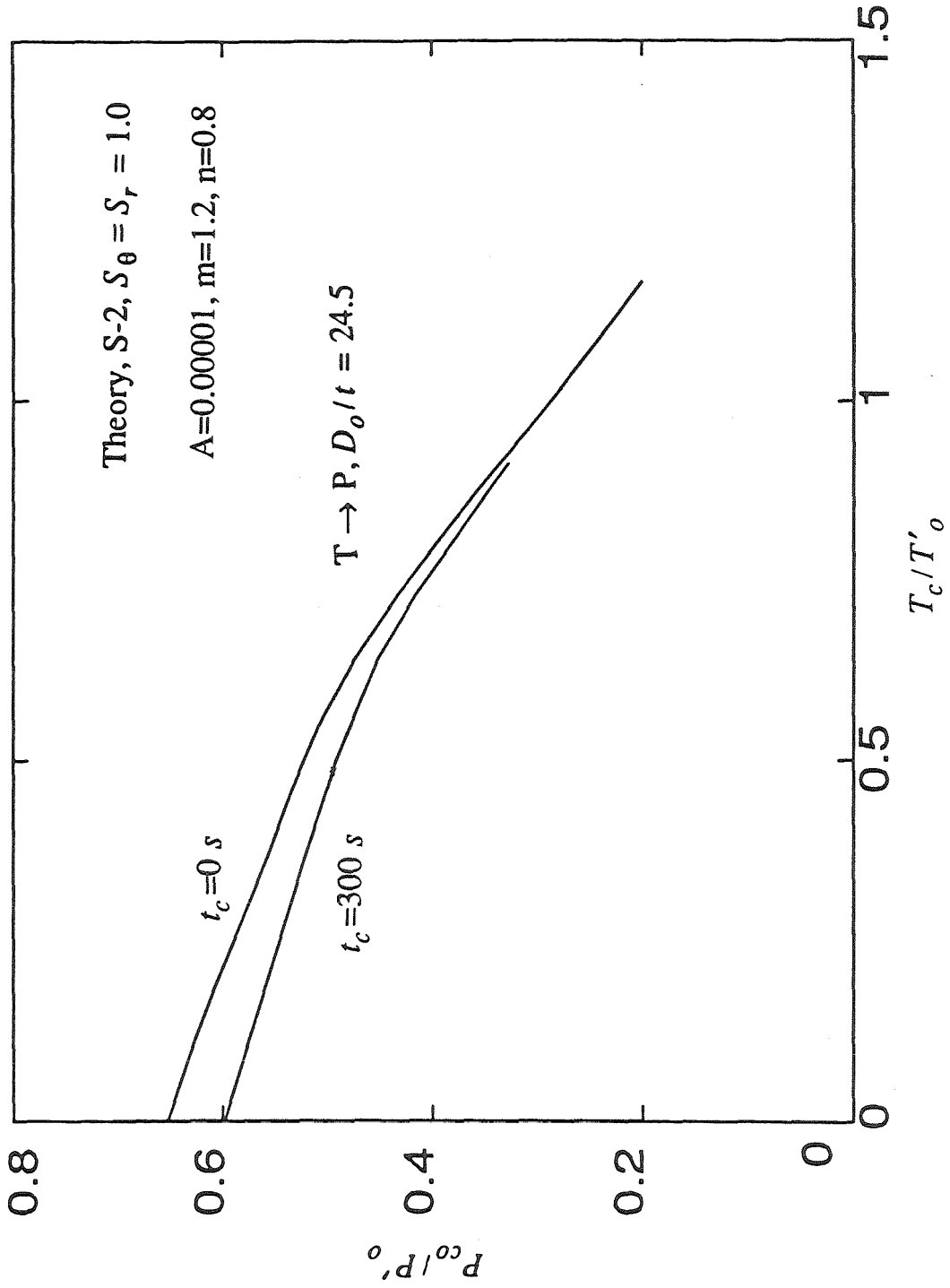
Figure 6.6.   Effect of Primary Creep on Predicted Tension-Pressure Collapse Envelope ($D_o/t = 24.5$, T→P)

Uniaxial test   Lateral Pressure test   Hydrostatic Pressure test
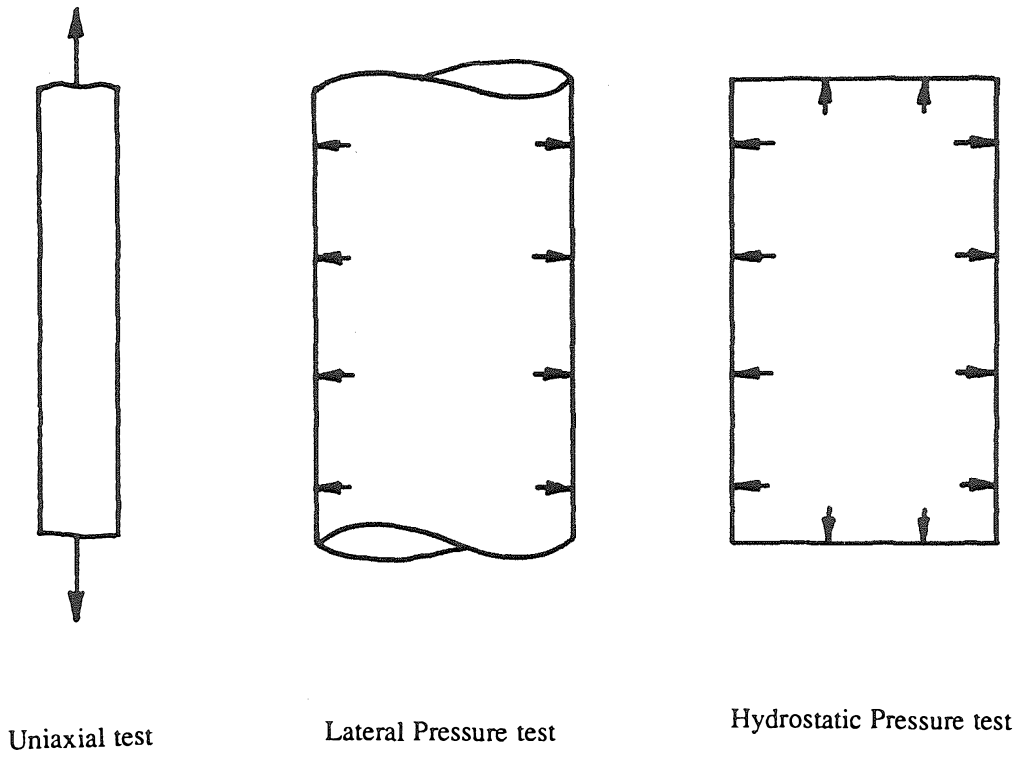
Figure B.1.   Schematic Representation of the Tests to Characterize Anisotropy.
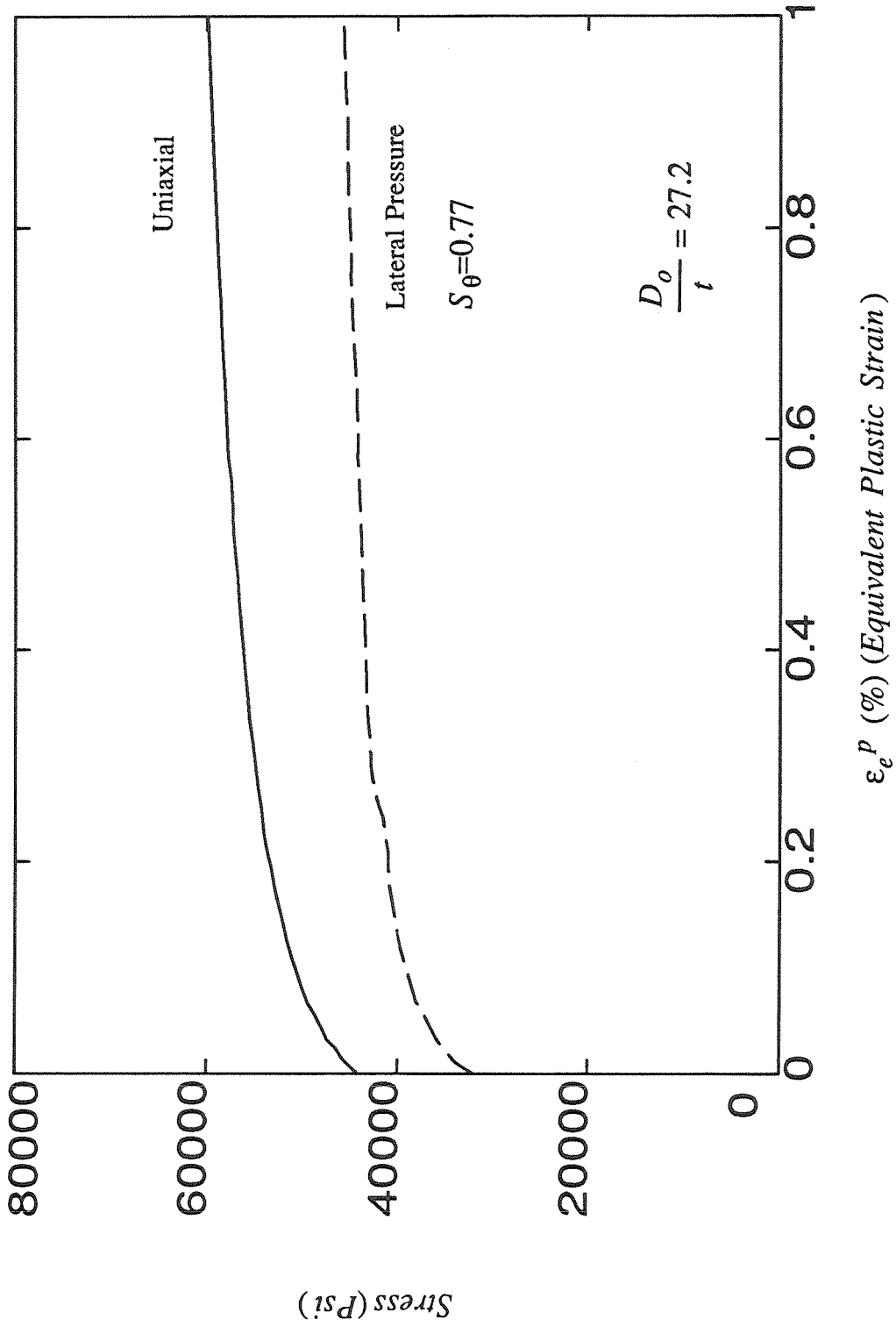
Figure B.2a.   Comparison of Stress-Strain Curves from Uniaxial and Lateral Pressure Tests.
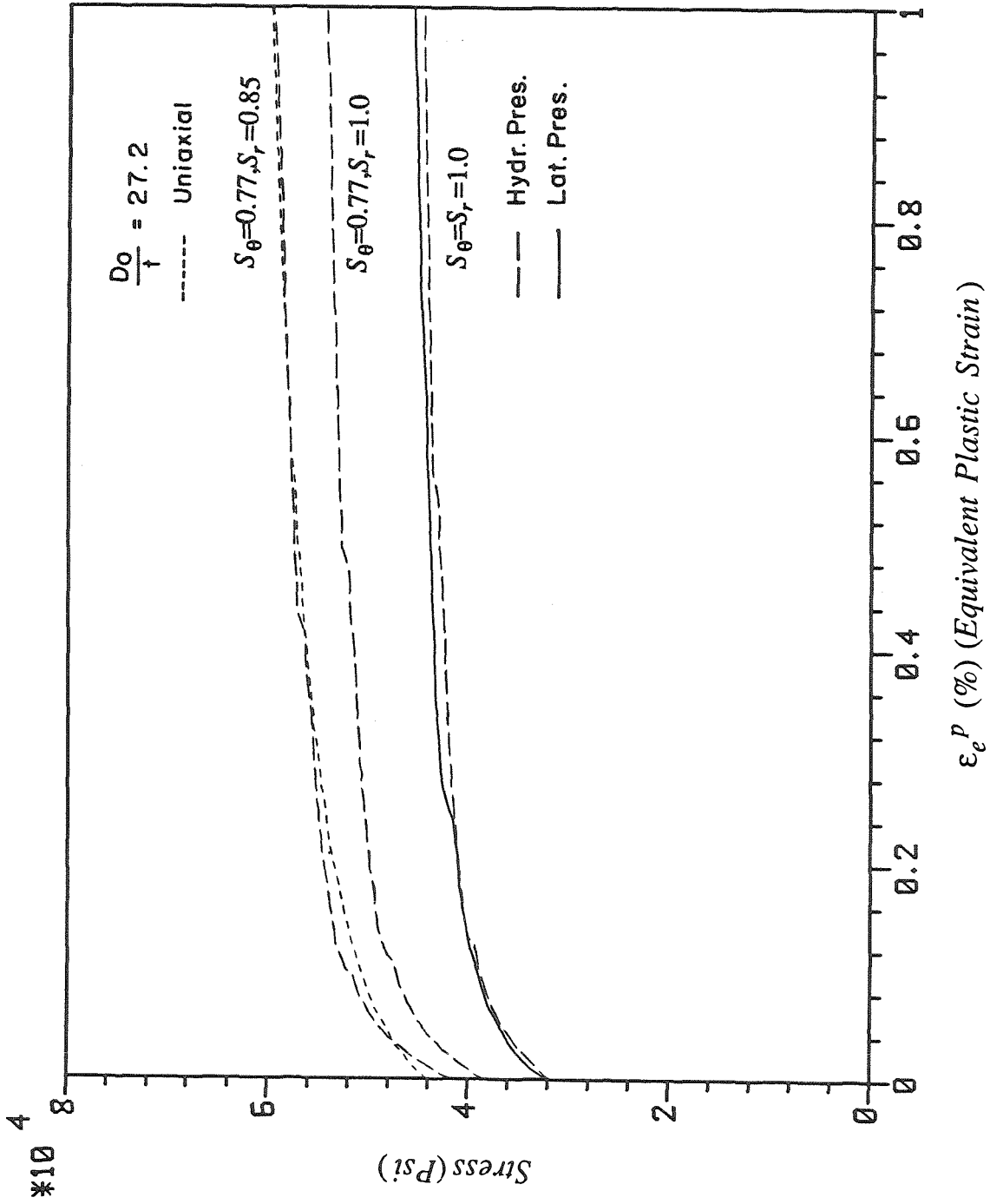
Figure B.2b. Equivalent Stress-Strain Representations for Characterizing the Anisotropic Parameters.